Electrical and Magnetic Investigations on Transition Metal Implanted GaAs

Dissertation

zur Erlangung des Grades eines Doktors der Naturwissenschaften
in der Fakultät für Physik und Astronomie der Ruhr-Universität Bochum

vorgelegt von

Şafak Gök
geboren in Zonguldak, Türkei

Angewandte Festkörperphysik Ruhr-Universität Bochum

Oktober 2006

Bochum

Dissertation eingereicht am	10.10.2006
Erstgutachter	Prof. Dr. A. D. Wieck
	Ruhr-Universität Bochum
Zweitgutachter	Prof. Dr. H. Zabel
	Ruhr-Universität Bochum
Tag der Disputation	18.12.2006

Acronyms

AFM	**A**tomic **F**orce **M**icroscopy
AMR	**A**nisotropic **M**agneto **R**esistance **E**ffect
DMS	**D**iluted **M**agnetic **S**emiconductor
DWR	**D**omain **W**all **R**esistance
EDS	**E**nergy **D**ispersive x-ray **S**pectroscopy
FIB	**F**ocused **I**on **B**eam
FM	**F**erro**m**agnet
GMR	**G**iant **M**agneto **R**esistance **E**ffect
HEMT	**H**igh **E**lectron **M**obility **T**ransistor
LMIS	**L**iquid **M**etal **I**on **S**ource
LT-MBE	**L**ow **T**emperature **M**olecular **B**eam **E**pitaxy
MBE	**M**olecular **B**eam **E**pitaxy
MR	**M**agneto **R**esistance Effect
MOVPE	**M**etal **O**rganic **V**apour **P**hase **E**pitaxy
RE	**R**are **E**arth Metals
RHEED	**R**eflection **H**igh **E**nergy **E**lectron **D**iffraction
RTA	**R**apid **T**hermal **A**nnealing
SEM	**S**canning **E**lectron **M**icroscopy
SQUID	**S**uperconducting **Qu**antum **I**nterference **D**evice
TLM	**T**ransmission **L**ine **M**ethod
TM	**T**ransition **M**etal
2DEG	**2** **D**imensional **E**lectron **G**as
2DHG	**2** **D**imensional **H**ole **G**as
UHV	**U**ltra **H**igh **V**acuum

Contents

Chapter 1

Introduction

The conventional semiconductor electronics bases on the transport of the electron charge which is manageable in the framework of the classical physics. Mass storage of information is performed by magnetic recording using the spin of the electrons in ferromagnetic metallic media, while it is a static process on the quantum mechanical spin feature of the electrons. It is then quite natural that one comes to the idea to deal with charge and spin of the electrons together in one process and in such a way enhance the performance of devices. To realize this vision, the theoretical and experimental efforts are collected under the new multidisciplinary field of so-called *spintronics*. The discovery of the giant magneto resistance effect (GMR) in 1980s is considered in general as the birthday of this fresh technology. It predicates to govern the electrical transport by the spin or to manipulate actively the spins by electric fields. This promises an interesting physics where technologically useful new effects can occur. It will enable higher data storage densities in hard discs, non-volatile random access memory (RAM), and faster devices with more functionality with lesser energy consumption. For this purpose new kind of materials are necessary in which the semiconducting and ferromagnetic properties coexist. The usual semiconductors used for devices and integrated circuits, such as Si and GaAs, are not magnetic due to the absence of magnetic ions. In order to have a useful difference between the energies of the two possible electron spin orientations in these conventional semiconductors magnetic fields would have to be applied which are too high for everyday use. Moreover, the crystal structures of magnetic materials are usually quite different from that of the semiconducting materials, which makes both materials incompatible. The efforts for combine ferromagnetic and semiconducting properties in one material

begun in the late 1960s and early 1970s with magnetic semiconductors, as europium chalcogenides and semiconducting spinels where the magnetic ions are arranged in semiconducting host crystal periodically [1]. These are material systems in form of Eu*X* and *X* is an element of group *VI* in periodic table of elements. Europium chalcogenides are partly ferromagnetic, but the crystal growth of this materials and integration into the heterostructures is notoriously difficult. One of the most important features of semiconductors is the ability to dope them with impurities to change their properties. With this reasoning magnetic elements, and so magnetic moments were incorporated into the nonmagnetic semiconductors to make them magnetic. Semiconducting materials, in which magnetic atoms (transition metals and rare earths) are distributed statistically and form a mixed crystal, are called *diluted magnetic semiconductors* (DMS). Another possibility to make a semiconductor ferromagnetic, ferromagnetic metallic nano-magnets can be embedded into the nonmagnetic semiconducting matrix. These material combinations are called *semiconductor-ferromagnetic hybrid systems*.

In this work it was looked for a ferromagnetic semiconductor with a Curie temperature above room temperature, as semiconductor-ferromagnetic hybrid system. With this motivation magnetic ions manganese, cobalt, gadolinium, terbium and dysprosium are implanted into GaAs. The crystal structure and the magnetic properties of these new compounds are studied. To fabricate such kind of material systems the advantages of a combined molecular beam epitaxy (MBE) - focused ion beam (FIB) system is utilized. This system enables to transfer the sample into the FIB processing chamber under ultra high vacuum (UHV) conditions, so that the implantation can be done into the fresh grown GaAs with a chemically active clean surface. Another possibility in this FIB system is to work in soft landing mode, in order to deposit magnetic ions into the semiconducting GaAs lattice with very low crystal defects [2-11].

As well the transparent (in the visible) II-VI semiconductor ZnO is a promising material for spintronics because of the physical properties. ZnO has an extremely high exciton binding energy of 60 meV (exciton binding energy of GaAs is 4.2 meV). The energy band gap is 3.35 eV at RT, which is similar to GaN, the material with highest Curie temperature [46], but ZnO is more stable. These and other features make ZnO a better candidate for (opto-electronic) applications than all other known materials. The

n-type doping of ZnO can be performed successfully, but p-type doping is a mighty challenge, which is reported only by a few groups for particular cases up today. For electronic applications both p- and n-type doping is necessary. For this purpose Co ions are implanted into ZnO and transport properties are studied.

This thesis begins with the theoretical fundamentals of semiconductors, micromagnetism, DMS, semiconductor-ferromagnetic hybrid structures, and transport phenomena (chapter 2). The principle of the experimental techniques and the facilities, which are used, are represented in chapter 3 with schematically drawings. The physical processes in the interaction of the ion beam with a solid are considered theoretically in chapter 4.1. The experimental data of the focused ion beam implantation process of the ions Mn, Co, Gd, Tb, and Dy into GaAs are presented in the residual part of the chapter 4. In this chapter also the results of the structural investigation by atomic force microscope (AFM), and the investigation of magnetic features by superconducting quantum interference device (SQUID) are shown. The chapter 5 is devoted to magneto transport measurements on (1) (Ga,Mn)As grown epitaxially by LT-MBE and (2) manganese implanted heterostructures overgrown by a III-V MBE system. About the doping of ZnO, which shows simultaniously ferromagnetic hysteric curves, is reported in chapter 6. In chapter 7 the initial goals and achieved results are summarized. An outlook and some suggestions are also mentioned. The mask layouts, which are used for photolithographic processes on the samples, can be found in appendix A. Appendix B summarizes the properties of GaAs tabular. The layer structures and some characteristic parameters of the samples are listed in appendix C. The units of the physical values occurred in considerations about magnetism are summarized tabular in appendix D. The selected features of ZnO are listed in appendix E.

Special names like company, machine, book and people names are written italic; as well mathematical terms which are appear in an equation are written italic in explaining texture.

Chapter 2

Theoretical basics

The goal of this work is to produce ferromagnetic semiconductors by implantation of magnetic ions into a nonmagnetic matrix. Chapter 2 gives an introduction into the theoretical basics, which are necessary to understand the lattice structure and the origin of the electronic and magnetic transport properties of ferromagnetic semiconductors. The basic definitions of the semiconductor physics are introduced exemplarily for the semiconductor material GaAs in chapter 2.1. In chapter 2.2, one of the main objects of this work, DMS are discussed, which are a convolution of a semiconducting material and implanted ferromagnetic ions. In chapter 2.3 the basic ideas of the micromagnetic theory of ferromagnets, particularly the energetics of ferromagnetic materials are expressed by the micromagnetic equations. Finally, in chapter 2.4 a summary of the basics of the transport theory is given.

2.1 Semiconductors

The forbidden zone (band gap E_g) in the order of 1 eV in the energy landscape is the most noticeable feature of semiconductors. The presence of this band gap dominates the properties of semiconductors and is defined as the energy difference between the highest totally occupied valence band state and the lowest unoccupied conduction band state. The band gap is temperature and pressure dependent. All eigenstates in the valence band are occupied and all eigenstates in the conduction band are empty at 0 K, so that semiconductors become insulators. This results from the phenomenon that a totally occupied band gives no contribution to the conductivity. However these electrons in the valence band can be excited optically or thermally into the conduction

band. Then an applied electric field makes electron transport within the conduction band (and hole transport within the valence band) possible. If there are only excited electrons in the conduction band and excited unoccupied eigenstates in the valence band with the same concentration, the semiconductor is called intrinsic, in which the number of the mobile electrons depends strongly on temperature. Figure 2.1 shows the temperature dependence of the intrinsic carrier density.

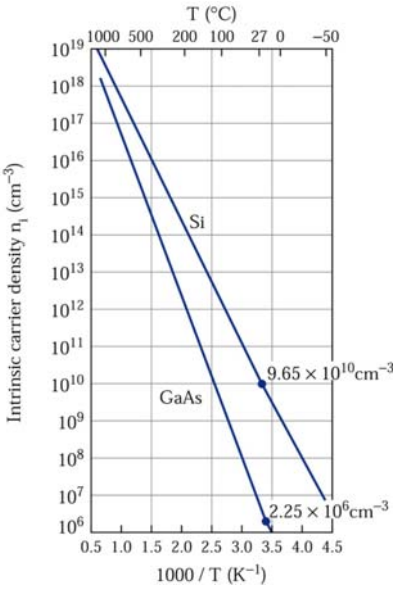

Figure 2.1: *Intrinsic carrier densities in Si and GaAs are drawn as a function of reciprocal temperature [12].*

The doping of electrically active impurities into the crystal lattice can vary the carrier density in semiconductors. Doping generates the impurity levels E_D and E_A, and their position in the forbidden zone depends on the binding configuration of the dopants in the matrix. The carriers from impurities are denoted extrinsic carriers. The doped impurities are called donors, if they have more valence electrons than the lattice atoms so that they give electrons to the conduction band, increasing the electron concentration in semiconductor and make it n-type. In this case electrons are the majority carriers. The accrued donor level E_D lies just under the conduction band and the fermi level is shifted closer to the E_C (figure 2.2.b). The doped impurities are called acceptors, if they have fewer electrons than the lattice atoms, so that they get electrons from the valence band and generate holes there. In all, they increase the hole

concentration in semiconductor and make it p-type. In this case holes are the majority carriers. The accrued acceptor level E_A lies just over the valence band and the fermi level is shifted closer to the E_V (figure 2.2.b).

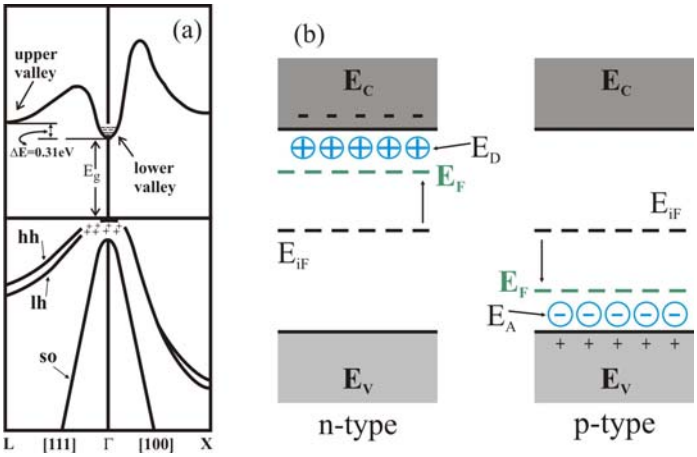

Figure 2.2: *Energy band structure of GaAs is drawn schematically. (a) hh is the heavy hole band, lh the light hole band and so the split-off band. (b) The donor and acceptor levels are shown for n- and p-type GaAs. E_{iF} marks the Fermi energy for intrinsic GaAs [12, 13].*

The energy width of the donor and acceptor bands depends on the impurity concentration; the higher the impurity concentration the wider the impurity band. In the case of very high doping the donor band overlaps the conduction band minimum and the acceptor band the valance band maximum, respectively. In this case the semiconductor is degenerate. In degenerate semiconductors the fermi level falls into the conduction band and the semiconductor conducts even at 0 K like a metal. Such materials are used as contact layers in metal/semiconductor junctions [12, 13, 14].

Thus, the technologically important parameters of semiconductors are the band gap E_g, electron or hole concentration n or p, and the corresponding mobility μ_n or μ_h. For small fields, the mobility μ is proportionality constant between electric field E and drift velocity v_D in equation $v_D = \mu E$.

The schematic in figure 2.3 shows principally the electron density in the conduction band as a function of temperature for Si. The extrinsic electrons (holes) are bound to the donors (acceptors) at cryogenic temperatures and this interval is the so-called

freeze-out range. With increasing temperature the impurities are ionised, so that all of them are ionised around RT and the maximum carrier concentration is achieved for a certain impurity concentration. Then the carrier density does not more depend on temperature. This interval is called extrinsic range (or saturation range). For technological applications the extrinsic range around 300 K is desired so that the extrinsic carriers defined the conduction. At very high temperatures the intrinsic carriers are dominant, so that the semiconductor behaves like an undoped one, which is not interesting for the electronic applications.

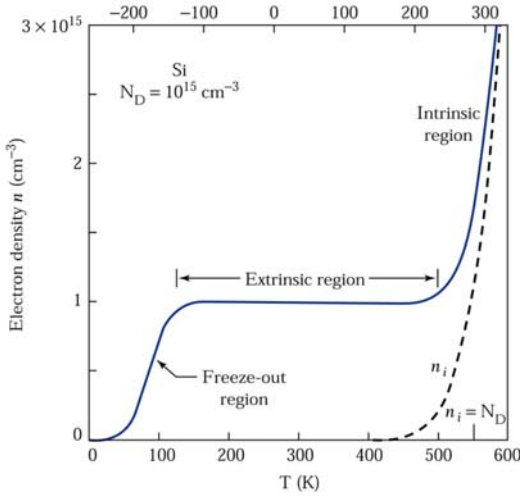

Figure 2.3: *The electron density in the conduction band is drawn as a function of temperature in Si with a donor concentration of $N_D=10^{15}$ cm^{-3} [12].*

There are different kinds of semiconductors: (1) the elemental semiconductors like Si and Ge, (2) the compound semiconductors, which are a combination of many elements, for instance binary (2 compounds), ternary (3 compounds) and so on. The binary semiconductor GaAs combines elements from group III (Ga) and V (As) of the periodic table, and therefore is called as III-V-compound semiconductor. The binary semiconductor AlAs and ternary one AlGaAs are used for instance in HEMT (high electron mobility transistor) structures. Most of the technologically important semiconductors, like GaAs, have fcc lattice with a two-atom basis; this is illustrated in figure 2.4.

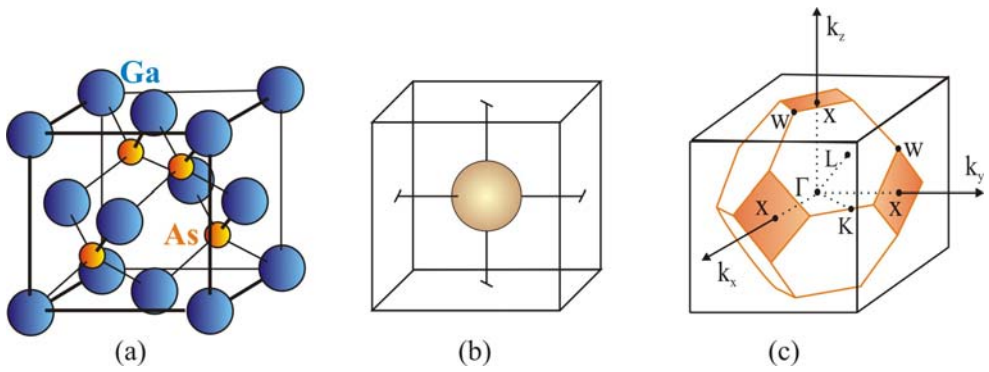

Figure 2.4: *(a) GaAs crystallises in so-called zinc-blende structure. (b) The constant energy surface for GaAs is a sphere at zone centre (Γ point). (c) The Brillouin zone for zinc-blende lattice is shown (the Wigner-Seitz cell) [12].*

At temperatures between 0 K and 300 K the only relevant action (i.e. thermal excitation of electrons and holes, optical absorption edges) occurs close to the valence band maximum and the conduction band minimum. If these energy levels are at the same ***k*** value, this material is qualified as direct-gap semiconductor and if not as an indirect-gap semiconductor. Direct-gap semiconductors like GaAs are interesting especially for optoelectronic applications. Because of the direct transition between the valence band and conduction band, there is no phonon excitation necessary. Every photon can generate directly a transition and vice versa every transition generates a photon without loosing excitation energy as crystal vibrations (phonons).

It is decisive for the $Al_xGa_{1-x}As/GaAs$ material system that it is qualified excellent for epitaxially growth of semiconductor heterostructures because of the very small lattice mismatch of smaller than 0.14 % and a large band gap difference of about 0.8 eV. Experiments were performed on such HEMT samples, which have principilly a high mobility. If the free motion of the charge carriers in a semiconductor heterostructure is confined in the growth direction by a heterostructure like $Al_xGa_{1-x}As/GaAs$, the energy of the carriers is quantised in growth direction and a two-dimensional carrier system builds up. The confinement is necessarily in the order of de Broglie wavelength of the carriers (~ 10 nm). Material systems containing two-dimensional electron gas (2DEG) consist of minimally two different epitaxially grown semiconductor layers with different band gap. If the lattice parameter of the substrate varies from that of the

grown layer, the layer takes the lattice constant of the substrate and the layer is strained. This kind of samples can be grown in III-V-MBE systems as presented in chapter 3.

If the layer $Al_xGa_{1-x}As$ with the larger band gap (E_g ~ 1.76 eV at RT) is doped n-type in a semiconductor heterostructure, the extrinsic carriers move to the lower energy levels of the undoped layer GaAs with smaller band gap (E_g ~ 1.42 eV at RT). Thus the ionised impurities and the extrinsic carriers are spatially separated and induce an electric field. This field modifies the band structure so that a quantum well forms at the interface between $Al_xGa_{1-x}As$ and GaAs. The doping can be performed so that only one subband of the quantum well is deeper than the Fermi-level. The extrinsic carriers occupy this level. Their motion is free in the layer plane and confined in the growth direction. Therefore it is called two-dimensional electron gas (2DEG). The spacer layer, an undoped $Al_xGa_{1-x}As$ layer, is grown between the $Al_xGa_{1-x}As$ / GaAs layers in order to separate the carriers from the ionised impurities. This is the "modulation doping" technique. Figure 2.5 shows exemplarily the band structure of a HEMT sample.

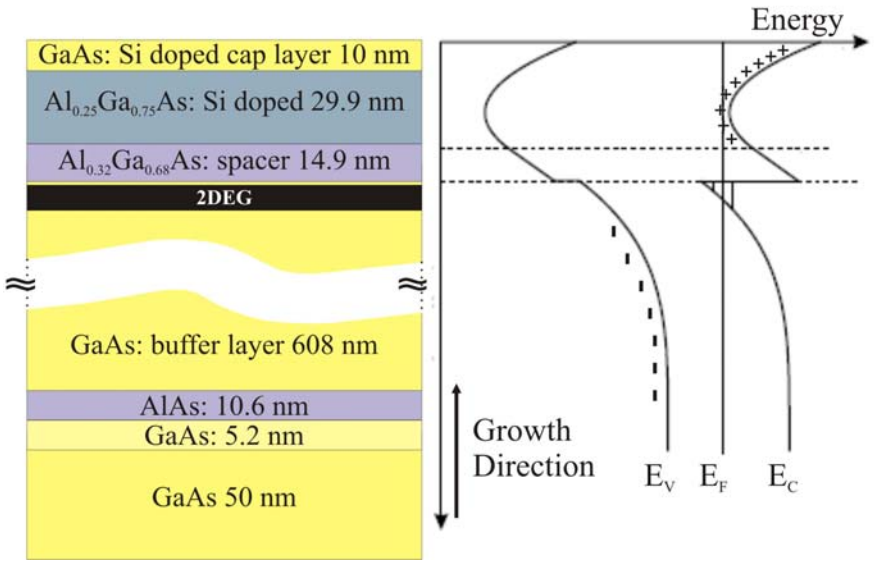

Figure 2.5: *A HEMT structure and the simulated band structure are shown.*

Because the spacer layer eliminates the scattering of the extrinsic carriers from the ionised impurities, the mobility in a 2DEG is high, typically around 6000 cm^2/Vs at

RT and approximately 10^6 cm^2/Vs at 4.2 K. The electron concentration in a 2DEG ranges typically from $2 \cdot 10^{10}$ cm^{-2} to $6 \cdot 10^{11}$ cm^{-2} [15, 16]. By appropriate choice of the material system and the doping, a two-dimensional hole gas (2DHG) is also possible.

2.2 Diluted magnetic semiconductors

The problem of making semiconductors magnetic by ion implantation is discussed here. The circuit elements of the classical electronics process with the charge of the electrons and have had a great success. Today's information mass storage technology uses the electron spins in ferromagnetic metals. The spintronics technology tries to integrate the ferromagnetic features into the semiconductors and to use the charge and the spins parallel [1]. In the framework of this new technique, one should be able to generate, transfer, control, modify, and detect a single spin or an ensemble of spins. In order to generate spin-polarised current in a semiconductor, the electron spins can be polarised in a magnetic material, for instance in a ferromagnetic metal, and injected into the semiconductor through a ferromagnetic metal/semiconductor junction (Schottky barrier). But the spins are scattered strongly at the interface of FM metal and semiconductor, so that such a junction becomes inefficient. It is already proved that spin-injection from a FM semiconductor into a nonmagnetic semiconductor has higher efficiency than from a FM metal into semiconductor [17]. The spins of the electrons can be polarised also just in the semiconductor. For this purpose, this semiconductor must contain magnetic moments, which align the electron spins. But usual semiconducting materials do not contain such magnetic moments. The relaxation time, in which the spin polarisation decays, is another challenge. These problems, spin injection, spin polarisation in the semiconductor, and spin relaxation, are the present challenges for the new technology of spin-based electronics. A spin selective junction, for instance, might do the spin detection. If we cope with these different process steps, it may allow us to carry out *qubit* (quantum bit) operations required for quantum computing. However, there are good reasons why this has not yet been realized [1]. Due to the mentioned problems above, the attention and efforts of many groups are concentrated on the semiconductors with magnetic properties.

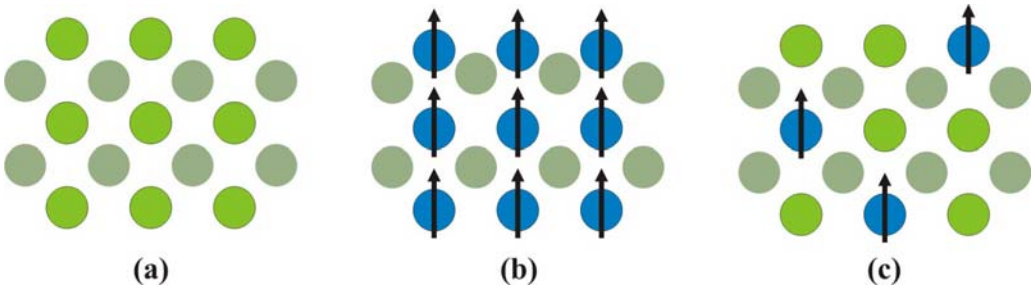

Figure 2.6: *The principle structure of (a) nonmagnetic semiconductors, (b) magnetic semiconductors and (c) diluted magnetic semiconductors are drawn [1].*

New materials are necessary to govern spins and charges of the carriers simultaneously. The common semiconductors used for devices and integrated circuits, made of Si and GaAs, are not magnetic (figure 2.6.a). The crystal structures of magnetic materials are usually different from that of the semiconductors, so that both materials are incompatible. Ferromagnetic and semiconducting features coexist, for instance, in europium chalcogenides (EuS, EuSe, EuTe) and semiconducting spinels, which have a periodic array of magnetic elements (figure 2.6.b). Unfortunately, their crystal structure is quite different from Si and GaAs, so that they are incompatible with the common electronics. Additionally, their growth is difficult and takes long time (weeks for a small, single crystal) [1].

The properties of semiconductors can be changed by impurity doping as mentioned in chapter 2.1. This approach is followed to introduce as much as possible magnetic elements into nonmagnetic semiconductor to make it magnetic. This class of semiconductors called diluted magnetic semiconductors (DMS) or also referred to as semi magnetic semiconductors (figure 2.6.c), are alloys of nonmagnetic semiconductor and magnetic elements. In general, transition metals (TM) and rare earths (RE) are used, because of their half filled 3d and 4f shells, respectively. These elements have the highest spin magnetic moment according to the Hund's rules. The introduction of magnetic elements is limited by the solubility. The atoms of the magnetic element cannot remain in the crystal at usual growth temperatures of MBE-technique and for high concentrations; they diffuse to the surface and form nanoparticles. The epitaxially growth of DMS by low temperature molecular beam epitaxy (LT-MBE; the principle can be found in chapter 3.2), i.e. the discovery of ferromagnetic DMS in the

pioneering work by Munekata et al. on (In,Mn)As [7], was a major step towards the integration of the spin degrees of freedom with the semiconducting properties in the same material [18]. If the temperature is low, the atoms of magnetic element have not enough thermic energy to diffuse up to the surface and form the so-called second phase (the nanoparticles). The formation of nanoparticles is studied in Chapter 4. The study of DMSs has centred mostly on II-VI semiconductors, which have been difficult to dope getting p- and n-type semiconductors. In 1996 Ohno et al. grew the first ferromagnetic (Ga,Mn)As sample in LT-MBE and proved the ferromagnetism by SQUID measurements [3.21]. The experiments on a similar sample (#M275) grown by LT-MBE in Würzburg at the institute of III-V Heteroepitaxy (Prof. Brunner) are represented in chapter 5.

2.2.1 Crystal structure

Some theoretical aspects of the crystal structures of DMSs are considered on (Ga,Mn)As. The structural features of GaAs samples implanted with other elements are discussed in Chapter 4 separately in corresponding subchapters.

The Mn position in GaAs has influence on carrier type, carrier density, and magnetic features, particularly on the Curie temperature. During the growth of (Ga,Mn)As on GaAs (001) substrate, Mn atoms ideally replace Ga and act as acceptors. This is the so-called substitutional position of Mn (Mn_{Ga}). One Mn_{Ga} contributes one hole. In that case, theoretically the Mn content should be equal to the hole concentration. But experimental results indicate that the hole concentration is substantially lower than the Mn content. The relationship is approximately $p = N_{Mn}/3$ [18]. This is valid for GaAs samples with Mn content in the range of 3-6 %. One reason therefore is the Mn interstitials, which are Mn atoms placed between the lattice points. Erwin et al. explain this mechanism with the density functional theory (DFT): During the growth, Mn atoms follow a simple low-energy pathway to form directly interstitial Mn. Some of these interstitials are converted to substitutionals by additional deposition of As. Interstitial Mn atoms act as donors and each of them compensates two substitutional acceptors. 15 % of the Mn atoms go to interstitial position [20]. This mechanism is called *self-compensation*. Another reason for the reduction of the hole concentration is

the As anti-sites (As_{Ga}), which form during the growth at low temperatures (LT-MBE; 250°C) and act as donors. As_{Ga} also compensates two holes. These defects are relatively stable. It was experimentally shown that to remove these defects annealing temperatures above 450°C are necessary [18]. The (Ga,Mn)As samples in this thesis are grown at usual substrate temperatures of about 600°C and subsequently magnetic ions are implanted. Therefore there are no As_{Ga} defects, which would compensate the holes and that is an advantage of our sample preparation technique. That is very important, because generally it is believed that carriers mediate the ferromagnetism in DMSs [1, 20]. The content of the magnetically active Mn and the hole concentration play a very important role. Decreasing Mn_{Ga} leads to decrease in hole concentration and this leads to a lower Curie temperature. Figure 2.7 shows the three replacements (Mn_{Ga}, Mn_I, As_{Ga}).

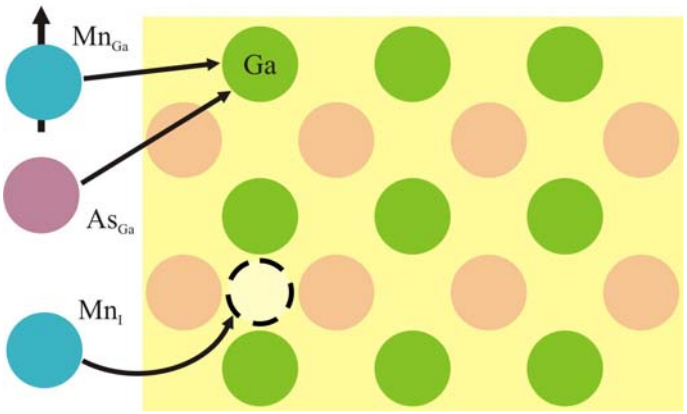

Figure 2.7: *The Mn_{Ga}, Mn_I, and As_{Ga} positions in GaAs crystal is schematically represented.*

The lattice constant *a* of LT-MBE grown (Ga,Mn)As increases linearly with increasing Mn content following *Vegard's law* [1], $a = 0.566nm\ (1-x)+0.598x$. Figure 2.8 shows that linearity clearly according to experimental results. The lattice constant of the hypothetical zinc-blende MnAs extrapolated from the x-ray diffraction experiments on (Ga,Mn)As (0.598 nm) and (In,Mn)As (0.601 nm) are in good agreement [1]. In principle, the lattice constant of MnAs should be in between these values.

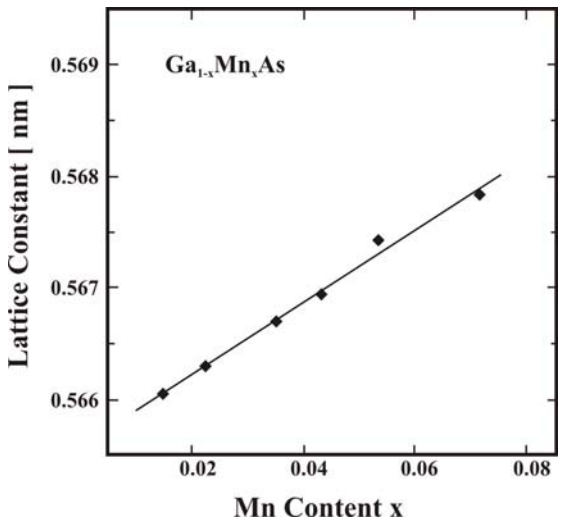

Figure 2.8: *The Lattice constant a increases linearly with Mn content x in (Ga,Mn)As, showing that it follows Vegard's law [19].*

2.2.2 The origin of ferromagnetism in DMS

The question of the origin of the ferromagnetism in DMS is discussed here exemplarily on (Ga,Mn)As, because this is one of the most investigated III-V DMS and the main material in this work. A DMS consists of a nonmagnetic semiconducting host matrix and localised magnetic element atoms distributed statistically in the matrix. The magnetic interaction between localised Mn atoms in the cation sublattice in zinc-blende structure is known to be antiferromagnetic in the absence of holes. This is observed in n-type (In,Mn)As [21] and in fully carrier compensated (Ga,Mn)As [1]. The ferromagnetic interaction responsible for the observed ferromagnetism in (Ga,Mn)As is most likely mediated by carriers. The itinerant conduction band electrons and valence band holes interact with the localised magnetic moments associated with the magnetic atoms. In principle, if 3d TM ions replace the cations of the host, the resultant electronic structure is determined by hybridisation of the 3d orbital of the magnetic ion and mainly the p orbital of the neighbouring anions. This hybridisation leads to a strong magnetic interaction between the localised 3d spins and the carriers in the host valence band [22]. DMS materials have to exhibit ferromagnetism with a transition temperature above RT in order to find practical applications and this is a key issue of the DMS investigation. The Curie temperature of

(Ga,Mn)As has been increased in process of time: It was reported 60 K in 1997 [23] and 110 K in 2001 [24]. Nazmul et al. achieve the highest Curie temperature of 172 K in 2003 by today [25]. The Curie temperature of DMS materials is still a mighty challenge. The ferromagnetic transition temperature can be calculated for a given Mn content x with the empirical equation $T_C = (2000\ x \pm 10)\ K$ [4.8]. For 9 % Mn_{Ga} it would lead maximally to 190 K.

There are several models about the ferromagnetism in DMS materials. (1) The Ruderman-Kittel-Kasuya-Yoshida (RKKY) model and (2) the Zener model are two of them, which are discussed in the following.

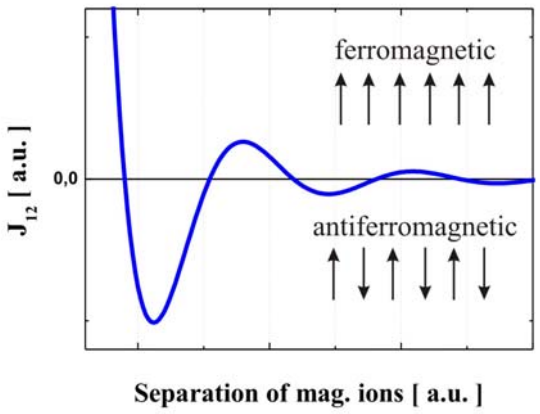

Figure 2.9: *The separation dependent oscillations of the exchange constant is simulated: In the case of $J_{12}>0$ the coupling of magnetic ions is ferromagnetic, for $J_{12}<0$ antiferromagnetic.*

The RKKY model describes the indirect exchange interaction between the localised spin moments of the magnetic atoms (Mn) mediated by itinerant electrons (or holes). There is an electrostatic interaction, while an electron travels through the vicinity of a charged impurity. This ion collects the itinerant electrons and experiences the classical Coulomb-screening. Thus the electrostatic potential of the ion decays faster than r^{-1}. Additionally, there is a quantum mechanical spin-dependent exchange screening due to the Pauli-principle. The electron gas is magnetised in the vicinity of the magnetic ion and the polarisation of that electron gas decays with distance to the magnetic ion in

an oscillatory fashion. The indirect exchange interaction between two magnetic ions oscillates between parallel (ferromagnetic) and anti-parallel (antiferromagnetic) orientation of the moments dependent on the distance of the interacting ions as shown in figure 2.9.

The RKKY interaction of two magnetic ions with spins $\boldsymbol{S_1}$ and $\boldsymbol{S_2}$ can be expressed with Hamiltonian $H_{eff} = J_{12}\boldsymbol{S_1}\boldsymbol{S_2}$. The exchange constant J_{12} is given by

$$J_{12} \propto \frac{\sin(2k_F R) - 2k_F R\cos(2k_F R)}{(2k_F R)^4}, \tag{2.1}$$

where R is the distance between the interacting magnetic ions. The Fermi wave vector k_F depends on the carrier concentration as

$$k_F = (3\pi^2 n)^{1/3}. \tag{2.2}$$

The carrier concentration *n* is written for electrons. For holes, which is the case in (Ga,Mn)As, it should be replaced by hole concentration *p*. The RKKY like interaction is excepted for concentrations lower than 10^{20} cm^{-3} [17, 26]. So the carrier concentration plays a critical role in the RKKY model.

The Zener model, developed by Zener in 1950, describes the ferromagnetism driven by the direct exchange interaction between d shells of the adjacent Mn atoms (super-exchange), leading to an antiferromagnetic order of the d shell spins [22]. Ferromagnetic spin configuration is possible if the indirect coupling of the spins through the conduction electrons dominates over the direct super-exchange coupling between adjacent d shells.

The Zener model does not take care of the delocalisation of mediators (carriers) and the oscillation of spin orientations of the carriers unlike the RKKY model. In the Zener model, the Curie temperature is determined by a competition between the ferromagnetic and antiferromagnetic interactions, $T_C = T_F - T_{AFM}$ and it can be calculated from the normalised ferromagnetic temperature ${}^{nor}T_f$. For detailed description of this model is referred to [27]. The behaviour of this function is drawn in

figure 2.10 dependent on the hole concentration p. The results exhibit a strong dependence of T_C on content of the magnetic ions x and the hole concentration p.

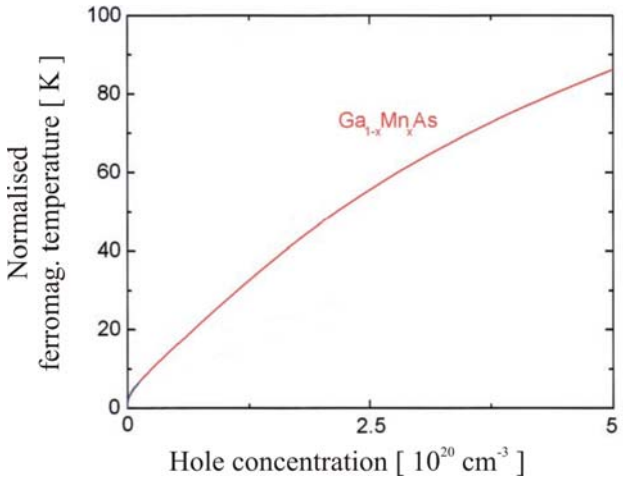

Figure 2.10: *The normalised ferromagnetic temperature is drawn as a function of hole concentration for p-type (Ga,Mn)As [27].*

Still, the prospects for practical applications of DMS in spintronic devices depend crucially on the possibilities to increase the ferromagnetic transition temperature in these materials. The two models, RKKY and Zener model, exhibit that the increase of the transition temperature is associated strongly with the content of the magnetic ions and the concentration of the carriers. The increase in the content of the magnetic ions results in segregation as metallic alloys like GaMn or MnAs, if the content x is too high ($x > 0.10$) and this leads to superparamagnetism (granular ferromagnetism). This kind of material systems is discussed in chapter 2.2.3. An enhanced RKKY interaction leads to higher Curie temperatures, which can be achieved by increase of the carrier concentration.

For details of these models is referred to [22]. The discussion about the origin of the ferromagnetism in DMS materials is not finalised [1, 28]. However, it is sure that the ferromagnetism in DMS and the Curie temperature of these materials are related to the concentration of the carriers and the content of the induced magnetic ions.

2.2.3 Semiconductor - ferromagnetic hybrid structures

As mentioned in the previous chapter, if the epitaxially growth is not favourable energetically due to the high concentration of the magnetic ions, the crystal transits to the minimum energy state by formation of nanoparticles, for instance by segregation as metallic alloys. This is the case, for example, for (Ga,Mn)As as shown in figure 4.8 in chapter 4 for higher substrate temperatures and higher Mn doses. The structures of ferromagnetic nanoparticles embedded in paramagnetic semiconductors are called *semiconductor-ferromagnetic hybrid structures* in the literature and they are currently of interest as potential materials for spintronics as they combine semiconductor properties and Curie temperatures above RT [29].

The size of the nanoparticles and the separation between them play a critical role at the magnetic features of such hybrid materials. When the separation between the small ferromagnetic particles distributed in a nonmagnetic matrix is so large that the interaction between these particles is negligible, the system will behave like a paramagnet while the thermic energy is larger than the anisotropy energy. This is a system of independent groups of moments where each group inside is a ferromagnetic particle (figure 2.11). Therefore the state of this system is called *superparamagnetic*.

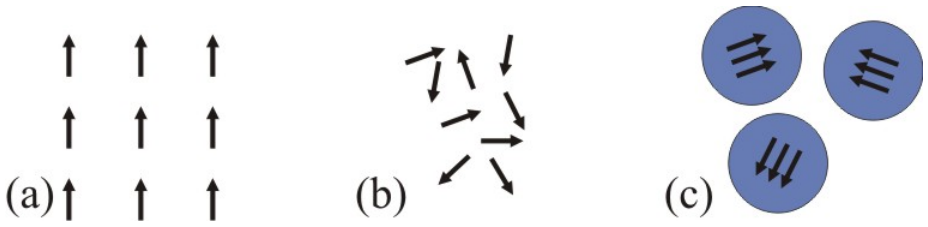

Figure 2.11: *Differences in the arrangement of magnetic moments in a ferromagnet (a), a paramagnet (b) and, a superparamagnet (c) is drawn schematically [30].*

The magnetisation *M(H,T)* of a non-interacting superparamagnetic ensemble of magnetic moments has the character of the classical Langevin behaviour as given in equation 2.3

$$M(H,T) \cong N\mu^2 \frac{H}{3k_B T} \quad \text{for } k_B T >> \mu H \,. \tag{2.3}$$

H is the magnetic field, T the temperature, N the number of the particles, μ the magnetic moment per particle and k_B the Boltzmann constant. According to this relationship, for example, a sample consisting of 10^6 paramagnetic atoms, each with a magnetic moment of $5\mu_B$ has notable different magnetisation $M(H,T)$ than an ensemble of 1000 nanoparticles each containing 1000 paramagnetic atoms. Equation 2.3 yields for the latter case, where the atoms form nanoparticles, of thousand times larger value. At high temperatures the moments on the particles are able to fluctuate rapidly. The relaxation time τ of the moment on a particle is proportional to temperature as

$$\tau = \tau_0 \, e^{\left(\frac{K_{eff} V}{k_B T}\right)}, \tag{2.4}$$

where K_{eff} is the effective magnetic anisotropy density and V is the volume of a magnetic particle.

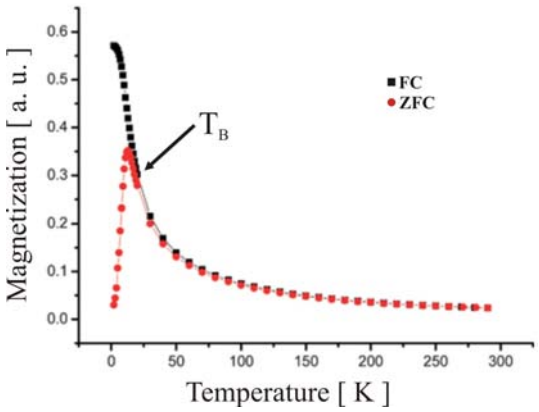

Figure 2.12: *The characteristic magnetisation curve of superparamagnetic state is shown.*

As the sample is cooled, the fluctuations slow down. If the time t of the particular experimental technique becomes much shorter than the relaxation time τ, the system appears static. The temperature at which the relaxation time τ becomes longer than the

laboratory time t is called blocking temperature T_B. The particles in the superparamagnetic system will "block" at different temperatures, if they have different sizes [26]. Temperature-dependent magnetisation (M(T)) measurements allow to distinguish superparamagnetic behaviour from paramagnetic. The characteristic magnetisation curve of a superparamagnet is drawn in figure 2.12.

At high temperatures both of the field-cooling (FC) and zero-field-cooling (ZFC) curves show paramagnetic behaviour. While the temperature decreases under ZFC thermal fluctuations become weaker and the magnetisation increases. At the blocking temperature T_B, below which the magnetic anisotropy dominates, the magnetisation decreases and achieves in the end the small value of paramagnetic state. The system is in the state of the frozen non-interacting magnetic nanoparticles. Subsequently, the magnetisation is measured during heating from low temperatures to high temperatures in a small magnetic field (about 1 mT) and it follows the ZFC curve. While cooling again in the same magnetic field of 1 mT (FC) the magnetisation increases and the system achieve a high magnetisation state where the coupling of the nanoparticles is ferromagnetic. Such a measurement offers a method to distinguish superparamagnetic state from paramagnetic and the blocking temperature can be determined in this way if the present state is superparamagnetic.

Spherical magnetic nanoparticles are paramagnetic materials with a very large magnetic moment, if they have no intrinsic magnetic anisotropy. When the particle size is reduced the surface energy become more and more dominant. Thus, a critical size may be reached below which it is energetically favourable to remove the domain walls so that the particle is a single domain particle. In the strong anisotropy limit the critical diameter can be calculated with equation 2.5

$$d_c \approx 18 \frac{\sqrt{AK_{eff}}}{\mu_0 M_S^2}. \tag{2.5}$$

Here, A is the exchange constant and M_S is the saturation magnetisation. The critical diameter lies in the range of 15-30 nm for typical values of exchange constant and anisotropy constant [30]. In figure 2.13, the possible magnetisation configurations for

small spherical ferromagnetic particles are shown and the corresponding energies of the states are given in equation 2.6.

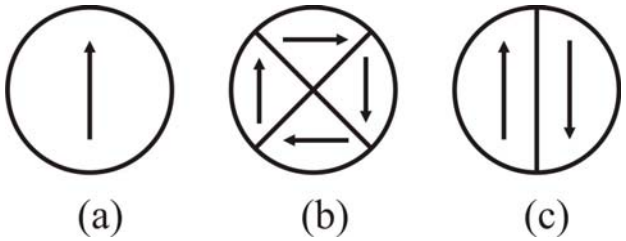

Figure 2.13: *The three possible magnetisation configurations for small spherical ferromagnetic particles are drawn.*

$$E_a = \frac{2}{9}\mu_0 \pi M^2 r^3 \qquad \text{for (a)} \qquad (2.6.a)$$

$$E_b = 2\pi r^2 \sigma_W^{90^\circ} \qquad \text{for (b)} \qquad (2.6.b)$$

$$E_c = \frac{1}{9}\mu_0 \pi M^2 r^3 + \pi r^2 \sigma_W^{180^\circ} \qquad \text{for (c)} \qquad (2.6.c)$$

In equation 2.6.a, b, and c, it is assumed that the critical particle size for removing the domain wall is larger than the domain wall width else it would be nonsensical. The ferromagnetic particles become single-domain particles below the critical size, because the energy cost of domain wall formation does not outweigh any saving in demagnetising energy. Due to the magnetocrytalline or shape anisotropy, the magnetisation vector of a small single-domain ferromagnetic particle is constrained to lie parallel or antiparallel to a particular direction. The energy density of the particle contains a term $K_{eff}sin^2\theta$ where θ is the angle between the magnetisation and this particular direction and K_{eff} is a constant associated with the anisotropy. Thus the energy has minimums at $\theta = 0$ and π. If the particle has the volume V, it needs the energy $\Delta E = K_{eff}V$ to flip from one minimum energy state to the other (from $\theta = 0$ to π or vice versa). The magnetisation can be easily flipped in this way by thermal fluctuations for very small particles (such that $K_{eff}V$ is smaller than k_BT).

2.3 Micromagnetic theory

The fundamental object in magnetism is the magnetic moment that can be equate in classical electromagnetism with a current loop. An electron has (1) an orbital magnetic moment ***m*** and angular momentum ***L*** due to the orbital motion around the nucleus, and (2) a spin magnetic moment associated with the spin motion. The magnetic moment in an atom associated with an orbiting electron is in the same direction with the angular momentum of that electron as given in equation 2.7

$$\vec{m} = \gamma \vec{L} . \tag{2.7}$$

γ is the gyromagnetic ratio defined as (*e/2mc*), which is 1 for purely orbital magnetism and 2 for purely spin magnetism. The ferromagnetic 3d metals have a g-factor of about 2 indicating that the magnetic features of these materials are determined vitally by electron spins. The magnetisation ***M*** of a large number of magnetic atoms in a solid is described as the magnetic moment per unit volume as in equation 2.8

$$\vec{M} = \frac{1}{V} \sum \vec{m}_i . \tag{2.8}$$

The magnetic induction (magnetic flux density) ***B*** relates to the (external) magnetic field ***H*** linearly in free space as described by equation 2.9.a. μ_0 is the permeability of free space. The relation between these vector fields in a magnetic material is described by equation 2.9.b.

$$\vec{B} = \mu_0 \vec{H} \tag{2.9.a}$$

$$\vec{B} = \mu_0 (\vec{H} + \vec{M}) . \tag{2.9.b}$$

In a linear material, the magnetisation ***M*** is connected with the external magnetic field ***H*** linearly, as the name indicates (equation 2.10). The magnetic susceptibility χ is a dimensionless quantity. The connection between the magnetic flux density ***B*** and ***H*** is given by equation 2.10.b in a magnetic material

$$\vec{M} = \chi \vec{H} \tag{2.10.a}$$

$$\vec{B} = \mu_0 (1 + \chi) \vec{H} = \mu_0 \mu_r \vec{H} \,. \tag{2.10.b}$$

$\mu_r = 1 + \chi$ is the relative permeability of the substance. The potential energy E_P of a magnetic moment in a magnetic field $\boldsymbol{H}$ is described by equation 2.11.a. If the magnetic moment lies along the magnetic field, the potential energy E_P is minimized, so that the magnetic moment experience the torque $\boldsymbol{G}$ as defined by equation 2.11.b

$$E_P = -\vec{m} \cdot \vec{H} = -mH \cos\theta \,, \tag{2.11.a}$$

$$\vec{G} = \vec{m} \times \vec{H} \,. \tag{2.11.b}$$

These equations are the fundamental definitions in magnetism and they are valid always, but they don't tell anything about the physical mechanisms of the magnetism. During the crystal formation from single atoms the electronic structure and thereby the magnetic properties are changed. Based on the fundamentals above the mechanisms of magnetism are expressed in the following paragraphs.

An orbiting electron around the nucleus has an orbital magnetic moment and a spin magnetic moment as mentioned above. The material is called paramagnetic, if the total magnetisation of that material becomes stronger due to a weak realignment of the orbital and spin moments by an applied external magnetic field. Paramagnetic materials with unpaired electron spins have a positive susceptibility χ and a permeability of $\mu > 1$. This material group pulls the magnetic flux lines into the substance, so that the magnetisation becomes stronger, for example Aluminium. This kind of contribution of localised (or atomic) magnetic moments to the magnetisation is called *Curie paramagnetism*. At finite temperatures the magnetic moments are distributed statistically due to the thermal motion. The competition of the realignment by an applied magnetic field and the temperature dependent spin disordering determines the paramagnetic contribution to the susceptibility, which is described by the Curie law as given in equation 2.12.a, b and c. χ_0 is the temperature independent

part of the magnetic susceptibility, C the Curie constant, N the number of particles per unit volume, μ_B the Bohr magneton and $J = L \pm S$ the total angular momentum.

$$\chi = \chi_0 + \frac{C}{T} \tag{2.12.a}$$

$$C = \frac{\mu_0 N \mu_{eff}^2}{3k} \tag{2.12.b}$$

$$\mu_{eff} = g\mu_B \sqrt{J(J+1)}\,. \tag{2.12.c}$$

Crystalline solids have energy bands, which are occupied totally at 0 K as mentioned in chapter 2.1, so that the spin magnetic moments of electrons are totally compensated. For band magnetism, i.e. magnetism of delocalised conduction electrons, the conduction band consists of two subbands - one of the spin-up electrons and one of the spin-down electrons (Stoner model) as shown in figure 2.14.b and c. These subbands experience a decrease or increase in energy due to the exchange interaction by an applied magnetic field dependent on the spin orientation. In the stable distribution the number of the electrons parallel to the magnetic field increases and this implies a paramagnetic effect, the so-called *Pauli-paramagnetism*. All element crystals are paramagnetic if they have no electronic redistribution for example in covalent bond, i.e. a bond of electron pairs with saturated spins. The compound semiconductor GaAs is such a covalent bond.

If an external magnetic field is applied and the substance has only paired electron spins, the total spin magnetic moment vanishes. The orbital magnetic moments change because of the Lenz rule so that the external field in substance becomes weaker. This is the *Langevin diamagnetism* and is valid for all materials without exception. Such materials with a negative susceptibility χ and a permeability of $\mu < 1$ are called diamagnetic; they push the magnetic flux lines out of the substance, for instance noble gases. Diamagnetism is induced only by an external field and is temperature independent. The diamagnetic contribution to the susceptibility is always negative because of the Lenz rule.

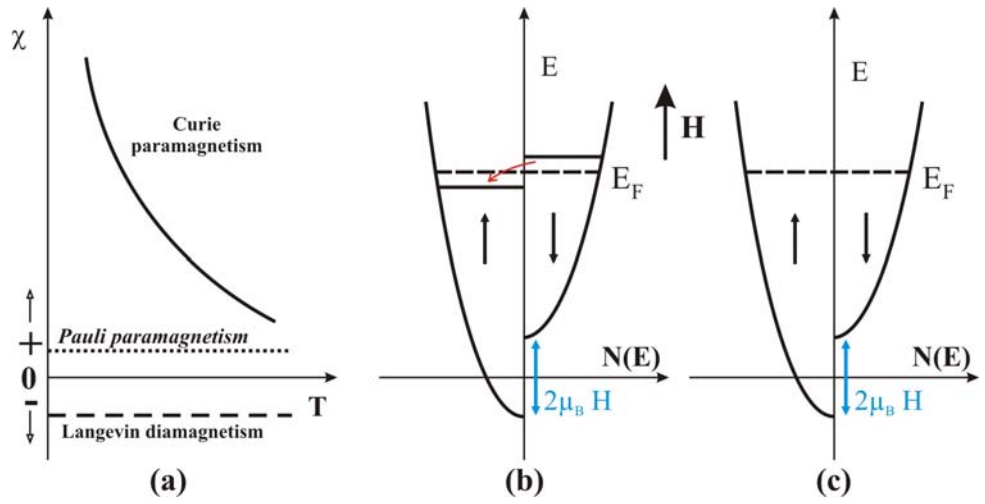

Figure 2.14: *(a) Characteristic susceptibilities of diamagnetic and paramagnetic materials [31]. (b) Before equilibrium and (c) in equilibrium interpretation of the Pauli-paramagnetism by the shift of the subbands in magnetic field* ***H****. E is the sum of kinetic and magnetic energy of the electrons [14].*

Diamagnetism and paramagnetism are weak effects and connected with an external magnetic field. There are other materials with ordered spin structures, which have a relatively large magnetic moment without an external magnetic field. Therefore their magnetisation is called spontaneous magnetisation and this group of materials are denoted as ferromagnetic, antiferromagnetic or ferrimagnetic depending on the configuration of the magnetic moments. The spontaneous magnetisation exists below the transition temperature. The transition temperature is called *Curie temperature* for ferromagnetic and *Néel temperature* for antiferromagnetic materials [14, 31, 32, 33].
The real magnetic materials consist of small magnetic regions, the so-called magnetic domains, in which the local magnetisation is saturated. The transition area, which separates the domains with different magnetisations alignment, is called domain wall. These domain walls contribute to the resistance of the sample at transport measurements. The magnetisation in different domains are not necessarily parallel to each other, it can be polarised in different directions. The realignment of the magnetic moments of a sample by an applied magnetic field can happen through two different independent processes. At lower fields the domain wall motion results in realignment or a rotation of the magnetisation under the influence of a high magnetic field. The

existence of domains results from the character of the magnetisation curve. In a single-domain-state, the system is aligned in a certain direction at positive saturation and is aligned in the opposite direction at negative saturation. At remanence the single-domain-state decays in many small domains. In order to describe the magnetisation processes and calculate the domain structure of ferromagnetic and ferrimagnetic substances, Landau, Lifshitz, and Brown developed the micromagnetic theory.

Micromagnetics and domain theory are based on the following variation principle, which is derived from thermodynamic principles: The vector field of magnetization directions are chosen so that the magnetic free enthalpy G reaches an absolute or relative minimum - the minimum energy principle. G consists of Zeeman energy, stray field energy, exchange energy, and anisotropy energy as given in equation 2.13 [34]

$$G = F_{Zeeman} + F_{Stray} + F_{Exchange} + F_{Anisotropy} \,. \tag{2.13}$$

The Zeeman term represents the interaction energy of the magnetisation vector field $\boldsymbol{M}$ with an external field $\boldsymbol{H}_{External}$. The second term is the free energy of the stray fields generated by the magnetic body itself. The lines of the stray field are going out from the sample at a certain point and return to the sample at another point. This contribution becomes smaller, while the bigger domains decay into smaller domains by introducing of new domain walls. Domain configurations with zero stray field are possible, for instance in Landau-Lifshitz configuration [34]. The free energy term $F_{Exchange}$ represents the exchange interaction between the spin magnetic moments. In magnetic crystals the magnetisation can depend on the direction, so that in order to turn the magnetic moments parallel to certain crystal axes needs larger or smaller magnetic fields (hard-axis and easy-axis, respectively). The work by remagnetisation into the easy axis is minimal and into the hard-axis maximal. The difference of these remagnetisation works is the anisotropy energy and that energy corresponds the difference of the free energy of the initial state and the final state. The anisotropy can occur as crystal anisotropy, magneto elastic anisotropy, shape anisotropy and interface anisotropy, which are summed up in the term $F_{Anisotropy}$ in equation 2.13. These contributions to the magnetic free enthalpy are given in equation 2.14.a to g.

$$F_{Zeeman} = -\mu_0 \, \vec{M}_S \cdot \vec{H}_{external}\,, \tag{2.14.a}$$

$$F_{Stray-Field} = \frac{1}{2}\mu_0 \, \vec{H}^2_{Stray} \quad , \tag{2.14.b}$$

$$F_{Exchange} = J \, S^2 \sum_{i>j} \varphi_{ij}^2 \,, \tag{2.14.c}$$

$$F_{Crystal} = K_1(\alpha_1^2\alpha_2^2 + \alpha_2^2\alpha_3^2 + \alpha_3^2\alpha_1^2) + K_2\alpha_1^2\alpha_2^2\alpha_3^2 \,, \tag{2.14.d}$$

$$F_{MagnetoElastic} = \left(\frac{3}{2}\right)\lambda T \sin^2\theta \,, \tag{2.14.e}$$

$$F_{Shape} = \left(\frac{1}{2}\right)\mu_0 M^2 \cos^2\theta \,, \tag{2.14.f}$$

$$F_{Interface} = \left(\frac{1}{t}\right)(K_S \cos^2\theta + K_P \cos^2\phi) \,, \tag{2.14.g}$$

where μ_0 is the permeability of the free space (equation 2.14.a and b) and $\boldsymbol{M_S}$ the saturation magnetisation. J is the exchange integral and φ the angle between the directions of the interacting spins $\boldsymbol{S}$ (equation 2.14.c). α_1, α_2 and α_3 are the direction cosines of the magnetisation vector referred to the crystal axes. K_1 and K_2 are the anisotropy constants with the unit energy per volume (equation 2.14.d). λ is the isotropic magnetostriction and θ the angle between the tension T and the magnetisation (equation 2.14.e). K_S and K_P are anisotropy constants with the unit energy per area, t the thickness of the magnetic layer and ϕ the angle between the magnetisation and the normal of the interface (equation 2.14.g) [34].

The units of the fundamental physical terms of magnetism used in the literature are summarised in appendix D.

2.4 Theory of electronic transport

Three years after J. J. Thomson's discovery of the electron in 1897, Drude constructed the theory of the electrical and thermal conduction by applying the kinetic theory of gases to a metal. According to this model, a metal is a construct of metallic ions fixed

on the lattice points in a "*free electron gas*" of the valence electrons of the metallic crystal. The assumptions of Drude's theory are the following:

- Electrons collide only by ionic cores and do not interact with anything else.
- Collisions are instantaneous and result in a change of electron velocity.
- Between collisions, electrons do not interact with each other (*independent electron approximation*) or with ionic cores (*free electron approximation*).
- Electrons achieve thermal equilibrium with their surroundings only through these collisions.
- Electrons experience a collision with a probability per unit time $1/\tau$. τ is the relaxation time and τ^{-1} is the scattering rate.

The presence of different crystal defects, such as vacancies, interstitials, and impurities influences the electronic transport in a crystalline conductor. Especially at lower temperatures, the contributions of the resistance from defects or impurities become dominant than thermal contributions. Additionally, phonons excited thermally contribute to the resistance at higher temperatures. With increasing concentration of these defects the probability of the scattering of the electrons increases and so the resistance of the conductor becomes higher. This is taken into account with the relaxation time τ in Drude model.

The approximation of the free electron gas is easily fulfilled in the case of 2DEG, so that the Drude model can be applied for the description of the electronic transport in HEMT structures of semiconductors. In the presence of an electric field $\boldsymbol{E}$ in the plane of a 2DEG an electron acquires a drift velocity v_{Drift} in the time τ between two collisions. The drift velocity can be written as

$$v_{Drift} = \mu_e E \tag{2.15}$$

where μ_e is the electron mobility and depends on the relaxation time τ, $\mu_e = e\,\tau/m_e$. While the electrons move in the conductor they experience a resistance, which is described by Ohm's law: The current I flowing in a conductor is proportional to the potential drop V along the conductor, $V = IR$. R is the resistance and depends on the

dimensions and the resistivity ρ of the conductor. The resistivity is defined as the proportionality constant between the electric field $\boldsymbol{E}$ and the current density $\boldsymbol{j}$, $\boldsymbol{E} = \rho\boldsymbol{j}$. If a uniform current I flows in a conductor of length L and cross-sectional area A, the current density is then $j = I/A$. Thus the resistance of this conductor can be calculated with

$$R = \rho\frac{L}{A}. \tag{2.16}$$

The inverse of the resistivity, which is the Drude conductivity $\sigma = 1/\rho$, allows to write the Ohm's law in terms of current density $\boldsymbol{j}$ and the electric field $\boldsymbol{E}$, $\boldsymbol{j} = \sigma\,\boldsymbol{E}$. Drude model describes the diffusive electronic transport, if the conditions below are valid

$$L >> l_\phi > l_e = v_F\tau \text{ , and } W > l_e. \tag{2.17}$$

L is the typical length in a semiconductor device, W the width of the sample, l_e the elastic mean free path, l_ϕ the inelastic mean free path, l_{ball} the ballistic length and v_F the Fermi velocity. In the diffusive regime the collisions of the electrons with the ionic cores determine the resistance of the sample at RT according to the Ohm's law. The electronic transport is quasi-ballistic if there is no inelastic collision ($L<l_\phi$ and $W \approx l_e$), where the elastic scattering of the electrons at impurity atoms plays an operative role. If $L < l_{ball} < l_e < l_\phi$, i.e. there are only elastic collisions with the boundaries of the conductor, the electronic transport happens in the ballistic regime. The electrons move through the solid body like an optical beam (angle of the incidence = angle of the reflexion). These three transport regimes are represented schematically in figure 2.15. Inelastic mean free path is also called phase coherence length, i.e. after that the phase coherence is destroyed. The sources of the inelastic collisions, which randomise the phase of the electron wave function, are the lattice vibrations (phonons), other electrons or impurity atoms with internal degree of freedom. For instance the spin of a magnetic impurity atom can be flipped by a collision, which causes an inelastic scattering of the electrons.

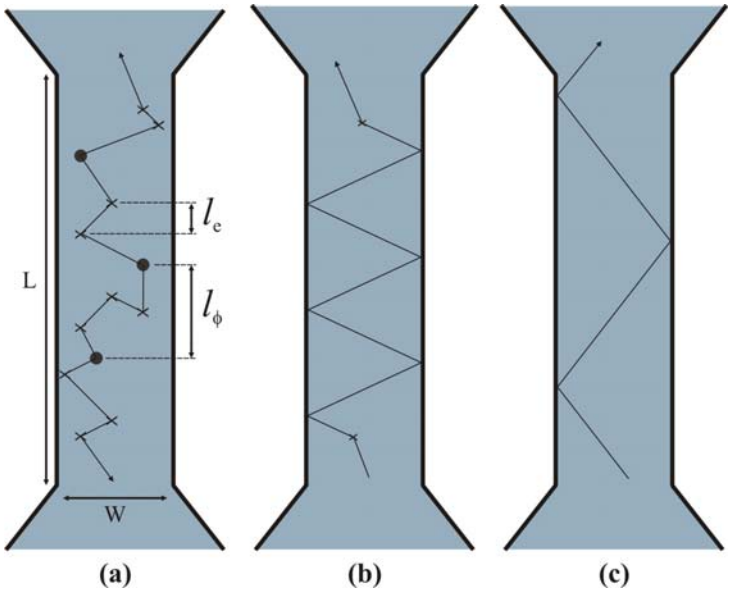

Figure 2.15: *The electronic transport regimes are represented schematically. (a) The collisions of the electrons with ionic cores determine the resistance for the diffusive transport. (b) There are no inelastic collisions, which cause a shift in the phase of the electron wave function, but the elastic collisions with the impurity atoms play an operative role for quasi-ballistic transport. (c) The electrons are scattered elastically only at boundaries and travel through the solid body like an optical beam in the ballistic transport regime.*

For quasi-ballistic and ballistic transports, where l_ϕ becomes larger than L, there is only negligible number of collisions, so that Ohm's law loos the sense. The resistance is not more proportional to the length of the conductor due to the weak localisation effects, a quantum mechanical phenomenon. The conductivity must be calculated quantum mechanically, where the Landauer-Büttiker formalism offers a powerful tool. The spin-dependency of the electronic transport is another important point and is a requisite for the development of the spintronic technology. Transport phenomena based on spin-dependent scattering of electrons in a magnetic field is denoted magnetoresistance effects. The relative magnetoresistance $\Delta\rho/\rho$ is defined as the change of the resistance in magnetic field normalised to the resistance in zero-field as given in equation 2.18 [29]

$$R_{rel} = \frac{R(H) - R(H=0)}{R(H=0)} . \tag{2.18}$$

The classical magnetoresistance effect (MR) is caused by Lorentz force. If a charge moves in a magnetic field, the Lorentz force acts on this charge perpendicular to the plane, which is spanned by the velocity ***v*** and the magnetic field ***B***

$$\vec{F}_L = q(\vec{v} \times \vec{B}) . \tag{2.19}$$

The path length of the charge becomes longer, so that the probability of the scattering increases and thus the resistance increases (positive MR).

An applied magnetic field can destroy the phase coherence, so that the *weak localisation* is destroyed and the MR becomes smaller (negative MR). Theoretically, if the magnetic field configuration gives an advantage to the weak localisation, the MR can increase (positive MR).

If the MR changes depending on the relative orientation of the magnetic moments and the direction of the current in ferromagnetic materials, the effect is called anisotropic MR (AMR). The longitudinal MR is larger than the transversal MR. The magnetic field is parallel to the current for longitudinal configuration and perpendicular for the transversal configuration. The AMR is expressed by the spin-orbit scattering.

The walls of the magnetic domains contribute to the total resistance of the material positively as well as negatively, which is denoted *domain wall resistance* (DWR). If there are domain walls in remanent state and with applied magnetic field they become more, this causes a positive MR. In the other case, if number of the domain walls becomes less with applied field, the MR decreases. The thinner the domain wall the larger the DWR [16, 35].

Chapter 3

Sample preparation and experimental techniques

In this chapter the sample preparation and experimental techniques are presented. The samples grown by molecular beam epitaxy (MBE) are compared with low temperature MBE (LT-MBE) grown samples by means of crystal structure determination. After the sample growth, magnetic ions (Co^{2+}, Dy^{2+}, Gd^{3+}, Mn^{2+}, Tb^{2+}) were implanted into the lattice of the III-V-compound semiconductor GaAs. For that purpose the focused ion beam (FIB) technique was applied, which is introduced in chapter 3.3. In order to study the formation of cluster by segregation of the implanted ions, the samples were annealed. Thermal annealing is known to induce implies the cluster formation and cures the crystal defects, which are produced during ion implantation. The thermal annealing is also used to move the magnetic ions from interstitial site to the gallium site, so that these ions are electrically and magnetically activated. The effect of the position of magnetic ions in the semiconductor lattice is discussed in chapter 2.4. The microstructuring of the samples was done by photolithography details depending on the specific experimental purpose and conditions. In a final step the samples were contacted electrically.

3.1 Molecular beam epitaxy

In order to control the growth of thin crystalline semiconductor layer systems with higher quality both chemical and physical growth techniques are applied. The MBE belongs to the most important physical growth techniques, and enables a control of the layer thickness with an accuracy down to one atomic layer. In MBE the molecular

beam is directed towards a substrate under ultra high vacuum (UHV) conditions. Due to the periodic potential at the substrate surface, the impinging atoms/molecules take over the regular atomic order of the substrate. So the crystal quality of the substrate is transmitted to the growing layer. During the growth different competing processes occur on the substrate surface which are shown schematically in figure 3.1 [36]:

- Adsorption of impinging particles on the surface,
- surface diffusion of adsorped particles,
- incorporation of particles into the crystal lattice (for instance at steps),
- aggregation of nucleation seeds,
- desorption of non-incorporated atoms and molecules.

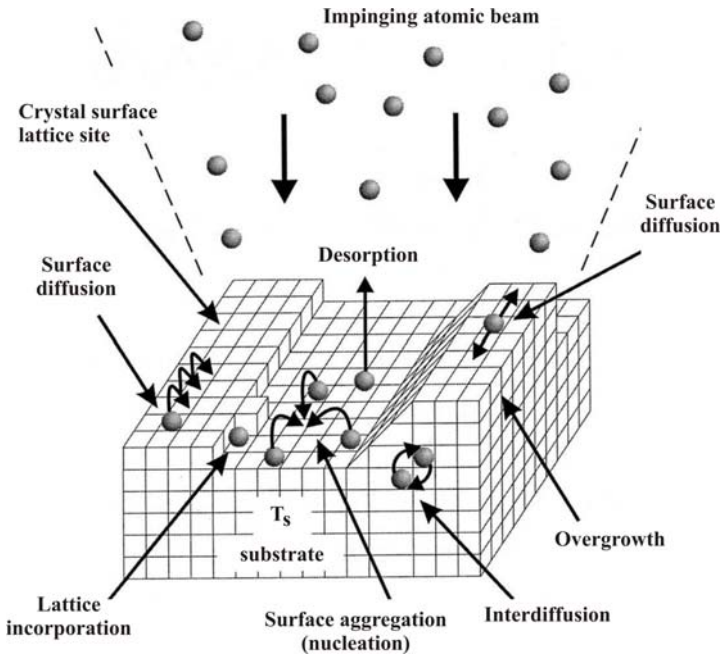

Figure 3.1: *Schematic illustration of the surface processes occurring during film growth by MBE [36].*

In a first step the impinging particles are adsorbed on the surface. In a second step it is possible that the adsorbed particles are desorbed again and are not available for the growth process. The ratio of adsorption and desorption is described by the bonding coefficient which is defined as the ratio of adsorbed particles to the incorporated particles and is inversely proportional to the surface temperature. For an effective

growth process the desorption rate must be smaller than the adsorption rate. For the sample preparation by thermal vaporization, an adequate growth temperature should give a bonding coefficient of close to 1. The diffusion can be described by equation 3.1 [37]

$$D = a\gamma\, e^{\left(-\frac{E_a}{kT}\right)}. \tag{3.1}$$

T is the temperature, a is the lattice parameter of the substrate, k the Boltzmann constant, E_a is the energy to escape from the surface (a kind of energy barrier) and γ is the impinging frequency of an atom at the energy barrier as shown in figure 3.2.

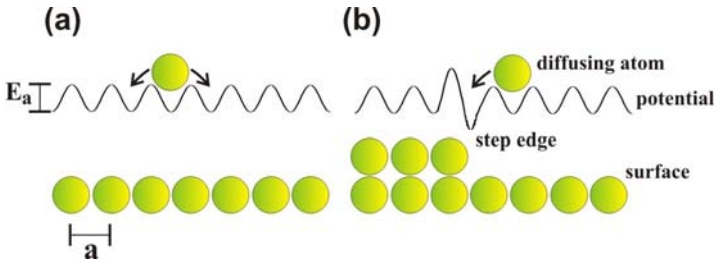

Figure 3.2: *The potential of (a) a smooth surface with energy states and (b) at a step edge with an energy barrier [38].*

The height of the energy barrier determines the mobility of the adsorbents on the surface. With increasing barrier height the probability of the atomic movement on the surface decreases and the probability to move from an energetically favourable state to an energetically non-favourable state is lowered. The aggregation of nucleation seeds is possible only if there are several adsorbents on the adjoining lattice sites. Because of this vicinity the atoms have an additional bond and the strength of this bond determines the stability of the nucleation seeds. If the critical cluster size is achieved, the nucleation seed becomes stable. Thus the nucleation depends on the density of the adsorbents on the surface and on the corresponding particle flow. If nucleation happens at defects of the substrate, it is defined to be an inhomogeneous nucleation,

else it is called homogeneous nucleation. The adsorbents can move freely along step edges, but to escape from the step edges is practically impossible.

The further growth can happen in different modes, depending on the energy of the surface states. In layer by layer growth mode a layer will have start to grow if the previous one is complete, where the step edge of the mono layer moves on the surface uniformly. If the large interaction between the adsorbents governs the growth the Vollmer-Weber growth mode occurs. In the third growth mode the layer-by-layer growth is followed by the Vollmer-Weber mode and it is said to be the Stranski-Krastanov growth mode. These three growth modes are shown schematically in figure 3.3.

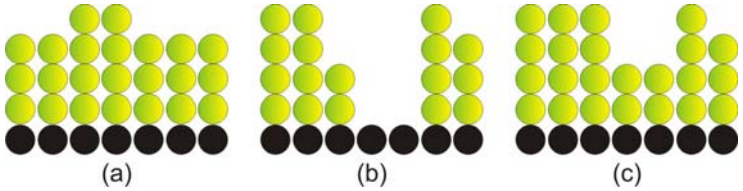

Figure 3.3: *Scheme of the growth mode; (a) layer by layer, (b) Vollmer-Weber and (c) Stranski-Krastanov growth modes [36].*

In the framework of this thesis the samples were grown in a *Riber Epineat* MBE-system on a monocrystalline GaAs (100) substrate with a clean surface. The simplified schematical principle of a III-V-MBE is shown in figure 3.4.

The growth process proceeds under UHV conditions, so that the impurity content of the growing semiconducting layers are minimised and the sample growth with high quality is rendered. In this MBE-system an ion getter pump and a cold trap, which is cooled by liquid nitrogen (77 K), ensure the UHV conditions. With this arrangement it is possible to achieve a base pressure about several 10^{-11} mbar (a rough calculation with the ideal gas equation yields a residual gas density of $< 10^6$ particle/cm^3).

The molecular beam of different elemental materials are created by evaporation in the small cylindrical effusion or so called Knudsen cells (gallium, aluminum and indium from the liquid phase; arsenic, silicon and carbon from the solid phase by sublimation). The doping substances (Si for n-type GaAs and C for p-type GaAs) were

proffered separately as molecular beams to the growing crystal. Spiral heaters adjust the temperature of effusion cells. Only for the carbon cell an electron beam is used. The molecular flow can be adjusted by the temperature. The switching time of the shutters (only the As cell has a valve instead of a shutter) is so short (about 500 ms) that the layer system can be grown with different dopants and chemical composition over a range of few atomic layers continuously without noticeable interruption of the crystal growth.

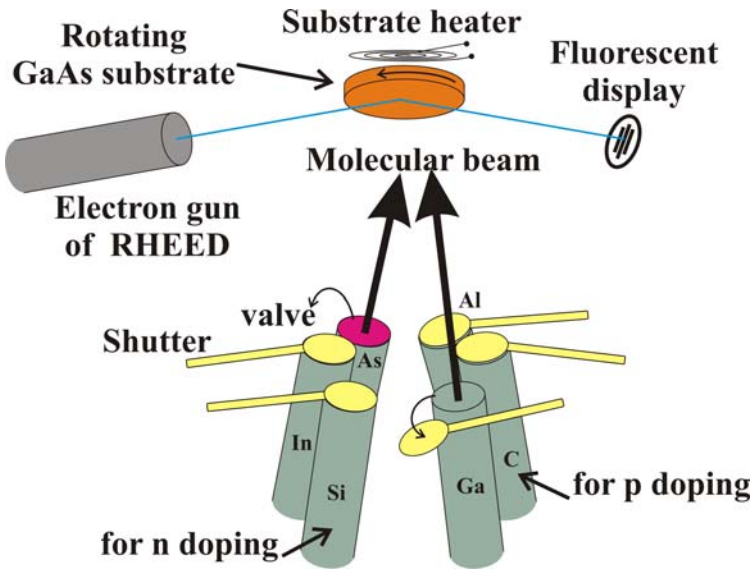

Figure 3.4: *A schematic representation of the growth process in MBE for III-V-compound semiconductors [39].*

During the growth process of the unionised molecular beam the primary elements react with the rotating and hot surface of the substrate, as mentioned at the beginning of this chapter and drawn in figure 3.1. The substrate temperature T_s (~ 590°C) is provided by the substrate heater. At this substrate temperature the impinging atoms and molecules can react with each other and the atoms can ramble fast enough onto their lattice sites, so that no crystal defects can emerge. The growth rate is in the order of 0.7 ML/s, which is defined by the temperature of the cell of group III element (i.e. Ga) in an III-V-MBE system. The group V element (i.e. As) is kept on the surface only by bonding to the free atomic group III element; therefore it has no effect on the growth rate. The

quality of the layers can be examined by in situ reflection high energy electron diffraction (RHEED) measurements [16, 39, 40].

3.2 LT-MBE technique

To overcome the problem of the solubility of magnetic ions in semiconductors, which are mentioned in chapter 2.2, a new growth technique called LT-MBE can be applied. With this method first the semiconducting layers are grown under the MBE conditions, as described in the previous chapter, at a substrate temperature of 600°C – 700°C. After the deposition of the semiconductor (GaAs) the substrate temperature is reduced to 250°C. The magnetic ions (e.g. Mn), which are supposed to make the semiconducting material magnetic, are evaporated together with the semiconductor compounds Ga and As and thus enabling the growth of the diluted magnetic semiconductor (DMS) $Ga_{1-x}Mn_xAs$. This technique enables the epitaxially growth of semiconducting layers with integrated magnetic ions, but has some disadvantages, e.g. the self-compensation problem which is discussed in chapter 2.2. Semiconducting layer systems with integrated magnetic ions can be grown via metal organic (chemical) vapour phase epitaxy (MOVPE) [41] as well.

3.3 Focused ion beam

A focused ion beam (FIB) system consists of three main parts: (1) the ion source, (2) the ion optics column and (3) the beam deflector. The source provides ions, which are accelerated and focused by a system of electrostatic lenses. At the end of the FIB column the ions are deflected electrostatically so that they are impinging the sample at the desired position. FIB systems have the following applications:

- Maskless implantation,
- semiconductor doping,
- creation of isolated regions in electronic structures,
- material sputtering to clean surfaces or to create graves,
- microstructure fabrication by microetching,
- microscopy,
- ion beam lithography.

These systems make it possible implantations over a wide range of doses with a high lateral resolution of a few 10 nm. Some details of the FIB facilities *E-100* from *EIKO Engineering Co. LTD* and *Canion-31* from *Orsay Physics* are shown in figure 3.5.a and b, respectively.

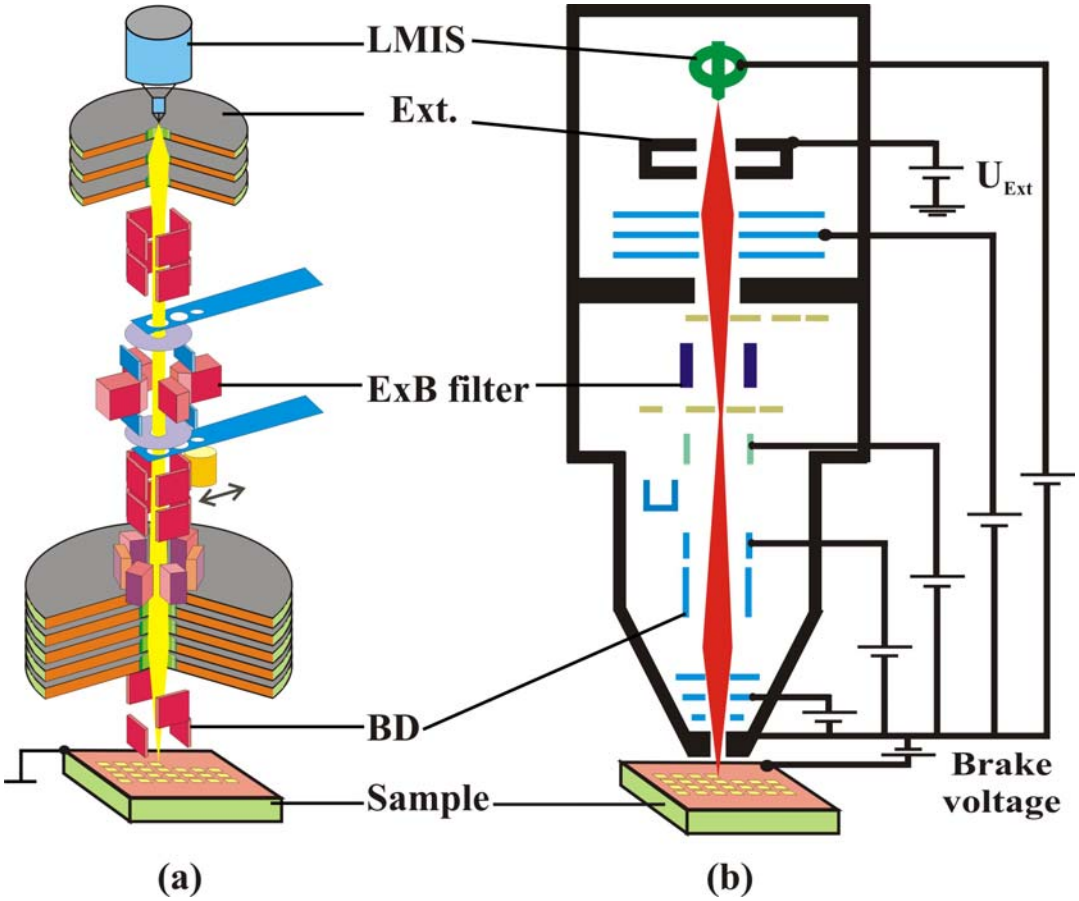

Figure 3.5: *A schematic of the FIB columns. The main parts are the liquit ion source (LMIS), the extraction lens (Ext.), the ExB filter and the beam deflector (BD).*

The ion emitter is a field emission ion source, so called liquid metal ion source (LMIS). A schematic depiction and a real image of LMIS are shown in figure 3.6. It consists of a tungsten needle, a tungsten heater (filament) and a spiral reservoir for an eutectic alloy. The emitter is heated by the filament with a current of about 2 - 3 A to melt the eutectic alloy (GaIn, AuGeMn, CoDy, AuGdSi…) in the spiral reservoir. A high positive voltage (extraction voltage U_{extr}) about 3 - 9 kV is applied to the

extraction electrode. The liquid metal forms the so-called Taylor cone under the influence of electrostatic, hydrodynamic and surface tension forces. The apex of the liquid cone becomes smaller and the liquid metal evaporates. The high electric field provided by the extraction voltage ionizes this vapour (field ionisation) and accelerates these ions towards the extraction electrode. Thus, an ion beam is created which can be processed further in the ion optics column.

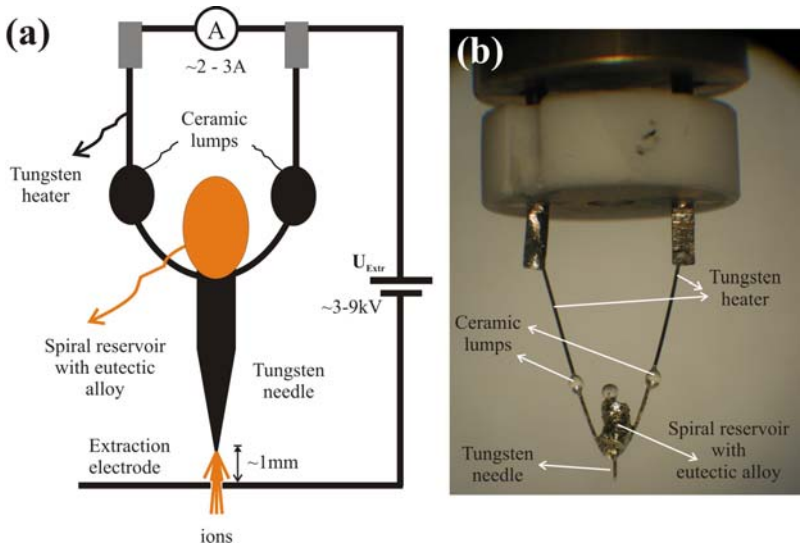

Figure 3.6: *(a) a schematic depiction, (b) a real image of a LMIS [42].*

A suitable alloy system has a low vapour pressure at the working temperature, a low melting point and is practically easy to use, i.e. cheap, non-toxic, etc. Due to the high surface tension the liquid metal can climb up along the filament, which is avoided by two ceramic lumps. The quality of a LMIS is defined by the term *brightness B* that is expressed in equation 3.2. The term d^2I is the differential of emitted ion current flowing into a solid angle $d\Omega$ from a differential area dA. By a good ion source the solid angle and the emitting area should be small so that the quality factor B becomes large [42, 43].

$$B = \frac{d^2 I}{d\Omega \, dA} \quad (\mathrm{A\ cm^{-2}\ sr^{-1}}) \tag{3.2}$$

The ions leave the ion source under the influence of the electrostatic force with different velocities, depending on their degree of ionisation and mass. The decisive ion separation criterion is the *e/m* ratio of an ion at the constant extraction voltage U_{Extr}. Ions with smaller masses and a higher level of ionisation are subject to a higher acceleration so that the ions are separated according to their mass and ionisation degree and they fly with different and constant velocities through the lenses and apertures of the E×B filter. The purpose of E×B filter (also called mass separator or Wien filter) is to extract a special ion species from a beam of a mixture of ions with different axial velocities. The principle sketch of an E×B filter is shown in figure 3.7.

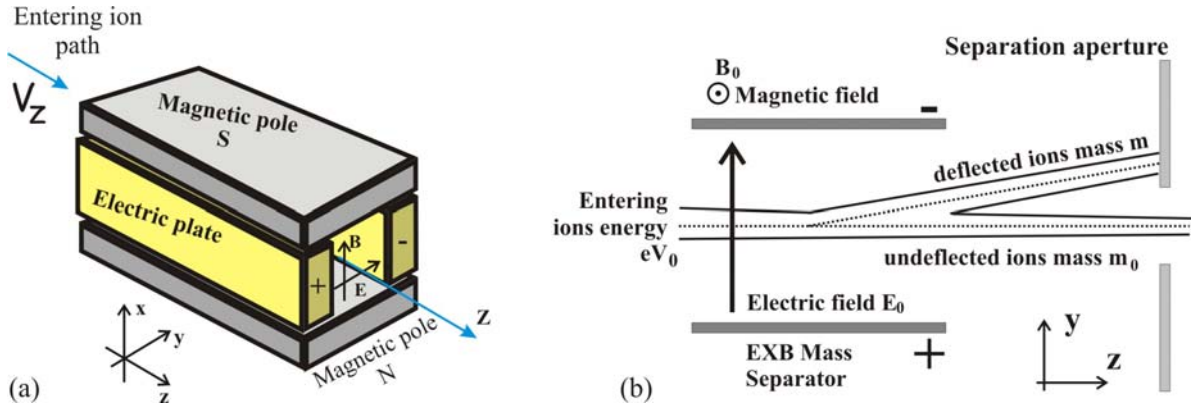

Figure 3.7: *The ExB velocity filter. (a) a perspective schematic of a ExB filter, (b) the schematic of the working principle [44].*

In this arrangement the velocity is perpendicular to the both fields ***E*** and ***B*** so that the electrostatic and the Lorentz forces on a point are in opposite directions. These two forces only compensate each other for the ions with a mass m_0 with a certain velocity $v_0=E_0/B_0$ and only these ions pass the E×B filter undeflected. All others, for which the deflection is larger than the aperture radius, hit separation aperture. Thus, to select a certain ion species the magnetic field is varied at a constant electric field. In this way, our LMIS are characterized and a typical spectrum of a LMIS with the eutectic alloy of AuGeMn is shown in figure 3.8. This E×B arrangement has also a focusing effect on the beam [44]. The ions are collimated onto the sample by a system of electrostatic lenses and apertures with cylindrical symmetry around the optical axis. An

electrostatic lens system consists of metal plates generating electrical fields with a gradient of cylindrical symmetry along the optical axis. This results in a focusing effect for the ions (see for details [45]). With increasing ion density and mass difference between the different ions the ion beam diameter increases due to the Coulomb repulsion and the spatial resolution degrades. The chromatic aberrations (due to the energy spread) and the spherical aberrations (due to the spherical lens surface) are the main limitations to the performance of a FIB column. These aberrations and some other misalignments can be corrected by objective lens alignment, condenser lens alignment and stigmator array. In order to implant desired objects the ion beam can be deflected out of the optical axis and can be blanked into the axis by a pair of electrodes by an electric field in transverse direction to the beam [15, 44].

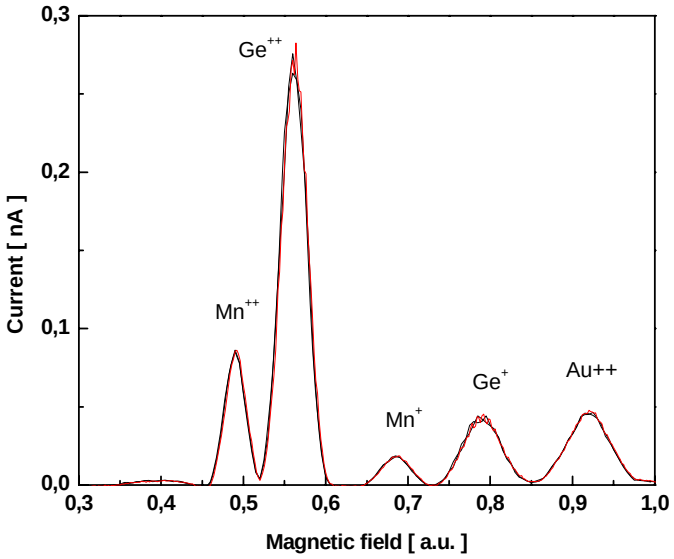

Figure 3.8: *The spectrum of the eutectic alloy AuGeMn [42].*

The MBE and the FIB facilities are combined as shown in figure 3.9 in order to transfer the sample into the FIB processing chamber under UHV conditions, so that the implantation or the deposition can be done on a freshly grown GaAs film with a chemically active clean surface.

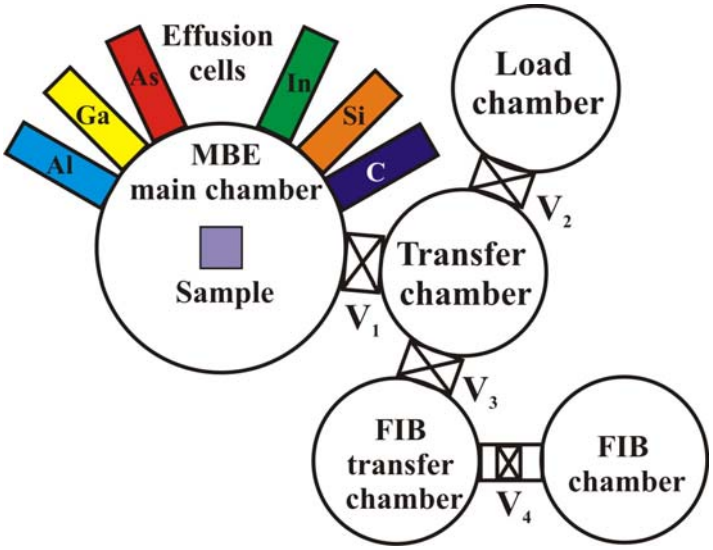

Figure 3.9: *A simple schematic picture of the combined MBE-FIB system with the different chambers and valves* $V_{1\text{-}4}$.

In this FIB system the ions can be slowed down by a brake voltage (see figure 3.5), thus the ions rich the sample surface with a very low energy of about 100 eV. This deposition mode with a very small impact of the ions to the crystal is so called "*soft-landing technique*".

3.4 Rapid thermal annealing

The implantation or deposition of ions on a semiconductor surface usually generates crystal defects. At higher implantation doses and implantation energies the crystal structure can even be completely destroyed and the material can become amorphous. The re-crystallisation and/or electrical activation of the implanted ions as donors or acceptors and magnetic activation is done by a subsequent thermal treatment, called rapid thermal annealing (RTA). By RTA the dopants receive thermal energy so that they can move to the lattice sites by diffusion. Fick's law can express the diffusion process in a semiconductor:

$$\frac{\partial n}{\partial t} = D\frac{\partial^2 n}{\partial r^2} \tag{3.3}$$

Here n is the concentration of the diffusing atoms or molecules, the diffusion constant D is given in equation 3.1. The diffusion process depends linearly on time and exponentially on temperature. Not only the diffusion process itself but, also the kind of the implanted or deposited ions and the kind of the crystal defects play a decisive role in re-crystallisation. The dopants can be bound by impurities or they can form clusters, so that they cannot move to a lattice site. Another effect caused by thermal treatment is the occurrence of secondary defects; such as dislocation lines, areas and loops. These defects are formed due to the aggregation of vacancies and interstitial atoms or anisotropic re-crystallisation of an amorphous crystal segment. The duration of the thermal treatment should optimised so that the implanted ions are activated as donors or acceptors and the primary crystal defects are cured, but secondary defects not yet appear and there is no interdiffusion of layers. Thus, the most important parameters for the RTA are duration and the process temperature. In this thesis annealing time used are of the order of several seconds and the temperature in the range of 700°C – 950°C. The name "*rapid thermal annealing*" comes from the ramping up the temperature from 400°C of the main process temperature to approximately 800°C in few seconds (~ 5 s) and after the treatment ramping down to the starting temperature of 400°C in about 10 s. So RTA is restricted to treat the local primary crystal defects, while the atoms have not enough time to diffuse far away from the defect region. In order to avoid desorbtion of As atoms from the top layers of the sample, an additional GaAs sample is put on the sample with the face down. This is the so-called "*face-to-face*" geometry.
The RTA facility *SHS100* from *AST Elektronik GmbH* uses an optical heating method. It can be used for thin plate samples, which absorb in visible or near infrared wavelength range. The facility allows high heating and cooling rates, temperature control with pyrometer or thermocouple and consistent process cycle repeatability. A simplified schematic of the RTA system is shown in figure 3.10. The main annealing process happens in a quartz reactor chamber, which lies in a water-cooled plated metal block and halogen lamps heat the sample. Because of the small mass of the target object (Si wafer and sample) a rapid heating and cooling is possible. The pyrometric temperature measurement has the advantages that the response time is short, it is executable in contactless mode and it has a high reliability. The sample placed on a Si wafer with a drilled cavity on the backside in which a ceramic thermocouple is

mounted. With this thermocouple the low temperature processes can be controlled or the pyrometer can be calibrated.

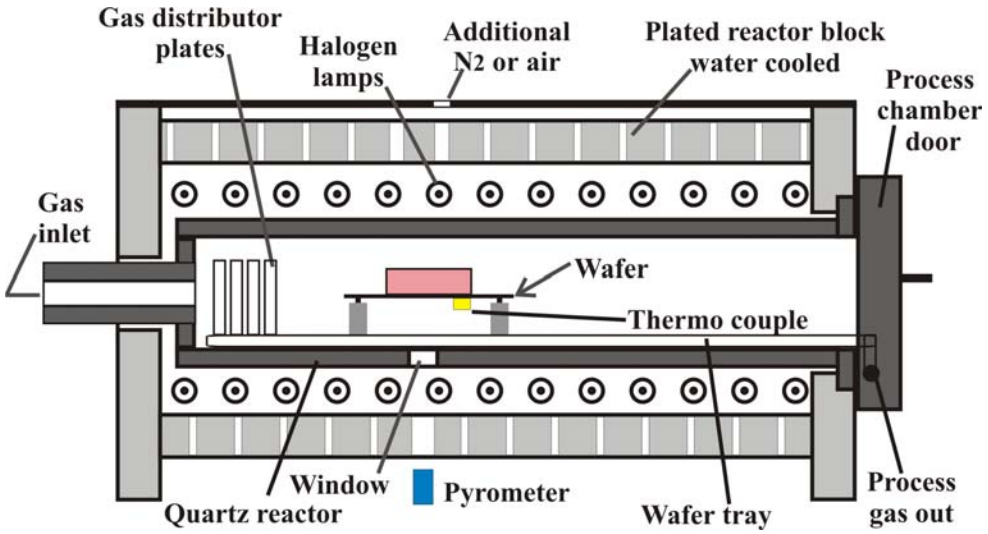

Figure 3.10: *A schematic of the reactor unit of the rapid thermal annealing chamber.*

First the sample chamber is evacuated and is flushed with nitrogen in order to have an oxygen free atmosphere in the reaction chamber, and the chamber is filled with nitrogen during all the thermal treatment process against an oxidation of the sample.

3.5 Photolithography

Before structuring by photolithography, the samples are cut into pieces of 5 x 5 mm^2 lateral size so that they can be glued on a sample holder or to a chip carrier after photolithographical processing. The structures can be transferred to the sample surface by shadow masks with ratio 1:1. The principal of this process is shown in figure 3.11. The photo resist *microposit sp25-10* is spin coated homogeneously on the sample surface with a thickness of few micrometers. Then the photo resist is hardened in an oven at 100°C for 15 min. To expose the resist to UV radiation through the mask an *MJB3* system of *Karl Süss* is used. The exposure time was set to 40 s.

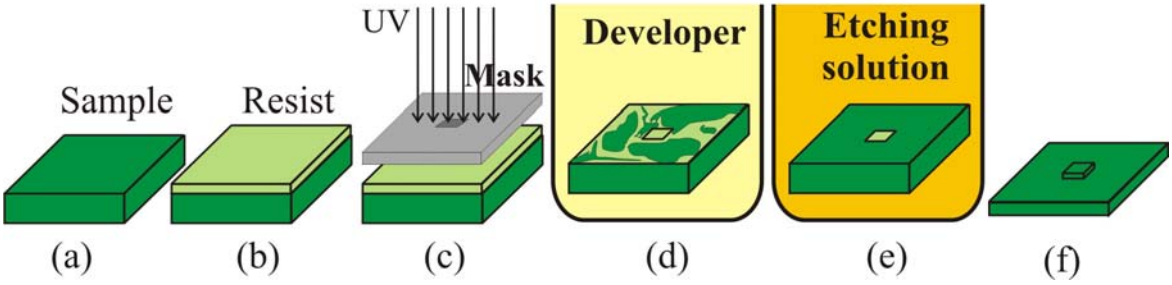

Figure 3.11: *Sample (a), sample with protecting photo resist on top (b), the UV exposure through the mesa mask (c), sample in the developer (d), sample in etching solution (e), and structured sample (f).*

In the framework of this thesis the structures are van der Pauw mesas (mesa is a well defined plane structure like a table with a certain height over the surrounding) and Hall bars. The developer is a sodium hydroxide solution, called *photoposit 160* from the company *Shipley*. To etch the mesa the sample is immersed in a solution of H_2O:H_2O_2:H_2SO_4 (1000:8:1). The etching ratio is 35 nm/min. In order to stop the etching reaction the sample is immersed into water. Finally the resist is removed by acetone and the mesa fabrication process is finished. In order to evaporate ohmic contacts on the structured sample the processing steps above are repeated using the contact mask. At variance with the first lithographic process the surface is covered by two different photoresists. Without the second resist (*microposit LOL2000*) the evaporated metallic contact in the contact window is interconnected with the residual evaporated metallic layer, which must be removed. In this case also the contacts will be removed by the *lift-off* process. The second photo resist interrupts the connection of the contacts and the residual film (see figure 3.12) and thus enables the removal of only the residual metallic layer leaving metallic contacts with sharp edges. The figure 3.12 shows the profile, which is provided by double resist technique. The upper resist is the *microposit sp25-10*, which is also used for the mesa. The lower resist is the *microposit LOL 2000*, which is a cyclopentanone solution. This resist must be hardened at 150°C for 5 min. After the exposure there are windows opened into the two resists. The ohmic contacts are evaporated in these windows in HV chamber (<

$2 \cdot 10^{-6}$ mbar), which is described in the next chapter. The detail steps of the contact processing are shown in figure 3.12.

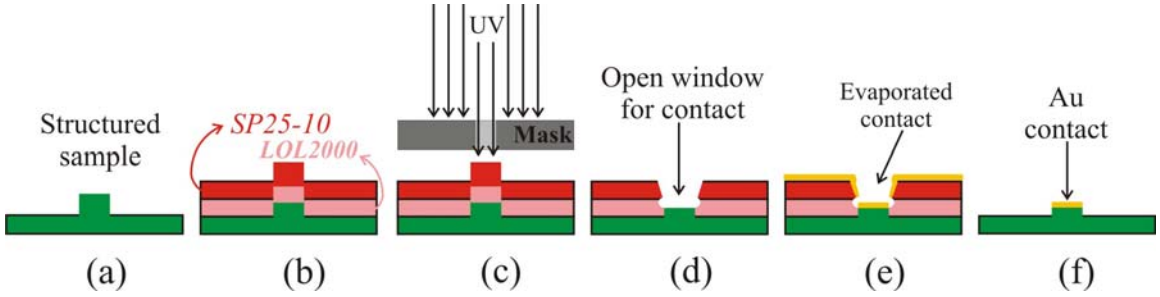

Figure 3.12: *The structured sample (a). The sample is covered with two resists (b), the UV exposure of the sample through the contact mask (c). The sample with a contact window in the two resists after developing (d). After the evaporation of the Au contact (e) and after the lift-off process (f).*

The layouts of the masks, the dimensions of the single van der Pauw and Hall bar structures are depicted schematically in Appendix A.

3.6 Ohmic contacts

A good electrical ohmic connection between the metal contact and the semiconductor should allow carrier transport with little loss of energy across the interface. The primary requirements of ohmic metal/semiconductor contacts are a low specific contact resistance, a negligible diffusion of the metal into the semiconductor, stability at high temperatures and ohmic behaviour without alloying. Ohmic means that the ratio of the voltage drop across the contact and the current flowing through the contact is linear [46].

If a metal contact touches a n-type semiconductor, the chemical potentials of the metal and the semiconductor become equal. Thereby a negative surface charge is collected by thermionic emission on the metal side and the fix ionised donors built up a positive space charge on the semiconductor side of the interface. Due to this space charge the conduction band bends upwardly and provide the junction potential ϕ_B. The amount of

this curvature is $q\phi_B$. This can be calculated using the 3D Poisson equation, which allows the calculation of potentials from charge distributions:

$$\Delta U(\vec{r}) = -\frac{\rho_{el}(\vec{r})}{\varepsilon_0} \quad . \tag{3.4}$$

$U(\mathbf{r})$ is the conduction band profile to be calculated by using Poisson equation, ε_0 is the dielectric constant of free space and ρ_{el} is the carrier density. This bending in potential profile of an n-type semiconductor is illustrated in figure 3.13.a.

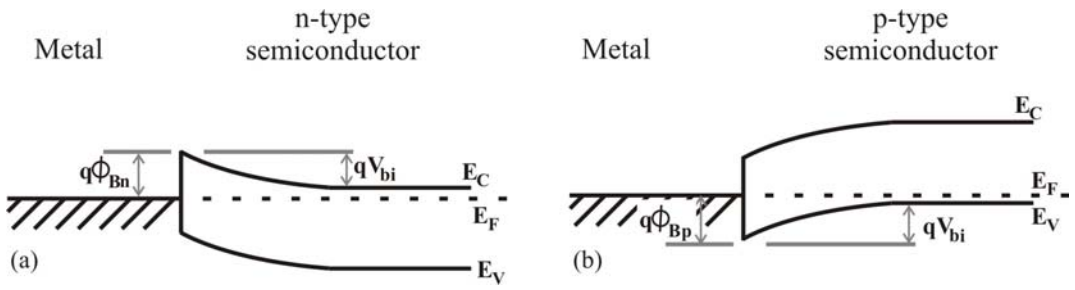

Figure 3.13: *The energy band diagram of a metal-semiconductor junction at thermal equilibrium, a) for n-type and b) for p-type semiconductor [12].*

In a junction between a metal and a p-type semiconductor the electrons diffuse into the semiconductor, recombine with holes in the semiconductor and, a depletion zone builts up for holes and the negative charge of the fix ionised acceptors remains. In this case the conduction band bends downward and provides the junction potential. The bending in conduction band can also be calculated with Poisson equation 3.4. The depletion zone acts as a barrier for the carrier transport (fig. 3.13.b). Both junctions metal/n-type semiconductor and metal/p-type semiconductor are junctions of Schottky type and have no ohmic I-V characteristic [46].

There are three mechanisms governing the current flow through the junction. **(1)** If the depletion zone is relatively wide, the electrons (or holes) cannot tunnel through the depletion zone. In this case, if the height of the barrier is small, the electrons can jump over the barrier by thermionic emission (TE) (figure 3.14.a) and provide an ohmic contact. This is the case for moderately doped semiconductors ($N_d < 10^{17}\ cm^{-3}$). **(2)**

The electrons can tunnel by field emission (FE) from metal to semiconductor through the depletion region, if this is narrow and the contacts are ohmic (fig. 3.14.b). This is the case for heavily doped semiconductors ($N_d > 10^{18}\ cm^{-3}$). **(3)** For intermediate doped semiconductors ($\sim 10^{17}\ cm^{-3} < N_d < \sim 10^{18}\ cm^{-3}$) both the thermionic emission and tunneling (the field emission) are important (figure 3.14.c).

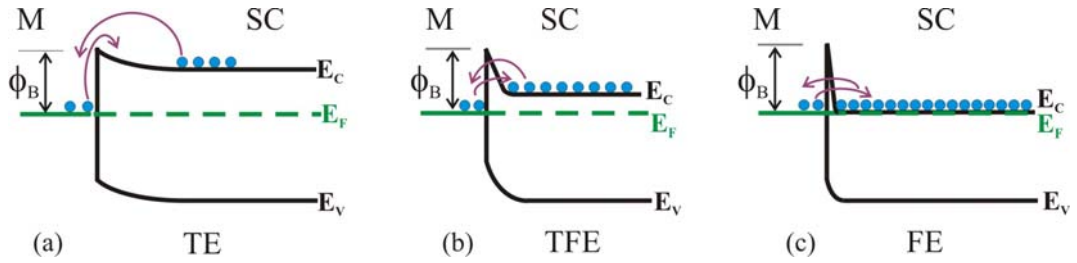

Figure 3.14: *The ohmic contact mechanisms. M means metal and SC semiconductor. (a) Thermionic emission (TE), (b) thermionic-field emission (TFE), and (c) field emission (FE). The scheme is valid also for holes with the corresponding band bending [46].*

Yu and Chang et al. introduced a useful method to define the characteristic of the contacts [47]. The product of measured resistance R_c and the contact area A defines the specific contact resistance ρ_c ($\rho_c = R_C A$) and is given as

$$\rho_c = \left(\frac{\partial J}{\partial V} \right)^{-1}_{v=0} \qquad (\Omega\ \mathrm{cm}^2). \tag{3.5}$$

Here J is the current density and V the voltage. A useful parameter to discuss the three transport mechanisms above is kT/E_{00}. The tunnelling parameter E_{00} is given as

$$E_{00} = \frac{qh}{4\pi} \sqrt{\frac{N_d}{\varepsilon m^*}} \tag{3.6}$$

where q is the electronic charge, h is the Planck's constant, N_d is the donor concentration, ε is the dielectric constant of the semiconductor and m^* is the effective

electron mass. The same equation can be written for a p-type semiconductor if N_d is replaced by acceptor concentration N_a with using the effective hole mass. For moderately doped semiconductors ($kT/E_{00} \gg 1$) the TE mechanism governs the current conduction and the specific contact resistance is proportional as given below

$$\rho_c \propto \exp\left(\frac{q\phi_B}{kT}\right) . \tag{3.7}$$

The specific contact resistance is clearly dependent on the temperature. At higher temperatures the specific contact resistance becomes smaller. For heavily doped semiconductors ($kT/E_{00} \ll 1$) the FE mechanism is the commanding mechanism and ρ_c is given as

$$\rho_c \propto \exp\left(\frac{q\phi_B}{E_{00}}\right) . \tag{3.8}$$

The specific contact resistance depends on the doping concentration. With increasing concentration the depletion width decreases and thus the tunnelling transmission coefficient increases and the contact becomes ohmic [46].

To define the ohmic contacts, for n-type semiconductors the metallic layer sequence in table 3.1 and for p-type semiconductors in table 3.2 are evaporated. The evaporation runs under HV conditions (~ $2 \cdot 10^{-6}$ *mbar*). The elements lie as small pieces of millimetres size in tungsten boats heated by a dc current.

Table 3.1: *The layer sequence for n-type contacts on n-doped GaAs.*

Layer	Element	Thickness [Å]	Growth rate [Å/s]
1	Ni	100	0.6
2	Ge	600	1.5
3	Au	1200	2.1
4	Ni	100	0.6
5	Au	1000	2.0

Table 3.2: *The layer sequence for p-type contacts on p-doped GaAs.*

Layer	Element	Thickness [Å]	Growth rate [Å/s]
1	Au	400	1.2
2	Zn	400	2.0
3	Au	2000	2.4

These as-grown contacts are not ohmic in most cases. In order to use all the advantages of the intrinsic performance of semiconductor devices, the resistance of the contacts must be reduced by alloying at a certain temperature. By the alloying the region just beneath the metallic contacts is highly doped with a component of the contact alloy (with Ge for n-contacts and with Zn for p-contacts) by thermal diffusion thus providing ohmic behaviour.

Summarized, the contact resistivity depends strongly on the doping concentration of the semiconductor, the barrier height of the metal/semiconductor combination, the carrier effective mass, the dielectric constant and the temperature [46].

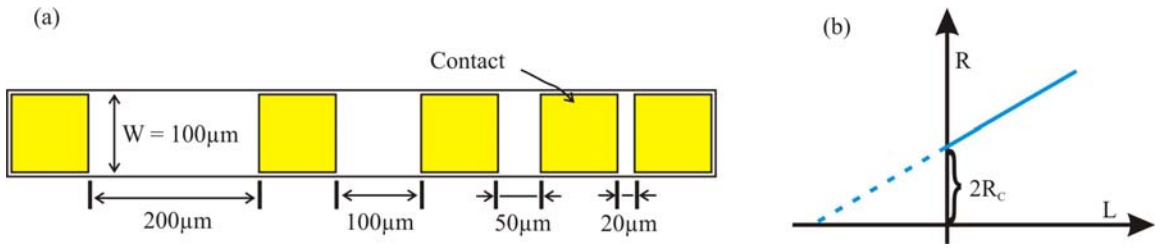

Figure 3.15: *(a) The transmission line, and (b) the resistance R vs gap spacing L.*

The transmission line method (TLM) is used to determine the contact resistance. This method was introduced first by Schokley [46]. A linear array of contacts is fabricated with spacings between them as shown in figure 3.15.a (see also appendix A). The total resistance is equal to twice the contact resistance and the sample resistance; $R=2R_C + (\rho/W)L$. The total resistance is measured as a function of the spacing L between the contacts. To determine the contact resistance the resistance versus gap spacing is extrapolated, this extrapolation crosses the *R-axis* at the value $2R_C$. The sample

resistance is equal to *(ρ/W)L*. From the slope *ρ/W* the specific resistance of the sample can be calculated (figure 3.15.b).

3.7 Hall measurements

To calculate the resistivity of a semiconductor, contact pads in Hall geometry are etched as shown in figure 3.16. The bar width *w* and the length *L* are known. The thickness *d* of the conducting layer corresponds to the penetration depth of the implanted or deposited ions and can be estimated approximately by the simulation program *SRIM*.

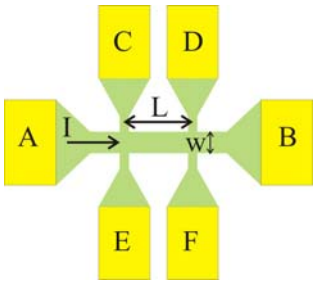

Figure 3.16: *The Hall bar with the length L and the width w. A, B, C, D, E and F are the contacts. I is the current.*

The relatively large contact area reduces the resistance of the ohmic contacts. This bar ensures that the lines of current flow are sufficiently parallel and are not changed on application of a magnetic field. The current *I* flows from contact A to B through the cross sectional area $A = d \cdot w$ and the longitudinal voltage drop is measured between contacts C and D or E and F at zero magnetic field without any current extraction by the measurement probes. The ratio of this voltage drop and the current gives the sample resistance. The longitudinal resistivity ρ_{xx} of the sample can be calculated then with equation 3.9. V_C and V_D are the voltage drops measured from the ground (contact B).

$$\rho_{xx} = \left(\frac{V_C - V_D}{I} \right) \frac{A}{L} \qquad [\Omega m], \quad (B = 0) \qquad (3.9)$$

To determine the carrier density, the carrier type and the mobility a magnetic field *B* is applied normal to the sample plane (B_z, perpendicular to the page plane). The charges sense the Lorentz force $q(\mathbf{V} \times \mathbf{B})$ and a transversal electric field E_y builds up. In

equilibrium the Coulomb force qE_y in the y-direction balances the Lorentz force (equation 3.10.a). The measured voltage drop between C and E or D and F is the Hall voltage V_H and it allows to derive the Hall coefficient R_H (equation 3.10.b) and thus to determine the carrier concentration (electrons or holes) as expressed in equation 3.10.c. n is the electron concentration and for holes it should be replaced with the hole concentration p.

$$qE + q(v \times B) = 0 \tag{3.10.a}$$

$$V_H = -\int E_y dy = R_H \frac{IB_z}{d} \qquad \text{(Hall voltage)} \tag{3.10.b}$$

$$n = \frac{1}{qR_H} \tag{3.10.c}$$

A negative Hall coefficient is an indicator of electron conduction and a positive Hall coefficient of hole conduction. The mobility can be calculated then from the Hall coefficient R_H and resistivity ρ_{xx} or conductivity σ_{xx} using equation 3.11.a. The mean free path can be estimated by equation 3.11.b for 3dimensional and 2dimensonal systems [12, 48]

$$\mu_H = \frac{R_H}{\rho_{xx}} \quad \text{or} \quad \mu_H = R_H \, \sigma_{xx}, \tag{3.11.a}$$

$$\ell_{3D} = \frac{\hbar\mu}{e} \sqrt[3]{\frac{3N_3}{\pi}} \quad \text{and} \quad \ell_{2D} = \frac{\hbar\mu}{e}\sqrt{\frac{N_2}{2\pi}}\,. \tag{3.11.b}$$

3.8 Van der Pauw method

Another method to determine the resistivity, the carrier concentration, the carrier type and the mobility was developed by van der Pauw (1958) [48]. The Hall measurement system *BIORAD*, which is used throughout the present thesis, is based on this van der Pauw method. The sample was cut into squares and the contacts are soldered on the corners or structured by wet chemically etching (appendix A) and contacted by evaporating the layer sequences in table 3.1 or 3.2. Subsequently the contacts are

alloyed to make them ohmic. The resistivities $R_{23,41}$ and $R_{12,34}$ are measured as shown in figure 3.17.a and b, respectively.

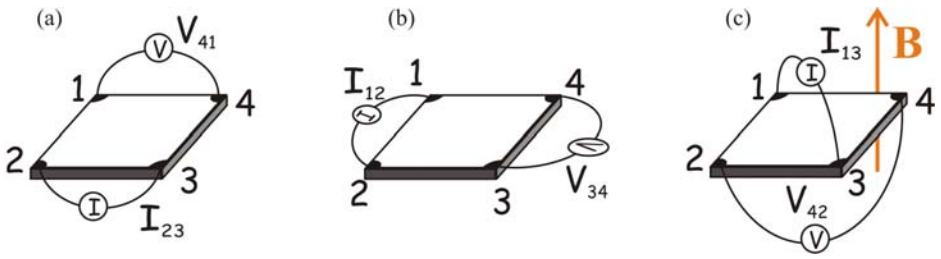

Figure 3.17: *(a) And (b) the resistances are calculated by dividing the voltages by the currents (R=V/I) in van der Pauw setup. (c) The measurement of Hall voltage V_{42}.*

The symmetry factor Q and the correction factor f have to be calculated by equation 3.12 and allow to correct the geometrical error. The sheet resistivity ρ_{sheet} and, if the thickness d of the conducting layer is known, the resistivity ρ can be calculated by equation 3.13

$$Q = \frac{R_{12,34}}{R_{23,41}} \qquad \text{and} \qquad \cos\left(\frac{\ln 2}{f}\left(\frac{Q-1}{Q+1}\right)^2\right) = \frac{1}{2}e^{\left(\frac{\ln 2}{f}\right)}, \tag{3.12}$$

$$\rho_{sheet} = \frac{\pi}{\ln 2}\left(\frac{R_{12,34}+R_{23,41}}{2}\right)f \qquad \text{and} \qquad \rho = \rho_{sheet}d\,. \tag{3.13}$$

A magnetic field is applied to determine the Hall coefficient R_H, in order to derive the carrier concentration from Hall coefficient and the mobility as shown in figure 3.17.c. The Hall voltage U_{42} is measured and the parameters mentioned are calculated as expressed in equation 3.14.a and b (R_{HS} is the sheet resistance)

$$R_{HS} = \frac{1}{2B}\left[R_{13,42}(+B) - R_{13,42}(-B)\right] \qquad \text{and} \qquad R_H = R_{HS}d\,, \tag{3.14.a}$$

$$n_{2D} = \frac{1}{qR_{HS}} \qquad \text{and} \qquad \mu_H = \frac{|R_H|}{\rho} = \frac{|R_{HS}|}{\rho_{sheet}}\,. \tag{3.14.b}$$

The same measurments were done for the other configurations by exchanging the voltage and the current probes [48].

3.9 Magnetotransport experiments

The magnetotransport measurements have been performed between 4.2 K and 300 K using a liquid He bath-cryostat and He-vessel. The magnetotransport geometries are represented by schematic drawings in figure 3.18. For the case of an in-plane current, there are three possible geometries: (1) The in-plane applied magnetic field is parallel (figure 3.18.a) or (2) normal (figure 3.18.b) to the current and (3) the field is normal to the sample plane and so also normal to the flowing current *I* (figure 3.18.c). These three different geometries can be applied in order to define the magnetic anisotropic properties of the sample and obtain the magnetotransport features. From these features some other important parameters like magnetic phase transition temperature can be derived [29]. By these measurements a certain voltage is applied between two electrodes and the corresponding current is measured. The resistance is then calculated by Ohm's law $R=V/I=\rho(L/A)$. The transverse voltage is also measured in order to observe the anomalous Hall effect, which is a clear indicator of ferromagnetism [19, 49].

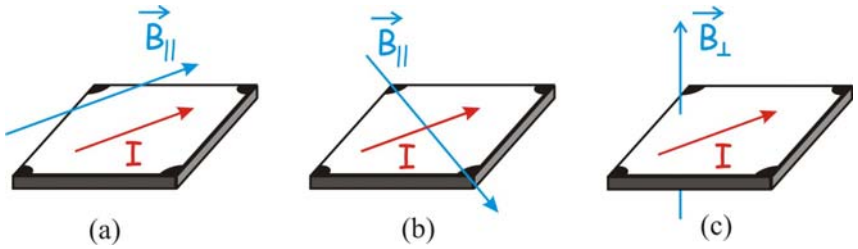

Figure 3.18: *The magnetotransport geometries. The magnetic field is (a) in-plane and parallel to the current, (b) in-plane and normal to the current, (c) out of plane.*

3.10 Temperature measurements

The temperature is measured by a sensor (carbon-glass resistor), which is positioned in close neighbourhood of the sample. The current through this sensor is regulated, so

that the voltage drop is limited to 10 mV. The output voltage on the resistor unit is proportional to the conductivity of the sensor. With this sensor the temperatures can be measured in the range of 4.2 K to 300 K. A disadvantage of this sensor is that the resistivity is magnetic field dependent. In order to solve this problem, the temperature is adjusted to a certain value and stabilized. Then the displayed apparent shift in the temperature was ignored, while the magnetic field is applied.

To stabilize the temperature, the *control height* parameters for the limitation of the heater voltage, *integration time* and *differentiation time* have to be adjusted on the *CryoVac* temperature control unit (*TIC 303 – M*). An additional control parameter for the temperature is the He-flow rate through the sample cavity, which has to be adjusted manually by a valve and can be observed by a flow meter with a resolution of 200 cm^3/min. Thus the time dependence of the temperature shift is observed. As the shift of the temperature was negligible (about ~1 K/h) for the complete time of the experiment, the measurement was started. For the temperature measurements two kinds of sensors are available. For temperatures between 4.2 K and 70 K an *Allen-Bradley* resistor and for higher temperatures between 70 K and 300 K a *PT100* resistor was used. The measurement principle is shown in fig. 3.19. V_W is the voltage drop on the wires 1 and 2, as well 3 and 4. This is subtracted from the complete voltage drop so that the effect of the wires is eliminated.

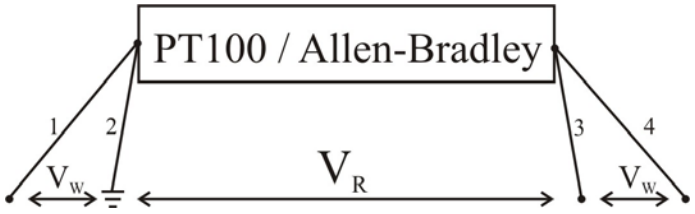

Figure 3.19: *The measurement principle of the resistors PT100 and Allen-Bradley. V_R is the voltage drop on PT100 (Allen-Bradley).*

The achievable magnetic field strength with the solenoid in bath-cryostat is up to 16.987 T (0.1416 T/A). With the solenoid in He-vessel field strength of 6 T (0.09023 T/A) is possible. The superconducting solenoids were cooled by liquid He.

3.11 Scanning electron microscope (SEM)

The sample surface is scanned by a fine focused primary electron beam with energy of 10-50 keV in HV surrounding. The secondary electrons, which are created by the ionisation of the surface atoms, are detected as a function of the instantaneous position on the sample surface. The intensity of the secondary electrons is visualised on a screen. The resolution is limited by the beam diameter and is about 1 to 10 nm. For comparison, the atomic or ionic spacing in solids is in the range of 0.2 to 0.3 nm [50]. A different content or order of the surface atoms changes the work function of the surface and this provides a change in contrast. The information depth depends on the secondary electron energy; lower secondary electron energies give information about upper layers. Also the incidence angle has an influence on the secondary electron emission, so that the coarseness, like breaking flats, can be recognized. The image has a good depth of field for 3D objects, but is only suitable for conducting samples. An insulating sample must be coated with a thin metallic layer to avoid electrical charging of the surface [14].

The figure 3.20 shows a SEM image of Dy^{2+} implanted GaAs sample with an ion energy of 200 keV and a dose of $7.8 \cdot 10^{16}$ cm^{-2}.

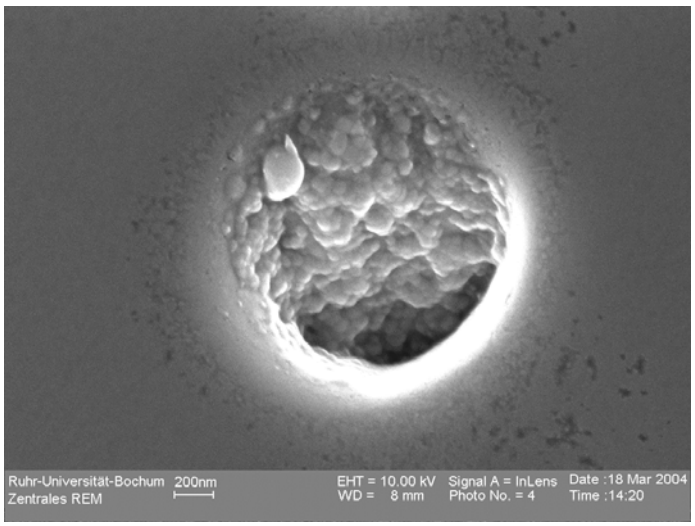

Figure 3.20: *A SEM image of a Dy^{2+} implanted region on GaAs sample. The Dy^{2+} ions have drilled a hole into GaAs (#S100-16) with a diameter of about 1460 nm.*

3.12 Atomic force microscope (AFM)

With the AFM method a tip scans the sample surface. During the sample is driven under the tip, the sample is moved up to the tip or down away from the tip so that the tip to surface distance of about 10 nm is kept constant by a feedback system and thus the tip drives along the surface profile (for details see [51]). A grey scale is assigned to the amount of the sample movement on the dependence of tip location on the surface. The cantilever is bent by the van der Waals forces between the atoms of the sample surface and the tip atoms depending on the spatial separation. A SEM image of the AFM tip and the cantilever are shown in figure 3.21.

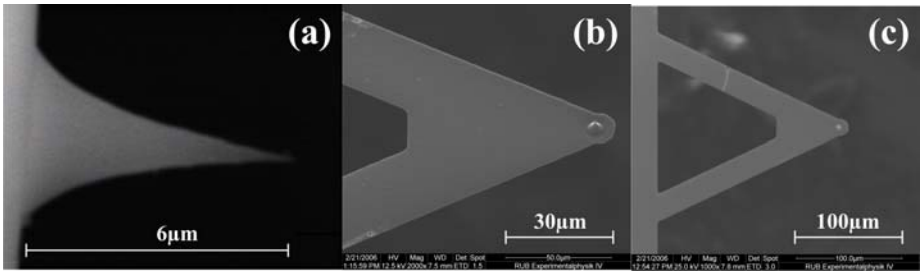

Figure 3.21: *SEM images of (a) the AFM tip, (b) the cantilever with a tip, and (c) the complete cantilever.*

The resolution of the AFM depends on the tip radius and the dihedral angle, which are defined in figure 3.22.

Firgur 3.22: *The definition of the tip radius r and the dihedral angle ϕ.*

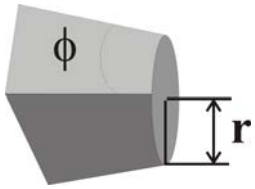

The tip radius is about 10 nm and dihedral angle about 20°. The experimental achievable resolution of the AFM facility of *Park Scientific Instuments*, which is used, is 10 nm.

Two examples for AFM topology images are shown in figure 3.23. The surface of a piece of hard disc sample is shown in figure 3.23.a. The horizontal trace of the reading head is visible. The brighter the grey scales the higher the region. The height difference between the marked points A, B and C are $\Delta H_{AB} = 60\ nm$ and $\Delta H_{BC} = 25\ nm$. The surface of a test sample is shown in figure 3.23.b. This is an array of gold particles on Si substrate with a distance of 1 µm in both directions [51]. The height difference between the points A and B is 25 nm.

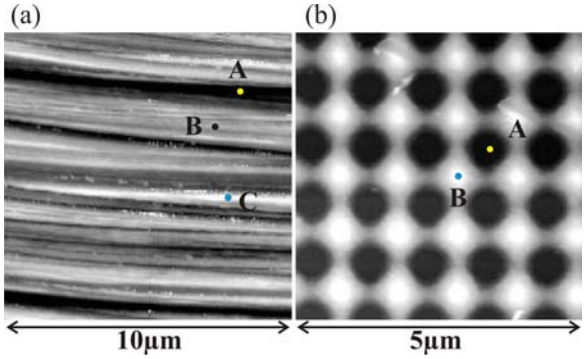

Figure: 3.23: *(a) The topology of a hard disc sample, and (b) the topology of the grating sample; the dark regions are Si and the bright particles are gold [51].*

For a comparison between SEM and AFM, the AFM image of the Dy^{2+} implanted sample (figure 3.20) is shown in figure 3.24. According to the AFM image the defined hole diameter is 1450 nm.

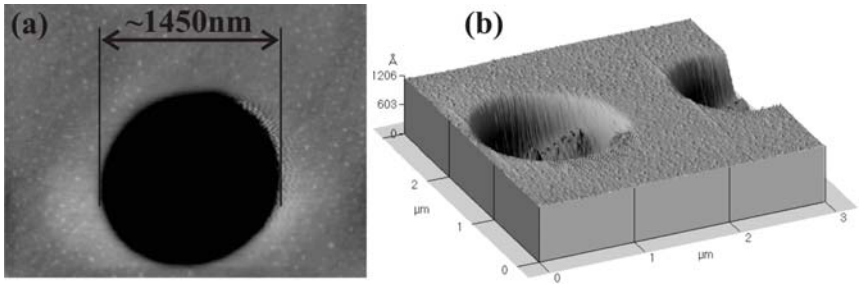

Figure 3.24: *(a) The AFM image of the Dy^{2+} implanted sample (fig. 3.20) and (b) the perspective.*

3.13 Magnetic force microscope (MFM)

Magnetic force microscopy makes the magnetic stray fields visible for magnetic characterisation. This technique is in principle analog to the AFM. However in this case the magnetic forces are registered instead of the van der Waals forces by a tip with magnetic coating. The magnetic coating is a CoCr layer with a thickness of about 50 nm (according to the information of producer).

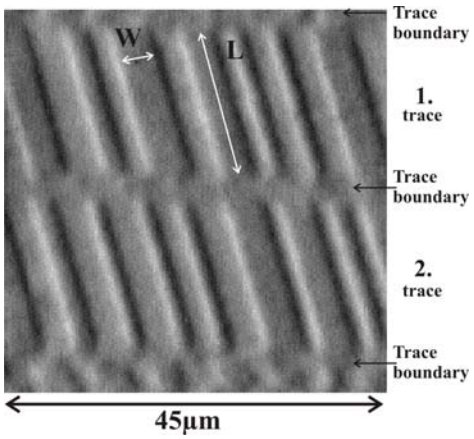

Figure 3.25: *The magnetic image of a hard disc sample [51].*

Figure 3.25 shows the magnetic image of the hard disc sample (figure 3.23.a). Two complete traces can be seen and the third one begins just along the lower edge of the image. The width *W* is in the range of 2 to 5 µm. The length *L* of the traces is approximately 18 µm. The magnetisation within an information unit (*bit*) lies in the sample plane. Where the stray fields point out of the plane a brightening is visible (magnetisation of the tip and the stray fields are parallel; attraction) and they point into the plane in darker regions (magnetisation of the tip and stray fields are antiparallel; repulsion) [51].

The figure 3.26.a shows the AFM image of a Ω-ring. This ring is written with implanted Co^{2+} ions into the HEMT (high electron mobility transistor) sample (for details see appendix C). The radius of this ring is 2.9 µm, the width of the FIB-lines is approximately 422 nm and the height of the FIB-lines is approximately 5.8 nm derived from the topology image. The sample is fed with a voltage of *+9.7 V*.

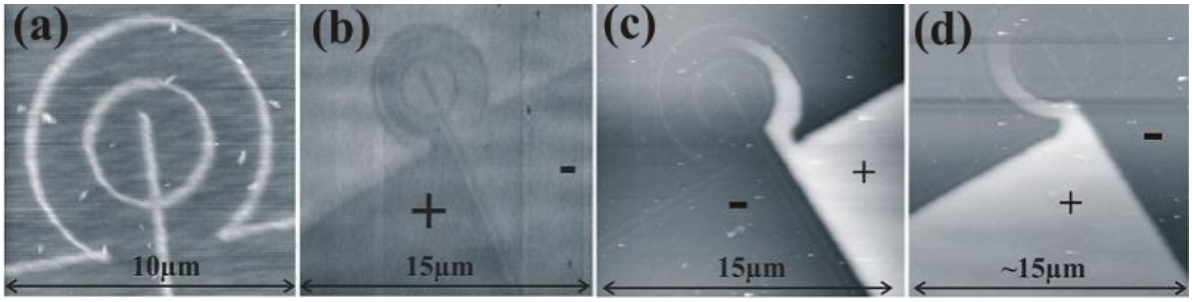

Figure 3.26: *A FIB written Ω-ring; (a) the AFM image, (b) the MFM image, (c) and (d) voltage contrast image observed in AFM mode. (Sample #1127_3d).*

The magnetic fields of this inductive coil are scanned at a height of 36.5 nm with the magnetic tip (figure 3.21.a) driven by a current of 90 µA as shown in figure 3.26.b. The regions where the current flows appear darker, because the current induced magnetic fields attract the magnetic tip and the distance between the tip and the sample is smaller (darker on a grey scale). The figure 3.26.c and 3.26.d show a mixed contrast of the topology signal (induced by van der Waals forces) and electrostatic forces (induced by the recharging of the sample). To check that the visible contrast is really due to the applied voltage the tip is driven to 42 nm height, where the interaction between the tip and the sample is negligible, and the poles of the voltage source are exchanged. Then the tip is lowered down to 36.5 nm and the surface is scanned again. The brighter and darker contrasts are exchanged.

3.14 Energy dispersive x-ray spectroscopy

Energy dispersive x-ray spectroscopy (EDS) is a chemical microanalysis technique performed in conjunction with a SEM. The technique utilizes x-rays that are emitted from the sample during scanning of an electron beam to characterize the elemental composition of the analyzed volume. Structures with a lateral size as small as 1 µm can be analyzed. When the electron beam of the SEM bombards the sample, electrons are ejected from the atoms on the sample surface. An electron from a higher shell fills a resulting electron vacancy, and an x-ray is emitted in order to balance the energy difference between the two electrons. A detector measures the number of emitted x-rays versus their energy. The energy of the x-ray is element specific. A spectrum of the

energy versus relative counts of the detected x-rays is obtained and evaluated for qualitative and quantitative determinations of the elements present in the probed volume.

3.15 Superconducting quantum interference device

A SQUID is a sensitive device available for measuring magnetic fields. The used model MPMS XL does not detect directly the magnetic field from the sample. Instead, the sample moves through a system of superconducting detection coils, which are connected to the SQUID with superconducting wires, allowing the current from the detection coils to inductively couple to the sensor. When properly configured, the electronics unit produces an output voltage, which is strictly proportional to the current flowing in the input coil. Hence, the thin film SQUID device, which is located approximately 11 cm below the magnet inside a superconducting shield, essentially functions as an extremely sensitive current-to-voltage converter.

A measurement is performed by moving a sample through the superconducting detection coils, which are located outside the sample chamber and at the centre of the magnet. As the sample moves through the coils, the magnetic moment of the sample induces an electric current in the detection coils. Because the detection coils, the connecting wires and the input coil form a closed superconducting loop, any change of magnetic flux in the detection coils produces a change in the persistent current in the detection circuit, which is proportional to the change in magnetic flux. Since the SQUID functions as a highly linear current-to-voltage converter, the variations in the current in the detection coils produce corresponding variations in the output voltage which are proportional to the magnetic moment of the sample [52].

Chapter 4

Cluster formation

The material formation mechanisms must be known to determine the standard preparation technique, which is compatible with present material systems and technologies. Some of the well-known and applied material synthesis techniques are (LT-) MBE, MOVPE described in chapter 3, and ion beam synthesis. In order to study the ion implantation by FIB Mn^{2+}, Co^{2+}, and Dy^{2+} ions are implanted into monocrystaline semiinsulating GaAs (100) substrates. Experiments are performed on the samples before and after the thermal treatment to observe the effect of the annealing at different annealing temperatures for different durations. Here, the structural aspects of the ion implantation are considered. In chapter 4.1 the theoretical basics of the stopping mechanisms of the ion beam in the solid body are introduced. The formation of new compounds and their structures are discussed in chapter 4.2.

4.1 Ion implantation

The ion implantation is discussed here according to the ion distribution in the beam and their final distribution in the sample. A focused ion beam consists of a central beam and a tail. The effect of the tail is very important for an implantation without a mask where the charge carrier channels adjoin at the fine isolating implantation lines. This tail can disturb or destroy the desired geometry sharpness of the written structures. The beam diameter can be determined by secondary electron imaging in the FIB chamber. Figure 4.1 shows the sputtered area by a cobalt beam on a GaAs surface, which allows concluding that the diameter of the beam is about 170 nm. The focusing

of the ion beam to a diameter of less than 100 nm is possible, but for an exhaustive implantation of a complete area a finer focusing of the beam is not necessary.

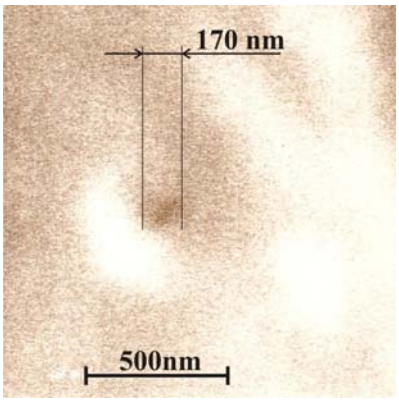

Figure 4.1: *The secondary electron image of the area on a GaAs surface sputtered by the Co^{2+} beam exhibits a diameter of about 170 nm. The implantation dose was $7.7 \cdot 10^{16}$ ions/cm^2.*

In chapter 3.3 the deleterious effect of the Coulomb repulsion among the ions on the beam profile was mentioned. The inter-ion spacing is fairly small at some positions in the beam throughout the column, causing the ions to interact significantly enough by Coulomb force. Because of the statistical nature of these beam interactions, the effects on a large number of ions must be ascertained, where statistical methods are necessary, like Monte-Carlo simulations. The Coulomb interaction is significant near the source where typically microamperes of current are emitted from an area with about 100 Å diameters. It is also significant in the focusing column, where the total current is less, but there is a much longer way over which interactions can occur [53]. Ward and Seliger did the first Monte-Carlo investigation of the Coulomb interaction in the ion beam in 1981 at the *Hughes Research Laboratories* and they have observed the "beam halo" effect [53]. The longer the exposure the broader is the "halo". Figure 4.2 shows an AFM image of a manganese implanted square area. The halo effect of the tail dose can be seen around the square area. The width of the "halo region" averaged over the four positions marked with arrows is 1.7 μm. But it is not a disturbing effect in our case, because the goal is to implant exhaustive as mentioned above.

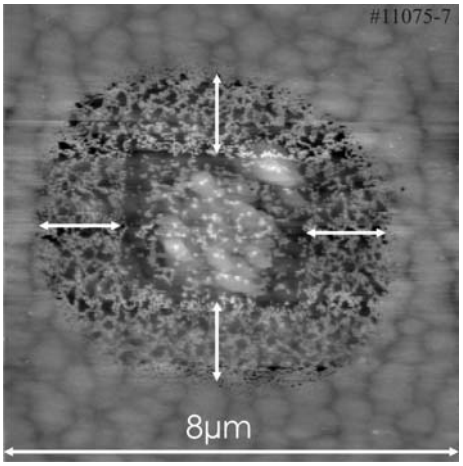

Figure 4.2: *The halo effect caused by the tail dose appeared around the square area implanted by twofold ionised Mn atoms. Implantation was done into GaAs with a dose of about* $2.9 \cdot 10^{14}$ *ion/cm*^{2}.

The ion distribution in the beam can be described with a Gauss function as written in equation 4.1

$$n(r,\sigma) = \frac{N_0}{2\pi\sigma^2} e^{-\frac{r^2}{2\sigma^2}}. \tag{4.1}$$

Here, N_0 is the number of the ions implanted in the target and σ the standard deviation. The beam diameter is equal to the full width at half maximum (FWHM) of the distribution curve given for the Gauss function by equation 4.2

$$FWHM = 2\sqrt{2\ln 2}\,\sigma \cong 2.3548\,\sigma. \tag{4.2}$$

The area under the distribution function gives the number of the ions in the beam. The function is integrated from $x = -1.2\sigma$ to $x = 1.2\sigma$ to get the part of the ions in the main beam. For this calculation the FWHM is defined as the width of the curve at $f(x) = 0.5$ ($f(x) = n(r,\sigma)$). Thus 75 % of the ions are in the main beam and the residual part is in the tail of the beam as simulated in figure 4.3.

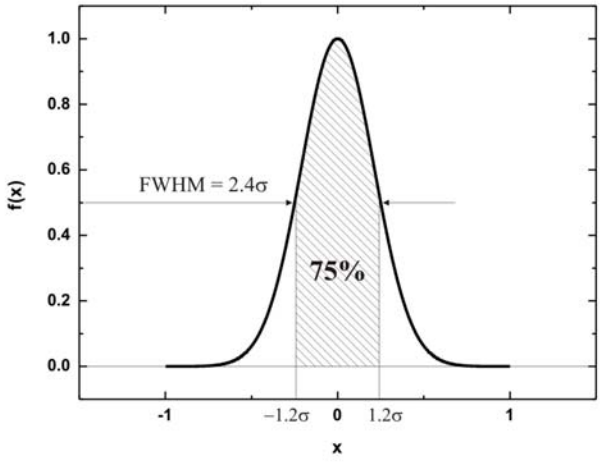

Figure 4.3: *The ion distribution in the beam can be described by Gauss function. 75 % of the ions are in the main beam and the residual part is in the tail.*

In order to determine the final distribution of the ions in the crystal structure, one must know what happens if energetic particles impinge and travel through the crystal. There are relatively small numbers of physical processes in the interaction of the ion beam with a solid. These processes determine also what can be done with the beam. The incident ions can displace the target atoms. This can occur in such a way that a number of useful phenomena arise which can be utilised in making, breaking, and altering structures on a very small scale. Figure 4.4 illustrates the possible interactions of the incident ion beam in a solid sample. These processes do not occur with equal probability. The interactions can be considered basically in two classes as listed below. The elastic interactions are

- surface sputtering,
- displacement of lattice atoms,
- formation of defects.

For elastic impacts the total energy and the total momentum of the system are conserved, where an exchange between kinetic and potential energy happens. The inelastic processes, which change the inner energy by excitation and ionisation, are

- secondary electron emission,

- x-ray emission,
- optical photon emission.

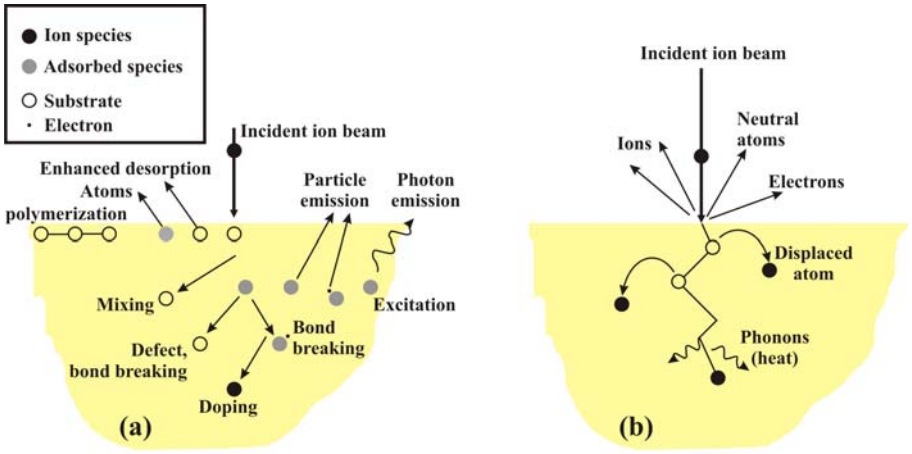

Figure 4.4: *Two views of possible processes initiated by an ion implantation are represented schematically [53].*

Depending on the energy and the mass of the colliding particles elastic or inelastic energy exchange proceeds. An important process is the sputtering of substrate atoms from the sample, where the resulting effect of this process can be imaged by the simultaneously releasing electrons. Another process is the displacement of the target atoms from their lattice sites by the prevalent elastic nuclear collisions. Depending on their energy these atoms can displace other lattice atoms, so that a cascade of displaced atoms accrues. The experimentally determined displacement energies E_d of gallium and arsenic atoms in GaAs-crystal are 8.8 eV and 10.1 eV, respectively [54]. If the incident ion has a kinetic energy of larger than $2E_d$ both the projectile ion and the displaced lattice atom have a kinetic energy of larger than E_d, and both can contribute to the cascade. Thus the maximal number of vacancies N_{max} per incident ion with the energy E_0 can be given by equation 4.3 [55]

$$N_{\max} = \frac{E_0}{2E_d}. \tag{4.3}$$

For the mean displacement energy of 9.5 eV, averaged over the displacement energies of Ga and As atoms in GaAs crystal, a Mn ion with an energy of 200 keV is able to move maximally $1 \cdot 10^4$ crystal atoms. Due to the momentum transfer also dislocations and rearrangements can occur. These rearrangements can generate crystal defects and/or can result in amorphization of the crystal. The generation of the crystal defects, which must be annealed subsequently, is the disadvantage of the ion implantation technique. In order to avoid very high concentration of crystal defects the implantation can be done at a certain substrate temperature, which is called *hot implantation*. Another technique is the deposition in *soft-landing mode*, where an inversely polarised voltage slows the impinging ions down. The ion implantation is a non-equilibrium process. When chemical reactions of the incident ions with surface atoms take place the rearrangement can cause chemical sputtering which results in forming new chemical phases. Their properties differ from the chemical phases, which appear in thermodynamic equilibrium. That is a modification of the host crystal structure and formation of clusters or nanoparticles with different crystal structures. The details of this process and the results are represented in chapter 4.2. This process is considered here to study the crystal structure and the magnetic features of new compounds. Ion implantation can also be used to dope semiconductors to adjust the electrical conductivity. Due to the elastic impacts with bound electrons of the target atoms the projectile undergoes a minimal change in the flight direction.

If the incident ions lose all their energy and become trapped in the solid, implantation has occurred. This has practical uses in the production and modification of semiconductor devices [53]. The application in this thesis is the doping of GaAs and integration of magnetic ions into GaAs to make it magnetic. So the fundamental quantity of interest is the mechanism of energy loss by which the incident ions transfer energy to the crystal. As ions are stopped by collisions with ionic cores in the crystal, they lose energy in two main ways: nuclear and electronic collisions [53].

4.1.1 Energy loss by nuclear collisions

In general, the collision kinematics can be calculated from the interatomic potentials and finally made a detailed calculation of hundreds of interatomic potentials using

modern solid-state atomic models. These models are represented very well in [56]. The calculations reduce the problem to a single analytic function, which is called a *universal interatomic potential*. This potential function can be applied to generate new universal nuclear stopping cross-section and scattering functions, which can be used to calculate the physics of ion penetration in solids. The classical transfer of energy between a moving and a stationary charged particle depends only on the mass and charge of the two particles, and the moving particle's initial speed and direction. While the moving particle passes, the stationary particle recoils and absorbs energy. The moving particle is deflected. The final velocities and trajectories can be found simply from the conservation of total momentum and energy of the system. A part of the kinetic energy of the implanted ions is transmitted to the target atoms. They take over an appreciable momentum. This leads to deflection of the projectile and displacement of the target atom from the original lattice site in the crystal.

Nuclear energy loss occurs in the collisions between the screened nuclear charges of impinging ions and the atoms in the target crystal. At low energies (from several eV to several 100 eV) the interaction is very complex. The interactions at medium energies (1 keV - 500 keV) can be described by screened Coulomb scattering. The implantation energies in chapter 4 lie in this energy range, thus the considerations below base on this thought. The interaction mechanism based mostly on the Rutherford scattering at high energies (MeV).

The nuclear energy loss mechanisms are all expected to be due to elastic two-body collisions. In the laboratory system, the energy T of an atom M_2 initially at rest is given by equation 4.4 based on the conservation of energy, momentum and charge

$$T = E_0 \frac{4M_1M_2}{(M_1 + M_2)^2} \cos^2 \phi \,. \tag{4.4}$$

Here, E_0 is the energy of the incident ion of mass M_1 and ϕ the recoil angle of the atom of mass M_2. Equation 4.5 gives the maximum energy transfer

$$T_{\max} = \frac{4M_1M_2}{(M_1 + M_2)^2} E_0 \,. \tag{4.5}$$

Thus equivalent to equation 4.4 can be written $T = T_{max} \cos^2\phi$. This equation can be rewritten in the form $T = T_{max} \sin^2(\theta/2)$ in the centre-of-mass system, where the total momentum is zero. θ is the scattering angle in the centre-of-mass system. In order to calculate a cross section, which gives the probability for the scattering of an ion into a certain angle θ, in the centre-of-mass system, an interaction potential must be submitted. For the case of reasonably heavy ions and not extremely high velocities, the ions experience repulsion while the electron cloud of the projectile and target atoms are close to each other. The electron cloud screen the nucleus from each other, thus a kind of screened Coulomb potential can describe this case. The Thomas-Fermi potential is a good approximation for such a potential

$$V(R) = \frac{Z_1 Z_2 e^2}{R}\left(\frac{R}{a}\right)\phi_0 . \tag{4.6}$$

$$a = 0.468\,(Z_1^{2/3} + Z_2^{2/3})^{-\frac{1}{2}} . \tag{4.7}$$

Here, Z_1 and Z_2 are atomic numbers, and a the Thomas-Fermi screening radius given in equation 4.7. ϕ_0 is a function of a and R. In order to simplifying the calculations two dimensionless parameters, the reduced path length ρ and the reduced energy ε, are introduced. Thus the number of the parameters, which are necessary to describe the interactions, is reduced from five to one: $t = \varepsilon^2 \sin^2(\theta/2)$. The reduced path length ρ is given by

$$\rho = n\pi a^2 \gamma x \qquad \text{(Atoms/cm}^3\text{)} \tag{4.8}$$

and the reduced energy ε by

$$\varepsilon = \frac{32.53\, M_2 E}{Z_1 Z_2 (Z_1^{2/3} + Z_2^{2/3})^{1/2} (M_1 + M_2)} \quad \text{(E in keV).} \tag{4.9}$$

Here, n is the atomic density of the target (atoms/cm^3), x the path length, E the energy in *keV* and γ the mass ratio given by equation 4.10

$$\gamma = \frac{4M_1M_2}{(M_1+M_2)^2}. \tag{4.10}$$

The nuclear energy loss or the stopping power dE/dx is proportional to the integral of the energy transfer over the energy transfer cross-section $d\sigma$

$$\frac{dE}{dx} = -n\int_{\sigma(0)}^{\sigma(E_{max})} E\, d\sigma = -nS_n(E). \tag{4.11}$$

Here $S_n\,(E)$ is the nuclear stopping cross-section and can be written in dimensionless units in the form $d\varepsilon / dr = -s_n\,(\varepsilon)$. $S_n\,(E)$ and $s_n\,(\varepsilon)$ are connected by equation 4.12

$$S_n(E)\,[eVcm^2] = \frac{s_n(\varepsilon)\,E[eV]}{\varepsilon}\,\frac{\rho}{x}\,\frac{1}{n}. \tag{4.12}$$

4.1.2 Energy loss by electronic collisions

The bound electrons of the target atoms (and as well the free electrons in the crystal) are excited or released by the inelastic electronic collisions with the incident ions. The ions interact with electrons of the target atoms during they pass through the material. Thus the ionisation state is changed ever depending on the ratio of the electron loss and electron capturing. For low ion energies the electron capturing prevails, and so it can be assumed that the incident ion is neutralised. For the energy range of 1 keV to 300 keV, which is the case in this thesis, the ions are neutralised as soon as they are in the crystal. For high energies the electron loss prevails and so it can be assumed that the ion is ionised totally. In this case the velocity of ions is larger than the orbital velocity of the K-electrons of these ions. Thus energetic ions lose electrons.

The electronic stopping cross-section is difficult to determine. The model of Lindhardt, Scharff and Schiott (LSS model) gives the rate of the energy loss of incident ions per unit depth [53]

$$\left(\frac{dE}{dx}\right)_e = -K_e \sqrt{E_0} = -n S_e(E). \tag{4.13}$$

Here, k_e is a complicate function of atomic mass and atomic number of the target atoms as well of incident ions. *dE/dx* is the energy lost of the ion per unit path length. The assumption for the equation 4.13 is that the ion and the crystal atom built a quasi molecule for a very short time. There is an exchange of electrons between the ion and target atoms. The electrons of the ion are transferred to the stationary atom and lose momentum. The electrons of stationary atoms are transferred to the ion and their momentum increases. This is the energy loss mechanism of penetrating ions into a crystal [57]. The electronic cross-section can be written in dimensionless units as given in equation 4.14

$$\left(\frac{d\varepsilon}{d\rho}\right)_e = -s_e(\varepsilon) = -k_e \varepsilon^{1/2}. \tag{4.14}$$

Treating the nuclear and the electronic energy loss independent of each other, the total stopping power can be calculated by the sum of the both parts as $S(E) = S_e(E) + S_n(E)$. The total stopping power in practical units is

$$\frac{dE}{dx} = -n[S_n(E) + S_e(E)] \tag{4.15}$$

or in dimensionless units

$$\frac{d\varepsilon}{d\rho} = -[s_n(\varepsilon) + s_e(\varepsilon)]. \tag{4.16}$$

The Monte-Carlo simulation program *SRIM* is based on this model and can simulate the trajectories of the ions, their striking distances, and final transversal distribution [56].

The energy loss depending on the ion implantation energy is shown for the light ions like Mn and Co (transition metals) in figure 4.5.a and for heavy ions Gd, Tb, and Dy (lanthanides) in figure 4.5.b. In both cases GaAs (100) is the target material. The detailed growth data of the target material are listed in appendix C. For the light ions manganese and cobalt the nuclear energy loss is slightly stronger than the electronic loss (figure 4.5.a). The nuclear loss has a maximum at about 50 keV, and after this point the nuclear stopping power decreases slightly with increasing implantation energy, which is the typical course of the nuclear loss effect. The electronic loss shows the typical $E^{1/2}$-dependence on the ion energy. For heavy ions the nuclear energy loss is clearly the dominant effect (figure 4.5.b), but has a saturation character (figure 4.5.b) instead of the typical course with a maximum. This results from the inelastic sputtering of the target atoms by incident heavy ions, while the Monte-Carlo simulation based on the elastic two-body collisions.

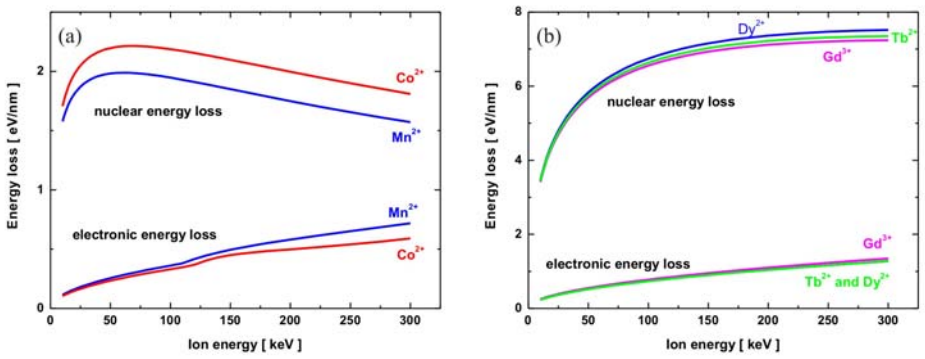

Figure 4.5: *Energy loss depending on the implantation energy is simulated by SRIM: (a) For transition metals Mn and Co, (b) for lanthanides Gd, Tb, and Dy.*

4.1.3 Striking distance and straggling

The incident ion is scattered multiple times from the lattice atoms and travels on a zigzagging path to the final stopping place while it losses all the kinetic energy. So the

final position of an ion has a certain depth, i.e. the distance of the final position, from the target surface, which is called here the striking distance R_l. The actual total distance, which the ion travels, is in general larger than the striking distance. The ion has also a deviation from the normal of the target surface at impinging point, which is called here the straggling R_t. These definitions are represented in figure 4.6 schematically. The specifying parameters for the striking distance are the atomic density N of the crystal, the energy of the projectile-ion, the relative atomic masses and atomic number of projectile and crystal atoms.

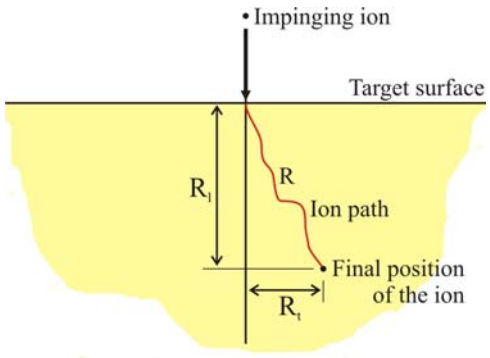

Figure 4.6: *A schematically drawing of an impinging ion onto a solid crystal surface which shows the relationship between the ion path* R*, the projected range* R_l *and the transverse straggling* R_t.

The striking distances and the straggling are simulated with the *SRIM* program for Mn, Co, Gd, Tb, and Dy ions in target crystal GaAs. The results are listed in table 4.2. The notation in this table corresponds the one in figure 4.6. The implantation energies are calculated with equation 4.17

$$E = h\,e\,U \tag{4.17}$$

where, h is the degree of ionisation, e the elementary charge, and U the acceleration voltage of the ions. The values for R_l and R_t are mean values. The striking distance (projected range) R_l and the straggling R_t decrease with increasing relative atomic mass. The stopping powers for the heavy ions (Gd, Tb and Dy) are 10-times larger than for the light ions (Mn and Co) due to the larger cross-sections.

Table 4.1: *The results of the* SRIM *simulation for Mn, Co, Gd, Tb, and Dy are listed. The heavier (bigger) the ion the smaller is the striking distance and the straggling due to the increasing cross-section of the collision.*

Ions	Rel. atomic mass	E_{impl} [keV]	R_l [nm]	R_t [nm]
Mn^{2+}	54.94	200	115.8	62.2
Co^{2+}	58.93	200	109.5	57.4
Gd^{3+}	157.25	300	68.2	24.5
Tb^{2+}	158.93	200	49.1	18.1
Dy^{2+}	162.50	200	48.7	17.8

4.2 Formation of new compounds

The synthesis of new materials using high dose ion implantation is an internal growth process and called "mesotaxy" by analogy with epitaxy [58] or ion beam synthesis (IBS). Using high dose ion implantation (~ 10^{18} ion/cm^2) and annealing buried single crystal layers can be grown with electrical characteristics that are comparable with MBE grown samples [57].

There are two classes of samples in chapter 4 on which the ion implantation executed. The samples in the first class are semi-insulating GaAs (100) substrates (with the labels *#s100* and *#s3661*) implanted with Mn^{2+}, Co^{2+}, and Dy^{2+}. The samples in the second class have the layer sequence $\{GaAs(2nm)/AlAs(2nm)\}_{20}$ /GaAs(300nm) grown in III-V-MBE system on a 50 nm thick GaAs (100) substrate (with the label *#11075*) (for details see appendix C) implanted/deposited with Mn^{2+}. Table 4.2 summarises these sample classes.

The possible reactions depend on the concentration of the participated substances, the temperature, the chemical features of the incident ions and the target atoms. From a pure statistically point of view, only a finite number of products will arise by the implantation of element *X* into GaAs as suggested below in reaction equation 4.18-4.21. More complicated reactions are not excluded.

Table 4.2: *The features of the implanted ions are listed. The electron configuration in the closed shells are for the transition metals (TM) [Ar] = $1s^2\ 2s^2\ 2p^6\ 3s^2\ 3p^6$ and for the rare earths (RE) [Xe] = [Ar] $3d^{10}\ 4s^2\ 4p^6\ 4d^{10}\ 5s^2\ 5p^6$. μ_B is the Bohr magneton. The spectroscopic term symbols of the ground state are determined with Hund's rules.*

Element / ion	Mn / Mn^{2+}	Co / Co^{2+}	Dy / Dy^{2+}
Atomic Number	25	27	66
Type	TM	TM	RE
Electronic Configuration	$3d^5\ 4s^2$ $3d^5\ 4s^0$	$3d^7\ 4s^2$ $3d^7\ 4s^0$	$4f^{10}\ 6s^2$ $4f^{10}\ 6s^0$
$S=\Sigma s_i$	5/2 5/2	3/2 3/2	2 2
2S+1	6 6	4 4	5 5
l	2 2	2 2	3 3
m_l	0, ±1, ±2 0, ±1, ±2	0, ±1, ±2 0, ±1, ±2	0, ±1, ±2, ±3 0, ±1, ±2, ±3
$L= \Sigma m_l$	0 0	3 3	6 6
$J=\lvert L \pm S \rvert$	5/2 5/2	9/2 9/2	8 8
Term symbol of Ground state	$^6S_{5/2}$ $^6S_{5/2}$	$^4F_{9/2}$ $^4F_{9/2}$	$^5I_8$ $^5I_8$
Magnetic moment per atom/ion	$5\mu_B$ $5\mu_B$	$3\mu_B$ $3\mu_B$	$4\mu_B$ $4\mu_B$
Implanted in sample class	#11075	#s100	#s100

$$X + GaAs \rightarrow X + GaAs\,, \tag{4.18}$$

$$X + GaAs \rightarrow Ga + XAs\,, \tag{4.19}$$

$$X + GaAs \rightarrow XGa + As\,, \tag{4.20}$$

$$X + GaAs \rightarrow (Ga, X)As\,. \tag{4.21}$$

It should be found a way to reduce the number of the reactions, which are respected here, in order to consider only the reactions, which are really possible within the framework of the rules of physical chemistry under the present implantation and RTA conditions. In fact, only the stable chemical phases are relevant, where the phase diagrams can be helpful. Thus the chemical phases must be considered which are stable at RT and at the certain content *x* of the implanted ions.

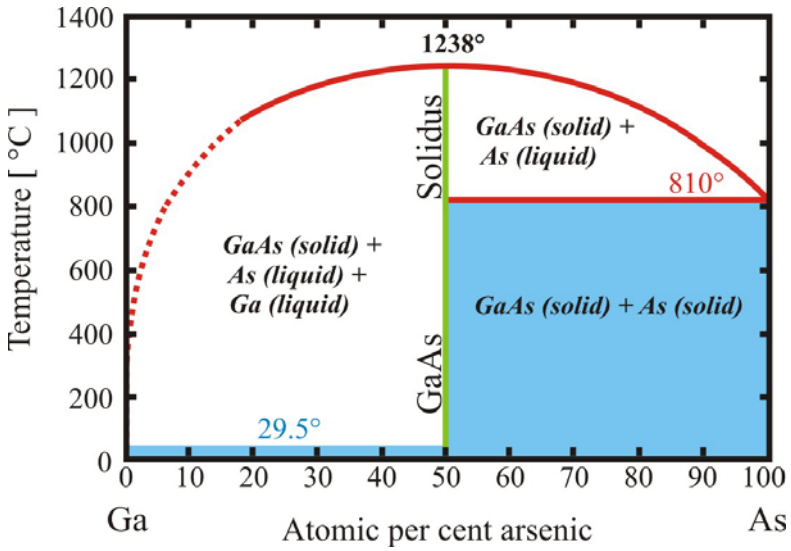

Figure 4.7: *The phase diagram of GaAs. The dashed red line is a theoretical extrapolation [59].*

The phase diagram of the reactant GaAs is represented in figure 4.7, which is the common material for all implantations. The solid (blue, green, and red) lines represent the experimental data and the dashed red line (below 20 atomic per cent arsenic) is a theoretical extrapolation. The blue region marks the solid stable phase for different compositions of gallium and arsenic. The solid crystalline GaAs with zinc-blende

structure is stable in the temperature range of 29.5°C - 1238°C and only for the chemical compositions of 50.065 - 49.985 atomic per cent gallium (green line in figure 4.7) [60]. In the region between the red line and the blue area there is a mixture of solid GaAs, liquid Ga, and liquid As. Above the red curve GaAs becomes gas.

4.2.1 Manganese in GaAs

Manganese is a transition metal with partially filled 3d-orbitals and has a magnetic moment of $5\mu_B$ per atom in twofold ionised state (table 4.2). Due to the unpaired 5 electron spins manganese is a good candidate to make GaAs a magnetic semiconductor. To achieve this aim (Ga,Mn)As has grown by LT-MBE [1] or MOVPE [41]. Figure 4.8.a shows the phase diagram of (Ga,Mn)As depending on the Mn concentration *x* and the growth temperature [1].

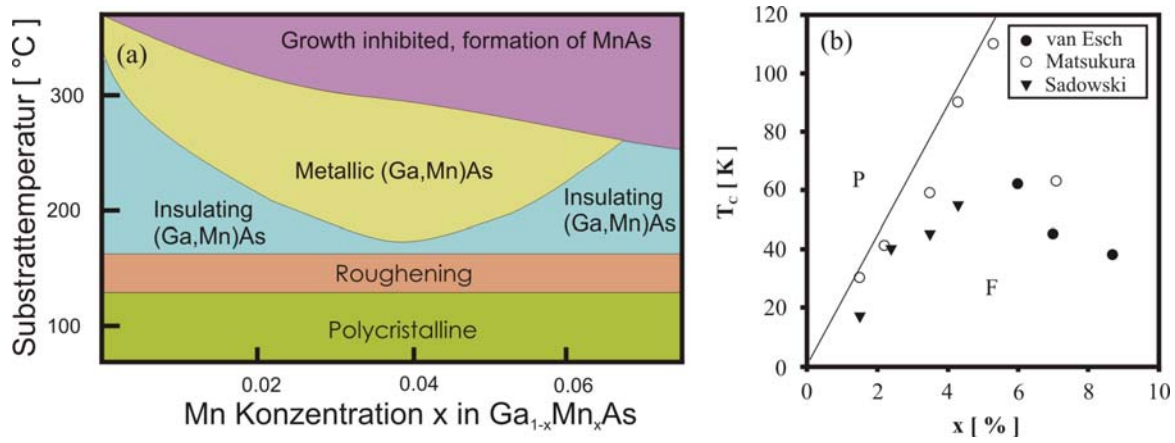

Figure 4.8: *The phase diagram of (Ga,Mn)As: (a) Mn content x vs. the growth temperature [4.8] and (b) the Curie temperature vs. Mn content x are shown [61].*

$Ga_{1-x}Mn_xAs$ mixed crystals with relatively high Mn concentration can be grown only at low temperatures (~250°C) as shown in figure 4.8.a. When the Mn flux or the substrate temperature, or both, were too high (*$x > 0.06$, $T_{sub} > 300$°C, the lilac area in figure 4.8.a*), a complex RHEED pattern appears that indicates the formation of the MnAs second phase on the surface in hexagonal NiAs-structure. This is due to the low solubility of magnetic elements in the compound semiconductors. MnAs occurs either in hexagonal NiAs-type structure with a lattice parameter of *$a = 3.7$ Å* and *$c = 5.7$ Å* or

in zinc-blende structure with $a = 5.98$ Å [1, 29, 62, 63]. By Mn implantation into GaAs and subsequent heat treatment, also GaMn ferromagnetic alloys can occur in several different phases like hexagonal Mg_3Cd-type superlattice (with $a = 5.4$ Å, $c = 4.4$ Å) and tetragonal CuAu-type phase ($a = 3.4$ Å and $c = 3.7$ Å) [64-66].

In general the formation of clusters was prevented because of the interest in epitaxially growth of samples with smooth surface. But it is well known, that a (Ga,Mn)As mixed crystal is not ferromagnetic at room temperature (RT) [23] as shown in figure 4.8.b. The ferromagnetic ordering temperature T_C increases with increasing Mn content up to $x \sim 5$. But additional increase leads to decrease in T_C because of the reduced crystal quality by the strong doping and the self-compensation mechanism.

MnAs and GaMn clusters are ferromagnets with a Curie temperature above 300 K [67]. In order to get a ferromagnetic semiconductor they can embed in a paramagnetic semiconductor matrix and such a material system is called semiconductor-ferromagnetic hybrid structure. Lampalzer at the Philipps-University Marburg reports that MnAs clusters form mostly on the surface and can be overgrown only with AlAs [29]. Mn act as an acceptor in (Ga,Mn)As and provide p-type conduction. (Ga,Mn)As can be grown also as n-type, which is an advantage because of the higher mobility of electrons than holes.

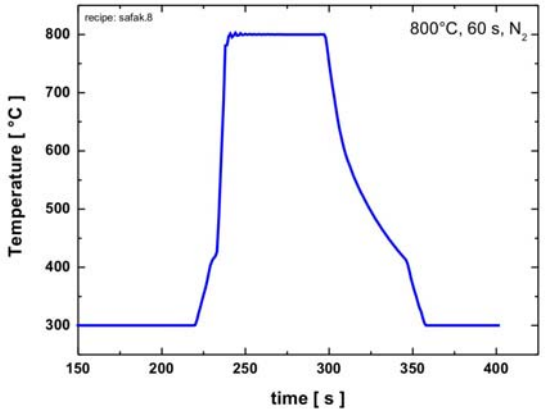

Figure 4.9: *The temperature course of RTA process is shown: annealing at 800°C for 60 s.*

In order to study the behaviour of Mn in GaAs Mn^{2+} ions are implanted into GaAs (samples: #11075, #s3661-6a, s100) at energy of 200 keV and doses ranging from $4.4 \cdot 10^{14}$ to $1.7 \cdot 10^{17}$ Mn^{2+}/cm^2 at RT. The penetration of the ions is simulated by *SRIM* and is about 118 nm. The samples are annealed subsequently at 800°C for 30 s in reduced inert gas atmosphere (90 % N_2, 10 % H_2). This was done to cure the lattice defects caused by the implantation process. In order to avoid the arsenic escape, the samples are covered with an unprocessed GaAs wafer. This is the so-called *face-to-face technique*. The time dependent course of the temperature for a RTA (rapid thermal annealing, see chapter 3.4) process at 800°C for 60 s is shown in figure 4.9 as an example drawn from the pyrometer data.

The surface dose of the deposition is given as $D = (I/f)(1/k^2d^2e)$, where I is the ion current, f the frequency of the beam motion, i.e. $1/f$ is the dwell time of the beam on a certain point. k is the step number, d the step length and e the elementary charge. If a rectangle area is scanned by a beam with an ion current of 15 pA, frequency 2000 kHz and the step size 16 nm (is the minimal step size of the used FIB facility), the calculated dose is then about $9 \cdot 10^{12}$ ion/cm^2. With a repetition number N the ion dose can be increased. The surface atomic density of a GaAs layer with 10 nm thickness is $4.42 \cdot 10^{16}$ ion/cm^2. So theoretically GaAs becomes amorphous by a greater implantation/ deposition dose than the surface atomic density.

Unfortunately, there is no generally accepted nomenclature for nearly spherical particles formed by synthesis and annealing. In this work, these particles will call depending on their size cluster (2 nm), nanoparticle (2-100 nm) or sub-micronparticle (100-1000 nm) as in the reference [30].

Mn^{2+} ions were implanted into the sample #11075-24 at energy of 200 keV with a dose of $2.7 \cdot 10^{16}$ ion/cm^2. The sample was annealed at 830°C for 60 s subsequently. The topology images of the surface are shown in figure 4.10. The AFM image of the unimplanted and unprocessed GaAs shows a smooth surface with an average roughness of 0.11 nm (figure 4.10.a). Implanted ions are distributed (dose is about $4.4 \cdot 10^{16}$ cm^{-2}) statistically in a layer of 118 nm thickness and there are no clusters on the surface just after the implantation as shown in figure 4.10.b. The average roughness is increased due to the atomic dislocations on the surface and is 0.23 nm. The AFM image taken after the thermal treatment shows cluster formation on the

surface (figure 4.10.c and d) and thus an increased average roughness of 7 nm. The nanoparticles have diameters in the range of 50 nm - 150 nm and heights of 25 nm - 60 nm with an average separation of 384 nm. The density is about $1 \cdot 10^9$ cm^{-2}. Some of them are grown together.

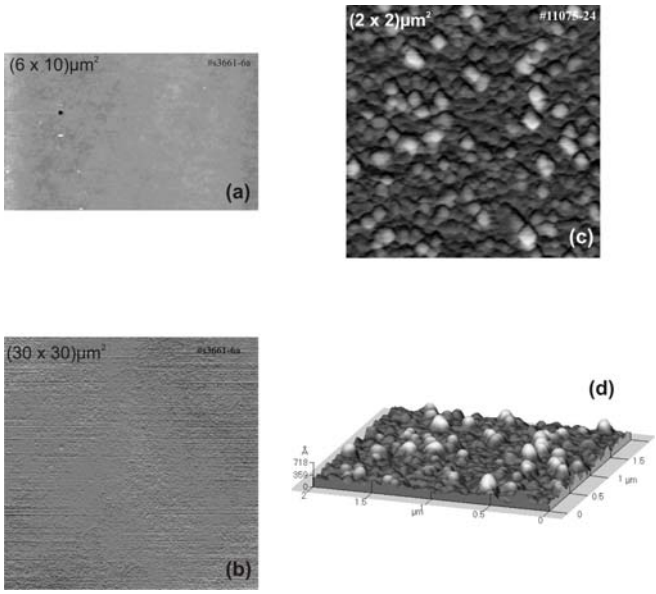

Figure 4.10: *The AFM images show (a) an unprocessed GaAs surface, (b) GaAs surface just after the Mn implantation, (c) Mn implanted GaAs surface after RTA, and (d) the perspective of the same area in (c). All images are taken at RT.*

On the AFM images in figure 4.11 the formation of new compounds is studied. The implantation of Mn into GaAs leads to formation of some "particles" after annealing. The diameter and the number of these particles depend on the annealing parameters (the temperature and duration), implantation dose, and the size of the implanted region. In figure 4.11 the implantation dose is varied at a constant size of the implanted region (2200 nm). At doses in the order of 10^{16} ion/cm^2 and higher, the RTA process leads to formation of sub-micronparticles with diameters ranging from 95-235 nm. In the region with smallest implantation dose (figure 4.11.e) there are some "particles" with sizes of 40-60 nm, but due to the resolution of the AFM facility (in the order of 10nm) it is not possible to say if they are nanoparticles. The implantation dose in figure 4.11.a ($5.7 \cdot 10^{16}$ ion/cm^2) is larger than the surface atomic density of GaAs ($4.4 \cdot 10^{16}$ ion/cm^2). The height difference between the deepest point in this region and

the unimplanted environment is 20 nm. With increasing dose the size of the sub-micronparticles becomes larger and their number smaller, that indicates they grow together. Inversely, with decreasing dose the sub-micronparticles become smaller and the spacing between them larger.

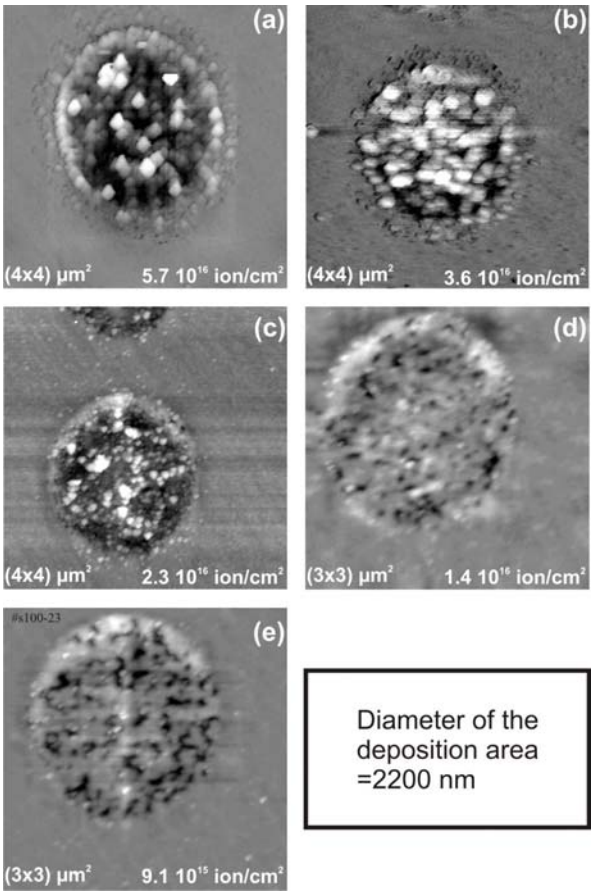

Figure 4.11: *AFM images show implanted circular regions, where the dose varied. The samples are annealed at 800°C for 30 s.*

In figure 4.12 the size of the implanted region is varied at a constant dose of $5.7 \cdot 10^{16}$ ion/cm^2. With decreasing size of the implantation area the density of impinging ions increases, so that the number of the nanoparticles decreases and the diameter of the nanoparticles become larger. Thus, the size and the number of the nanoparticles can be adjusted by the RTA parameters, implantation dose, and the size of the implanted region, so that a single particle can be created as an element of an electronics device.

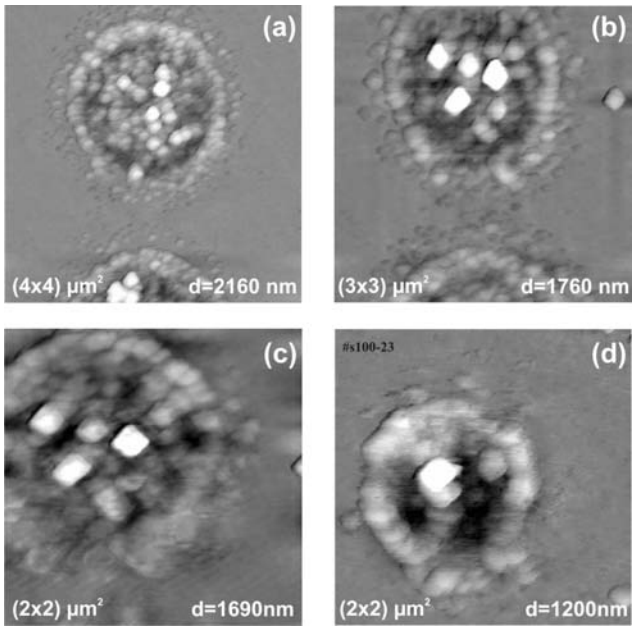

Figure 4.12: *AFM images show the nanoparticle formation depending on the diameter of the implantation area. The implantation dose of $5.7 \cdot 10^{16}$ ion/cm^2 is constant for all samples, which are annealed at 830°C for 30 s.*

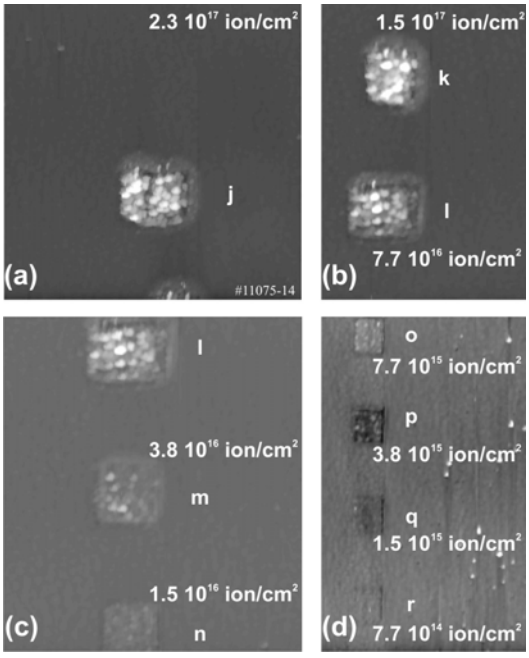

Figure 4.13: *AFM images show the sputter effect of the implantation depending on the implantation dose. The samples are annealed at 830°C for 60 s. The image sizes are (17.5x17.5) µm^2 (a), (25x17.2) µm^2 (b), (25x22.1) µm^2 (c), and (40x24.3)µm^2 (d).*

The sputter effect of the implantation is considered under the influence of dose variation in figure 4.13.a-d. The size of the implanted squares is 4x4 μm^2, inclusively the "halo". For the first three implantation areas j, k, and l (figure 4.13.a and b) the doses are higher than the amorphization limit of GaAs surface. Just after the implantation there is an atomic powder. By annealing these atoms built in again to the crystal, during some of them form the sub-micronparticles. Thus large differences between heights of the implanted area and the unimplanted environment are observed as seen in figure 4.13.a and b. These dislocations become less and less with decreasing dose (implantation areas m-r).

In order to analyse the chemical composition of the implanted regions EDS measurements are performed as shown in figure 4.14 for the region in figure 4.10.c.

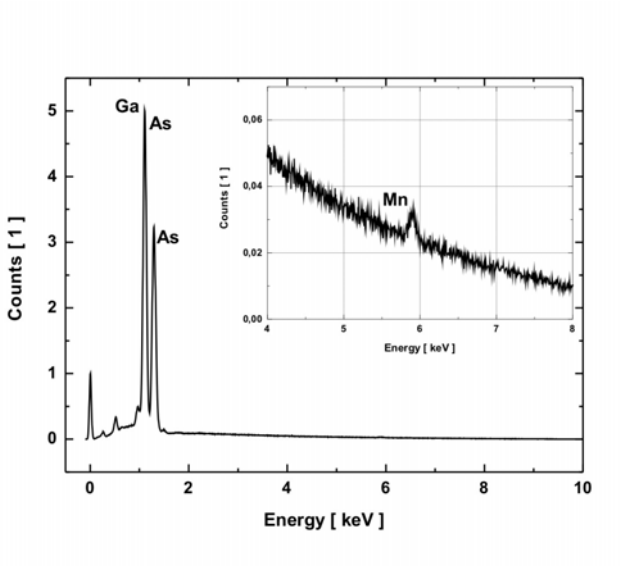

Figure 4.14: *The EDX spectrum on the region in figure 4.10.c. The inset is a zoom-in of the energy interval of 4 - 8 keV of the total spectrum. The small peak comes from the k-lines of manganese at about 5.8 keV.*

The formation of the submicron ferromagnetic alloys GaMn, MnAs and $MnGa_nAs_m$ (*n* and *m* are the contents of the corresponding elements) on the sample surface by ion implantation into GaAs and subsequent thermal treatment is reported in [62-66, 68]. Even these research groups give certain chemical compositions determined by the combination of EDS, TEM, AFM, MFM, alternating gradient magnetometer (AGM),

superconducting quantum interference device magnetometer (SQUID) and/or magnetic circular dichroism (MCD) spectra. The determination of the chemical composition of the nanoparticles demands investigations by different methods confirming in different respects.

According to the EDX spectra and the AFM images it can be suggested that the clusters in figure 4.10, 11, 12, and 13 are $MnGa_nAs_m$ alloys formed at temperatures above 750°C after RTA, which is in a good agreement with [68].

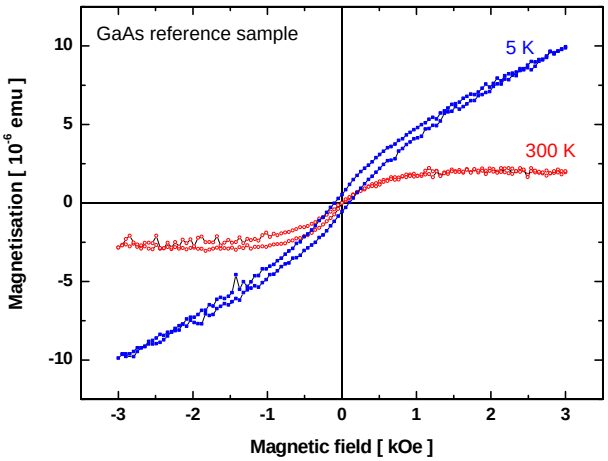

Figure 4.15: *SQUID measurement on the reference sample shows a hysteric curve with very small remanence.*

A SQUID measurement of magnetisation is performed on a GaAs reference sample, which is not implanted. The resulting graphic of magnetisation vs. magnetic field shows a very small remanence at 5 K, which vanishes totally at 300 K, a paramagnetic behaviour as drawn in figure 4.15. Pure GaAs is diamagnetic meaning that the reference sample has some magnetic impurities, which make GaAs paramagnetic.

Figure 4.16 shows the SQUID measurements of Mn implanted GaAs. The implantation was performed at 200 keV with a dose of 5.2 10^{15} ion/cm^2. In order to check the effect of RTA on the magnetic activation of the ions the magnetisation measurements are performed before and after the thermal treatment. The comparison of the reference sample with implanted samples shows changes in remanence

magnetisation, saturation magnetisation, and coercive field meaning that a part of the Mn ions are incorporated into the paramagnetic GaAs lattice. Thus, this material is ferromagnetic (if the clusters are coupled among themselves) or more likely superparamagnetic (if they are not coupled among themselves).

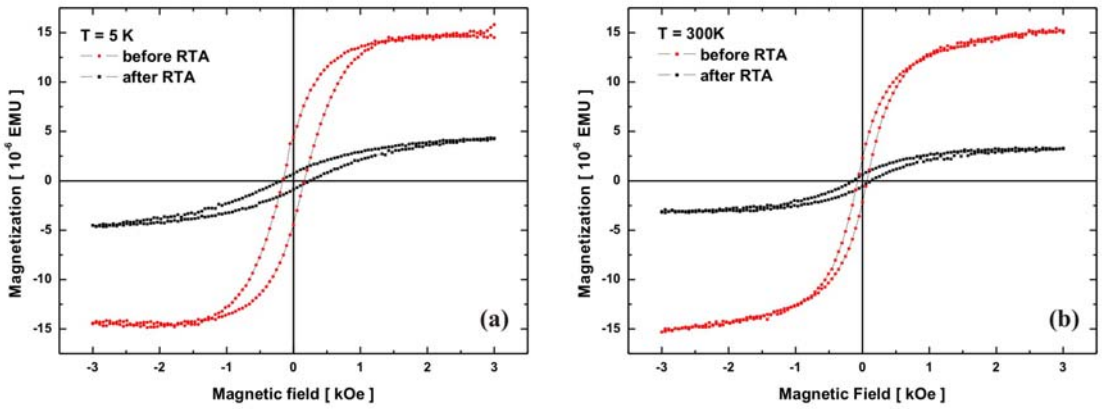

Figure 4.16: *SQUID measurement of magnetisation vs. magnetic field on Mn implanted GaAs with a dose of $5.2 \cdot 10^{15}$ ion/cm^2: (a) At 5 K and (b) at 300 K. RTA is carried out at 800°C for 30 s.*

Remanence values of magnetisation for both temperatures (5 and 300 K) are small indicating a paramagnetic phase. It is remarkable that the room temperature remanence remains 16 % of the low temperature value before RTA and 27 % after RTA. The apparent decrease in remanence magnetisation after RTA process is probably due to the observed As vacancies induced by thermal treatment.

For MBE grown samples the Mn content is determined in general indirect in the literature, i.e. the lattice constant of (Ga,Mn)As is determined by high resolution x-ray diffraction (HRXRD) and the Mn content is calculated by Vegard's law [19, 41, 69]. This conventional method is not suitable for the implanted samples due to the non-epitaxial sample structure. On the other hand the cluster size is not resoluble by HRXRD. The saturation magnetisation M_S (figure 4.16.a) is used, in order to determine the number of the Mn ions, which are incorporated into the crystal substitutional. M_S is $15.0 \cdot 10^{-9}$ Am^2 or $15.0 \cdot 10^{-6}$ emu (latter one is the usual unit of the

magnetisation in the literature) at 5 K. The resolution of the SQUID facility is in the order of 10^{-6} emu (model *MPMS XL* from the company *Quantum Design*). At high magnetic fields all these ions are aligned and contribute to the magnetisation. One Mn ion has a magnetic moment of $5\mu_B$. So, the number of the Mn ions, which contribute to the determined saturation magnetisation is then $3.24 \cdot 10^{14}$. The surface dose of the implantation is $5.20 \cdot 10^{15}$ ion/cm^2. The number of the Mn ions in the implanted area of 11 mm^2 distributed in a layer with a thickness of 118 nm simulated by SRIM is $5.72 \cdot 10^{14}$. Thus the substitutional Mn ions are then approximately 57 % of the totally implanted ions. The residual part is on the interstitial position.

4.2.2 Cobalt in GaAs

The transition metal cobalt has partially filled 3d-orbitals and a magnetic moment of $3\mu_B$ per atom in twofold ionised state as given in table 4.2. The unpaired 3 electron spins makes cobalt another good candidate to make GaAs magnetic. Therefore Co^{2+} ions are implanted into GaAs (#s100), where the penetration of the ions simulated by SRIM is about 88 nm at implantation energy of 200 keV with doses ranging from $1.8 \cdot 10^{14}$ - $2.2 \cdot 10^{17}$ ion/cm^2. Subsequently the samples are annealed at temperatures from 700 - 830°C for durations between 5 and 60 s in reduced inert gas atmosphere.

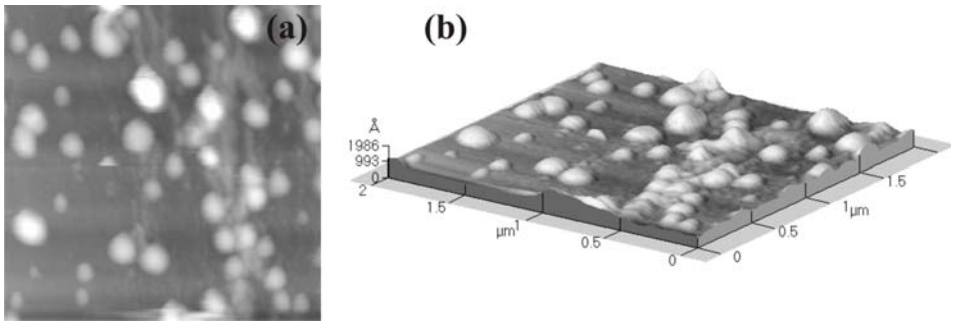

Figure 4.17: *The AFM image of the sample #11075-Co-20 represents in (a) the top view and in (b) the perspective of the same area.*

An AFM scan at RT shows the clusters on the surface with diameters in the range of 90 - 280 nm and heights of 30 - 125 nm as depicted in figure 4.17. The average separation of the nanoparticles is 267 nm and the density approximately $9 \cdot 10^8$ cm^{-2}.

ED-X spectroscopy is carried out for structural and compositional analysis on a single nanoparticle as drawn in figure 4.18. The Co peak appears at 0.625 keV (L_1 line).

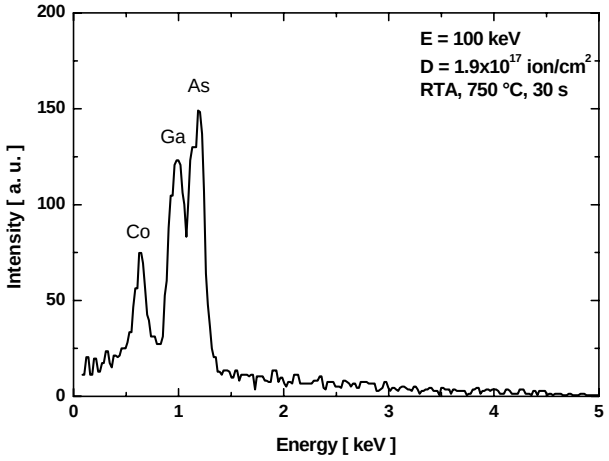

Figure 4.18: *The Co peak recorded on a single nanoparticle can be seen clearly.*

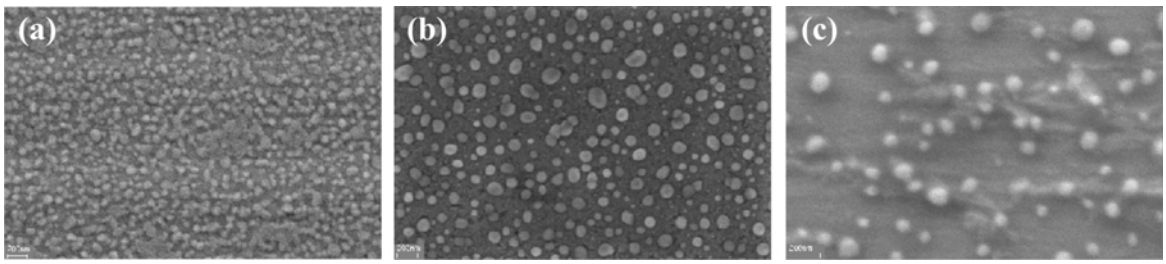

Figure 4.19: *Co^{2+} ions are implanted into un-doped semi-insulating (001) GaAs with energy of 200 keV. The implantation doses are in the order of $1 \cdot 10^{17}$ ion/cm^2. The subsequent annealing is carried out at 700°C (a), 750°C (b), and 830°C (c) in reduced inert gas atmosphere.*

The influence of the temperature of the RTA process on the nanoparticle formation is investigated by SEM (secondary electron microscopy, chapter 3.11) on Co implanted samples annealed at various temperatures. The resulting SEM images are presented in figure 4.19. The size of the images is (2.5 x 1.5) μm^2 (figure 4.19.a, c), and (3.5 x 2.4)

μm^2 (figure 4.19.b). In general, with increasing annealing temperature the density of the nanoparticles becomes smaller and the size larger.

The nanoparticle formation is depends also on the implantation dose as represented in figure 4.20. The implantation is performed with 100 keV ion energy and then the samples are annealed at 750°C. Below a dose in the order of 10^{16} ion/cm^2 there are no formation of nanoparticles observed.

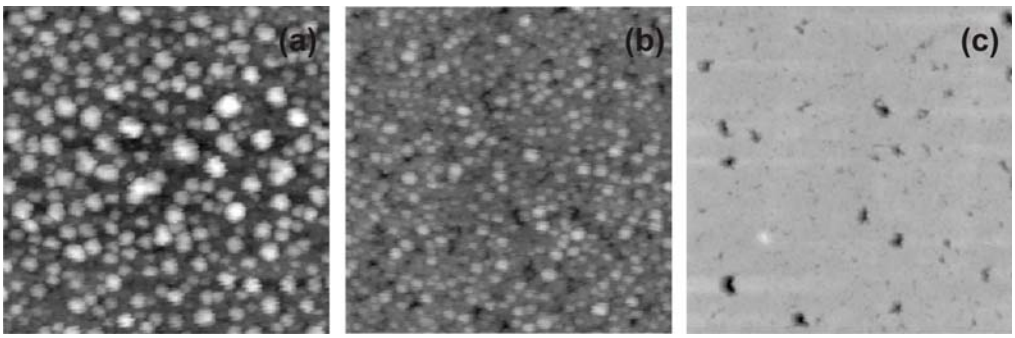

Figure 4.20: *The AFM images show the dose dependence of the nanoparticle formation. The used doses are $1.9 \cdot 10^{17}$ ion/cm^2 in (a), $7.6 \cdot 10^{16}$ ion/cm^2 in (b), and $1.9 \cdot 10^{16}$ ion/cm^2 in (c).*

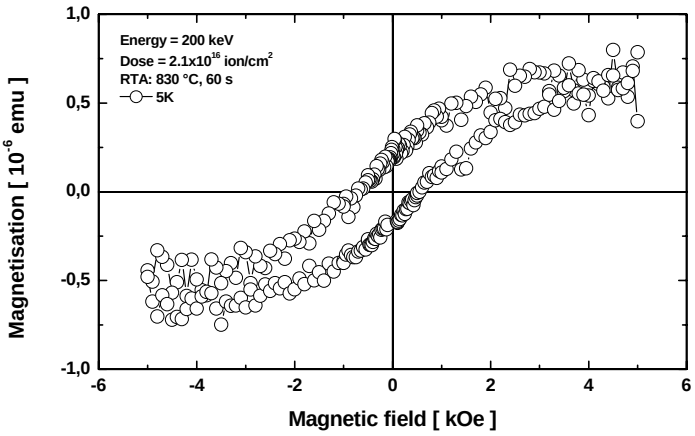

Figure 4.21: *The SQUID measurement of magnetisation shows an open hysteric curve indicating a ferromagnetic material.*

The SQUID measurement performed at 5 K is depicted in figure 4.21. The hysteric curve is open and saturated at a relatively small field of 4 kOe meaning that the material is ferromagnetic or superparamagnetic.

4.2.3 Dysprosium in GaAs

The rare earth dysprosium has partially filled 4f-orbitals and a magnetic moment of $4\mu_B$ per atom (table 4.2). In order to integrate the magnetic properties of Dy to GaAs, Dy^{2+} ions are implanted into an un-doped semi-insulating (001) GaAs sample at ion energy of 200 keV. The simulated penetration of Dy^{2+} ions is about 49 nm. The implantation doses are ranging from $1.8 \cdot 10^{14}$ - $1.2 \cdot 10^{17}$ ion/cm^2. The annealing is carried out at 750°C for 30 s in reduced inert gas atmosphere. The AFM image taken at RT shows clusters on the surface, which have diameters in the range of 40 - 170 nm and heights of 7 - 50 nm as depicted in figure 4.22. The average separation is 160 nm and their density approximately $1.5 \cdot 10^9$ cm^{-2}.

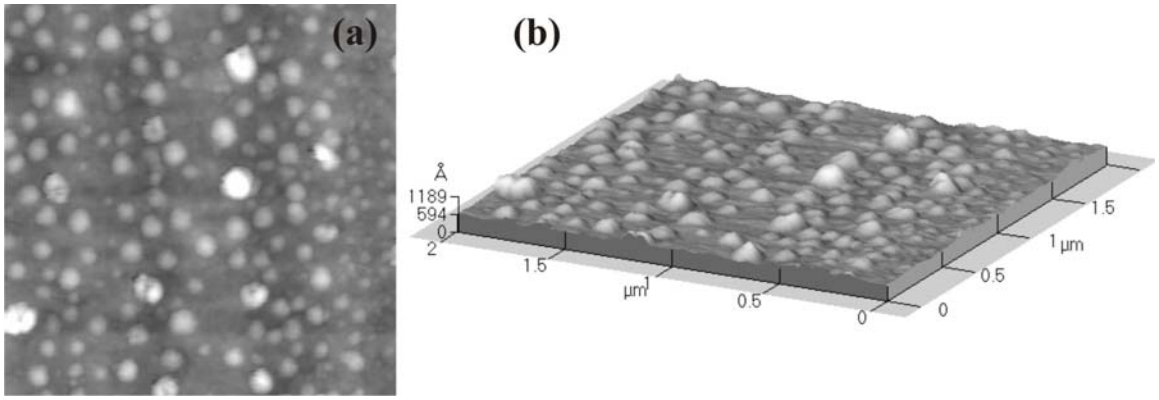

Figure 4.22: *The AFM image of the sample #11075-Dy-20 represents in (a) the top view and in (b) the perspective of the same area.*

For structural and compositional analysis EDX-spectroscopy is performed on a single nanoparticle as drawn in figure 4.23. The Dy peak appears at 1.293 keV and this is the $M_{\alpha 2}$ line.

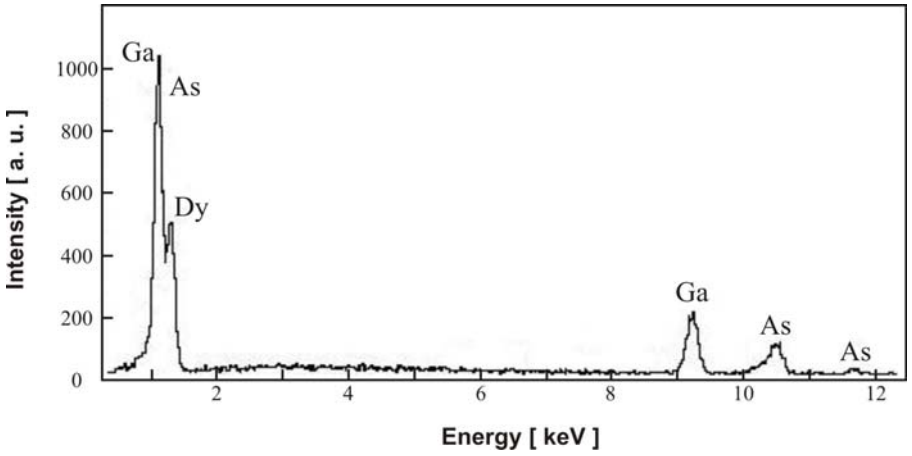

Figure 4.23: *The EDX spectrum on a single nanoparticle shows the Dy peak clearly.*

The nanoparticle formation depends on the size of the implantation area and the dose additionally to the RTA parameters as shown in figure 4.24.

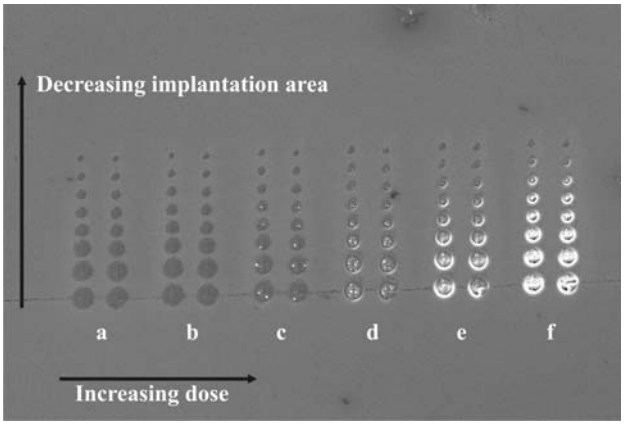

Figure 4.24: *SEM image shows the influence of the implantation dose and the implantation area on the nanoparticle formation on a* Dy^{2+} *implanted sample.*

Chapter 5

Magnetic ions in GaAs

The request of the material with simultaneously semiconducting and ferromagnetic features for the spintronic technology is mentioned in chapter 1 and 2. The temperature dependence of the resistivity showed that the samples grown by LT-MBE with intermediate Mn content (x from 0.035 to 0.053) were on the metal side of the metal-insulator transition [1]. The growth by LT-MBE is a thermodynamically different process than the MBE-FIB preparation. The growth of GaAs at standard substrate temperatures of about 650°C avoids the arsenic anti-sites, which is a disadvantage of LT-MBE leading to a lower carrier concentration and so a lower Curie temperature. MBE-FIB processing in soft-landing mode offers incorporation of magnetic ions with lesser number of crystal defects. The structural aspects of (Ga,Mn)As prepared by ion implantation are discussed in chapter 4. For electric/magnetic characterisation of (Ga,Mn)As new samples are prepared by MBE-FIB technique (#12196 and #12198; at *Institute of applied Solid State Physics at Ruhr University in Bochum*) and compared with samples grown by LT-MBE (*#M275-1* and *#M275-2; at III-V-Heteroepitaxy institute in Würzburg*). In the following paragraphs, the layer structures of the samples, the executed experiments, and our observations are represented.

5.1 LT-MBE samples

The investigated (Ga,Mn)As samples are grown by using an As_4 source. To provide a constant Ga flux, the temperature of the gallium cell was kept fixed at a temperature of 780°C. The LT-MBE processes can be characterised by three independent parameters. (1) The temperature of the Mn cell T_{Mn} is the main factor determining the manganese

incorporation. (2) The substrate temperature T_{sub} is controlled by a thermocouple. (3) The beam equivalent pressure (BEP) ratio of arsenic to gallium (As/Ga) defines the extent of arsenic in the epilayers. First GaAs layer is grown on a (001) GaAs substrate at about 620°C [5.1]. The substrate temperature was then reduced to 270°C and Mn ions were supplied to the growth environment. A (Ga,Mn)As layer was grown with a thickness of 50nm, which is determined by RHEED. The layer structure is shown in figure 5.1.a. The Mn content is about 6-8 %, which is derived from the lattice constant. This sample was annealed in situ at 285°C for 15 min. According to the SQUID measurements the Curie temperature is about 76.8 K. *III-V-Heteroepitaxy group* in Würzburg performs these preparation processes and SQUID measurements.

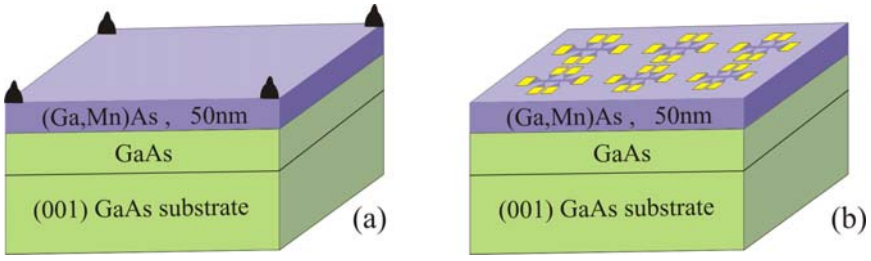

Figure 5.1: *The layer structure of the LT-MBE sample are drawn schematically; (a) for the unstructured sample #M275-1 with InZn contacts at the corners and (b) for the sample #M275-2 with hall bars and gold contacts.*

The Author did the further processes and measurements explained below at *Institute of applied Solid State Physics in Bochum*. InZn contacts were realised on the corners of the unstructured sample #M275-1 (figure 5.1.a) and alloyed at 350°C for 5 min in reducing inert gas (N_2H_2; 10% H_2 and 90% N_2) atmosphere. Sample #M275-2 with Hall bars shown in figure 5.1.b has a mesa height of 110 nm. For the dimensions of the Hall bars see appendix A. Au/Zn/Au p-contacts (chapter 3, table 3.2) are evaporated and then alloyed at 385°C for 2 min in N_2H_2 atmosphere. The contacts are ohmic and have a resistance in the order of 100 kΩ maintained from I(V) curves for sample (*#M275-1*) and determined by TLM technique (chapter 3) for sample (*#M275-2*). The resistance ($\Delta V/\Delta I$) of sample *#M275-2* maintained from the slope of the *I(V)* curve is 133 kΩ.

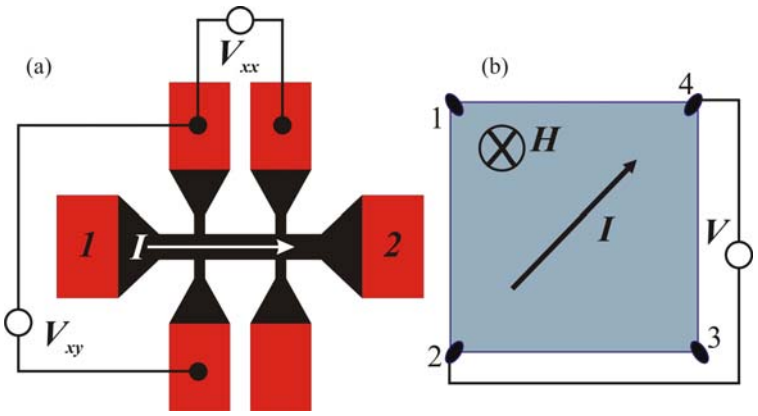

Figure 5.2: *(a) Electric characterisation is performed by Hall bar geometry. The voltages V_{xx} (longitudinal) and V_{xy} (transversal) are taped as drawn in the figure, during the current flows between the contacts 1 and 2. (b) The magnetotransport measurements are performed in two-point geometry with a magnetic field* ***H*** *perpendicular to the sample plane.*

Hall measurements are performed using standard low frequency ac technique in magnetic fields between ±106 mT at RT (figure 5.2.a) in order to determine the electric properties. Table 5.1 summarises the results.

Table 5.1: *The results of the Hall measurements performed at RT at the LT-MBE sample are summarised. The applied magnetic field is 106 mT and the current flow through the Hall bar is 25 μA.*

Sheet resistivity	12 kΩ
Hall voltage	12 μV
Hall mobility	5 cm^2/Vs
2D Carrier concentration	$1.1 \cdot 10^{14}$ cm^{-2}
2D mean free path [μm]	0.8 nm

The positive sign of the Hall voltage indicates a p-type material, so Mn replaces Ga and acts as acceptor. The 3dimensional resistivity of the sample calculated by the formula $\rho_{3D} = R_{sheet}Ld/W$, where L is the length of the Hall bar, W the width and d the thickness of the conducting sheet, is 0.243 Ωcm. The 3dimensional carrier concentration is the 2dimensional one divided by the thickness of the conductive sheet and that yields $2.1 \cdot 10^{19}$ cm^{-3}. Because the length of the Hall bar (400 µm) is larger than the mean free path, the electronic transport happens in the diffusive regime where the Ohmic law is valid.

Magnetotransport measurements are performed using standard dc technique between 4.2 - 100 K, in magnetic fields between ±5 T (figure 5.2.b) by measuring the resistance R as a function of the external magnetic field $\boldsymbol{H}$. The magnetoresistance (MR) effect is defined as the ratio of the resistivity differences in an external field $\boldsymbol{H}$ and in zero-field $R_{rel} = (\rho(H) - \rho_0)/\rho_0$ as discussed in chapter 2. Magnetic fields up to 5 T are applied perpendicular to the sample plane, because the MR effect is largest in this geometry, and smallest when the field is in the sample plane and parallel to the current [29]. The current I is measured at a constant voltage of 5 V and the resistance R is maintained. Figure 5.3 depicts exemplarily for chosen temperatures the temperature-dependency of the MR effect.

At low temperatures ($T < T_C$), a strong negative MR effect is observed with saturation behaviour at high fields. A MR of –97 % is achieved at H = 5 T (figure 5.3.a). While all the magnetic moments are aligned in ferromagnetic configuration, in the crystal ballistic channels open for carriers with spins parallel to the ferromagnetic order of the material leading to a reduction of the spin scattering. With increasing $\boldsymbol{H}$ the number of the aligned localised spins of the magnetic ions and the spins of the free carriers increases. The scattering at the phonons is reduced at low temperatures leading to further decrease in the resistance. With increasing temperature (i.e. increasing number of the phonons) the negative MR effect is suppressed. Between 21 K and 73 K the resistance has a plateau at very low fields following by a decrease at higher fields. The negative MR of about –13 % is achieved at 5 T (figure 5.3.b).

Michel et al. try theoretically to explain the plateau behaviour at very low fields with two models, the network model and the mobility model, based on the splitting of the

two hole-bands (see figure 2.2) in the applied magnetic field leading to changes in the occupation of these subbands and the electronic transport properties [70].

A positive MR is observed above the Curie temperature of 77 K ($T > T_C$) at lower fields, which changes to a negative MR effect after a maximum. This maximum in the resistance shifts to higher fields with increasing temperature. Above T_C the sample is paramagnetic. First, the external field alignes the spins. Due to this spin-rotation a small positive MR effect is observed (figure 5.3.c and d) at lower fields. As all the spins are alinged, a negative MR appears. With increasing temperature, the thermal fluctuations scattering the spins become stronger, and so a stronger field is necessary to align the spins leading to a shift of the maximum to higher fields.

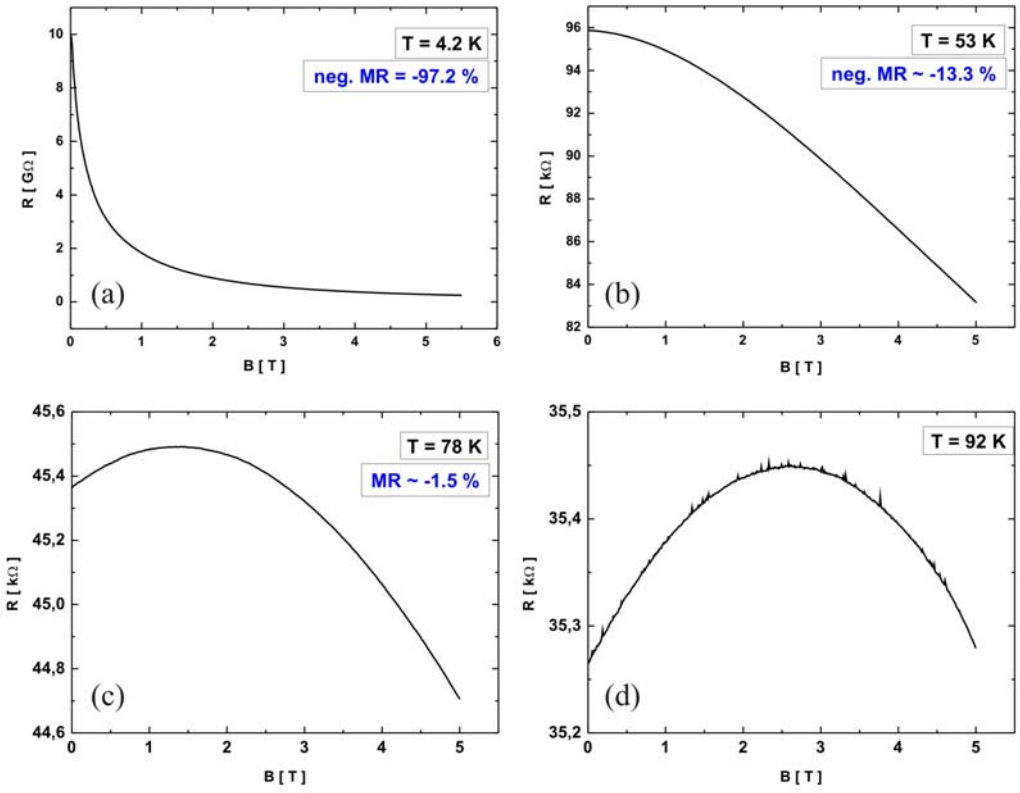

Figure 5.3: *The longitudinal resistance is drawn as a function of the magnetic field at various temperatures. MR effect can be seen clearly at all temperatures.*

Figure 5.4 shows the conductance σ at zero-field calculated from the resistance at zero field (figure 5.3) versus the temperature. The conductance decreases abrupt at the

temperatures around 76 K and 42 K. By temperature variation from higher to lower values, which means starting in paramagnetic phase, the magnetic moments reorient spontaneous at the Curie temperature, and the material change to the ferromagnetic phase. During the reorientation process the conducting electrons experience a stronger spin scattering and this results in a decrease of the conductance. The determined temperature is in a very good agreement with the SQUID measurement. The decrease at 42 K is not understood till now.

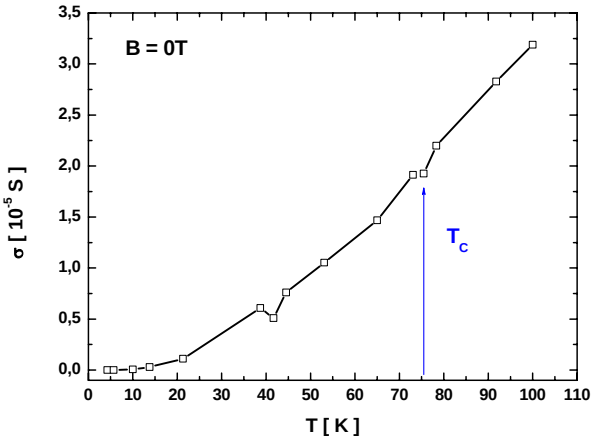

Figure 5.4: *The Conductance is drawn as a function of temperature.*

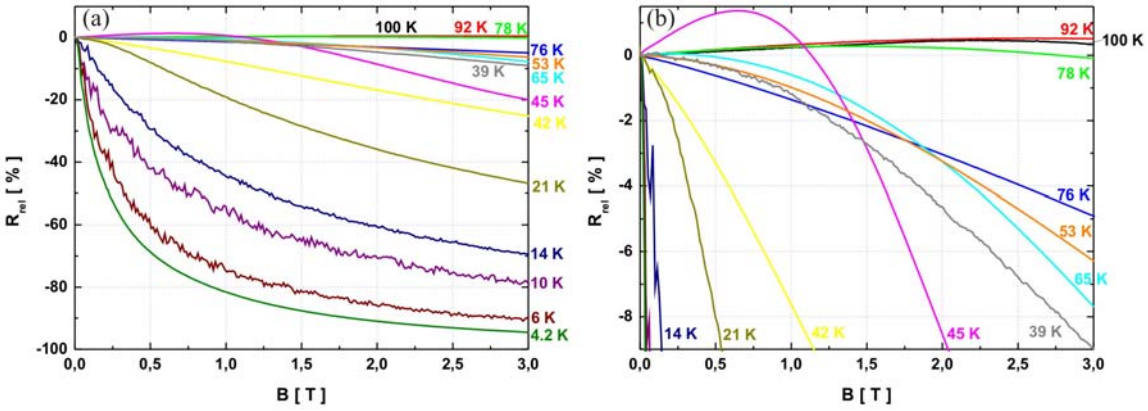

Figure 5.5: *(a) The relative MR is drawn as a function of external field H at various temperatures. (b) The high temperature interval of (a) is zoomed in.*

The relative MR defined by equation 2.18 is depicted in figure 5.5 at various temperatures.

The Hall effect, by which the electrical characterisation is performed (table 5.1), is complicate for magnetic materials, as two effects the ordinary Hall effect and the anomalous (in the literature called usually extraordinary) Hall effect (AHE) contribute to the Hall response. The ordinary Hall effect is proportional to the magnetic field, while the AHE is proportional additionally to the magnetisation of the sample. Therefore AHE offers an experimental technique for determining magnetic properties of DMS materials below the magnetic ordering temperature. The Hall voltage V_H related to the Hall resistance R_H by equation $V_H = IR_H$, where I is the current. The Hall resistivity ρ_H is given then by

$$\rho_H = R_H\, d = R_0\, B + R_S\, M \tag{5.1}$$

where d is the sample thickness, R_0 the ordinary Hall coefficient, B the magnetic field, R_S the anomalous Hall coefficient and M the magnetisation of the sample. For low fields the contribution of the AHE is larger than the ordinary Hall effect (R_S larger than R_0), where the anomalous Hall coefficient is temperature dependent and relates to the longitudinal resistance linearly. The skew scattering mechanism is responsible for this temperature dependent behaviour. If the relationship between the anomalous Hall coefficient and the resistance is quadratic, the side-jump mechanism is the dominant scattering mechanism. During the skew scattering the incident particle changes the flight direction and during the side-jump scattering the incident particle travels onward in the same direction but shifted transversally in the order of 1 Å. For details and mode of action of these scattering mechanisms is referred to [71]. The contribution of the ordinary Hall effect becomes larger with increasing magnetic field, whereat the Lorentz force is responsible. In the saturation, where all magnetic moments are aligned, the ordinary Hall coefficient R_0 is the slope of the $R_H(B)$ function and the dominant term of the Hall response. The ordinary Hall coefficient is temperature

independent, so that the carrier density p can be calculated by $R_0 = (pe)^{-1}$, where e is the elementary charge. These terms are described again in figure 5.6.

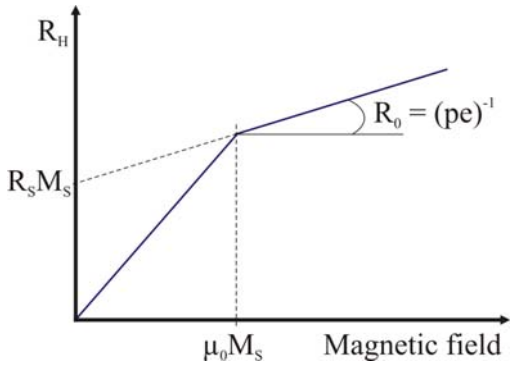

Figure 5.6: *The characteristic $R_H(B)$ curve of magnetic materials with two different slopes below the saturation field $B = \mu_0 M_S$ and above it.*

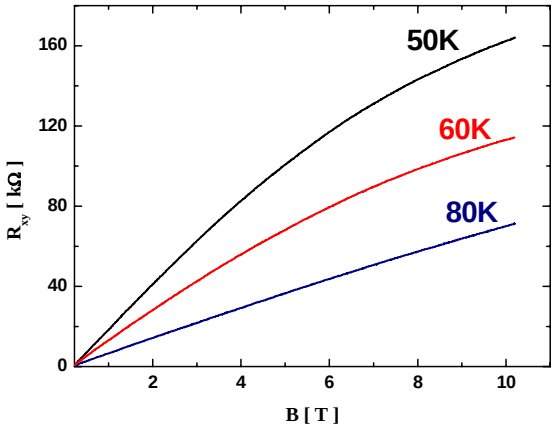

Figure 5.7: *LT-MBE grown sample shows AHE becoming weaker with increasing temperature.*

Figure 5.7 shows the AHE observed on the LT-MBE sample (#M275). With increasing temperature the effect becomes weaker, i.e. the difference between the coefficients R_0 and R_S becomes smaller. Above the order temperature the $R_H(B)$ curve changes into a linear curve, which is characteristic for a paramagnetic material. So the

AHE is a clear indicator for the ferromagnetism. To obtain hole densities from Hall data the measurements are carried out at low temperatures and high magnetic fields. The hole densities calculated from the slope of the $R_H(B)$ curve at higher fields (figure 5.7) are $1.5 \cdot 10^{18}$ cm^{-3} at 50 K and $2.0 \cdot 10^{20}$ cm^{-3} at 60 K.

5.2 MBE-FIB samples

In LT-MBE technique, the As_4 molecules are split only on the substrate surface into As_2 molecules, which have a lower mobility due to the low growth temperatures leading to point defects like arsenic-antisites (As_{Ga}). The samples *#12196* and *#12198* are prepared in the combined MBE-FIB-System at a substrate temperature of 670°C, where an As_2 source is used. The growth temperature and the As_2 source are the two important differences between the MBE-FIB and the LT-MBE systems.

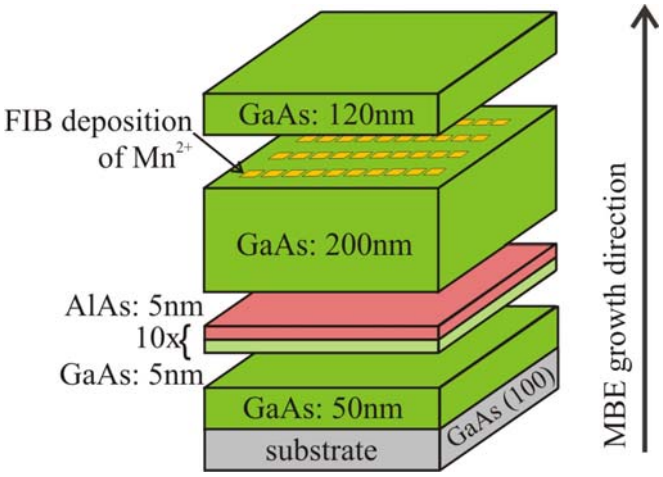

Figure 5.8: *The layer structure of the samples #12196 and #12198 are shown.*

First the oxides are removed from the surface of the semi-insulating GaAs (100) substrate by heating (~ 590°C) in the main chamber of the III-V-MBE-System under UHV conditions ($P < 10^{-7}$ mbar). Then a 50 nm thick GaAs layer is grown. This GaAs layer reduced the roughness of the surface, which increases due to the heating and provides for the following layer structure a „fresh“ and smooth ground. To smooth the surface further the superlattice of alternating GaAs (5 nm) / AlAs (5 nm) layers with ten iterations is grown following by a 200 nm thick GaAs layer. The sample is

transferred then into the FIB chamber by keeping the UHV conditions, so that the still unsaturated atomic/molecular bonds on the sample surface have no possibility to adsorb atoms/molecules from the environment. The combined MBE-FIB System provides exactly the possibility to keep the new grown layer clean during the growth interruption for the deposition of magnetic ions. The layer sequence of the samples *#12196* and *#12198* is drawn schematically in figure 5.8.

The Mn ions are accelerated by thermal field emission from the LMIS to the sample and shortly before the impact slowed down by a converse voltage to energies of several 100 eV (for details see chapter 3.3). The deposition areas are squares with an edge length of 150 µm, which are scanned in a matrix by the ion beam. The ion deposition is performed for the sample *#12196* at 190°C and for the sample *#12198* at 180°C. This is executed as an in-situ annealing process to reduce the crystal defects by the deposition. Afterwards, the sample is transferred back to the main chamber of the MBE in order to grow a protection layer of GaAs with the thickness of 120 nm against the Mn oxidation.

Table 5.3: *The summary of the electrical properties of the annealed and un-annealed samples. The dose is for both* $D = 1.6 \cdot 10^{14}\ cm^{-2}$.

Sample	#12196 (no RTA)	#12198 (RTA)
Sheet resistivity [Ohms]	10065.1 ± 43.6	9114.5 ± 6.9
Hall voltage [µV]	1320.0 ± 0.5	218.5 ± 1.1
Hall mobility [cm^2/Vs]	237	122
2D Carr. Concent. [cm^{-2}]	$2.6 \cdot 10^{12}$	$5.6 \cdot 10^{12}$
2D mean free path [nm]	6.3	4.8

The samples of the *#12198-series* are annealed at 700°C for 5 s, while *#12196-series* are not annealed. The further processing by photolithography is explained in chapter 3.5. For the experiments, van der Pauw structures are etched wet chemically and

macroscopic p-contacts are alloyed for ohmic behaviour at 392°C for 2 min. The processing parameters are summarized in table 3 in appendix C.

The electrical characterisation is performed using standard low frequency dc technique as for the LT-MBE sample and the results are summarised in table 5.3. The mobility decreases with increasing dose (the red curve in figure 5.9) and is hundred times larger than the mobility of the LT-MBE sample. This decrease in the mobility can be explained with the increasing number of the irregularities in the crystal structure induced during the incorporation of Mn. The carrier density increases with increasing dose (the blue curve in figure 5.9) indicating that a part of the deposited Mn ions replaces Ga, but it is relatively less in comparison with LT-MBE sample. An increase in dose results in a decrease in sheet resistivity meaning that the sample shifts to the metallic side. Under the assumptions that the samples are bulk material and the carrier transport happens in the diffusive regime, the resistance of a metal is principally lower than a semiconductor.

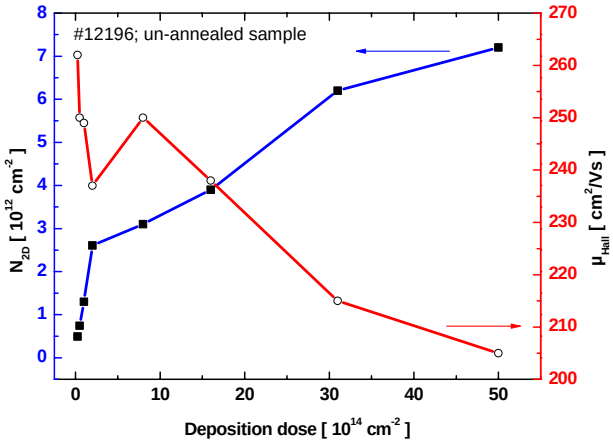

Figure 5.9: *The 2-dimensional carrier density and the Hall mobility are drawn as a function of the surface dose of the deposition.*

In order to determine the transition temperature, the temperature is measured during the sample cooled down in liquid He monotonously where the voltage V is measured at a constant current I in the range of 25 nA. From these voltage and current the

longitudinal resistance R_{XX} is calculated and drawn against the temperature in figure 5.10.a and b. Figure 5.10.c and d show the derivative of the function $log(R_{XX})$ with respect to the temperature T, which reflects clearly the slight increase in the resistance due to the reorientation in the vicinity of the transition temperature T_C. The asymptotic increase of the resistance R_{XX} at low temperatures is typical for semiconductors, which become insulator at T = 0 K.

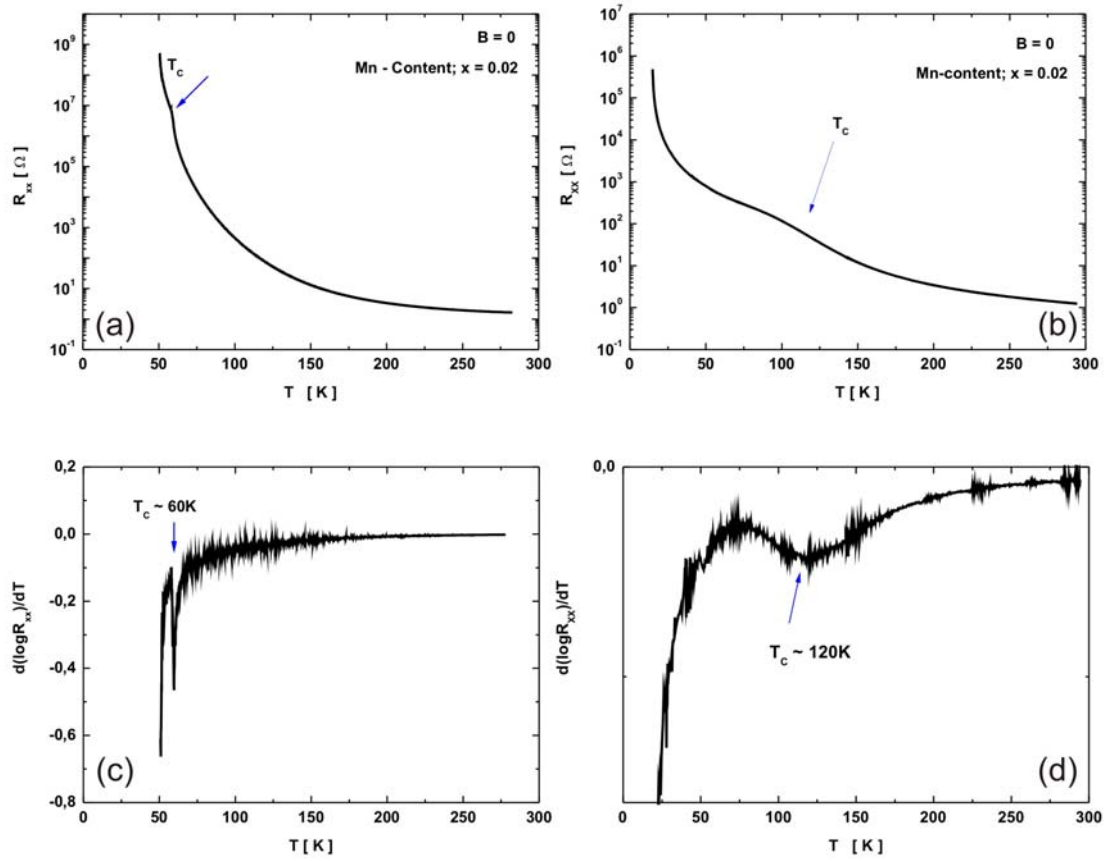

Figure 5.10: *Temperature dependency of the resistance is shown for un-annealed (#12196) and for annealed samples, (a) and (b) respectively. Derivatives of the $log(R_{XX})$ function with respect to temperature shows clearly the transition temperature (c) for un-annealed (T_C = 60 K) and (d) for annealed samples (T_C = 120 K).*

As the transition temperatures for various Mn concentrations are determined and drawn as a function of Mn concentration, the behaviour in figure 5.11 is observed. Thermal treatment activates further Mn ions as acceptors and thus enhances the

concentration of the magnetic moments and holes leading to a higher transition temperature. So the highest transition temperature (63 K) of un-annealed sample (figure 5.11.a) rise to 125 K after annealing (figure 5.11.b).

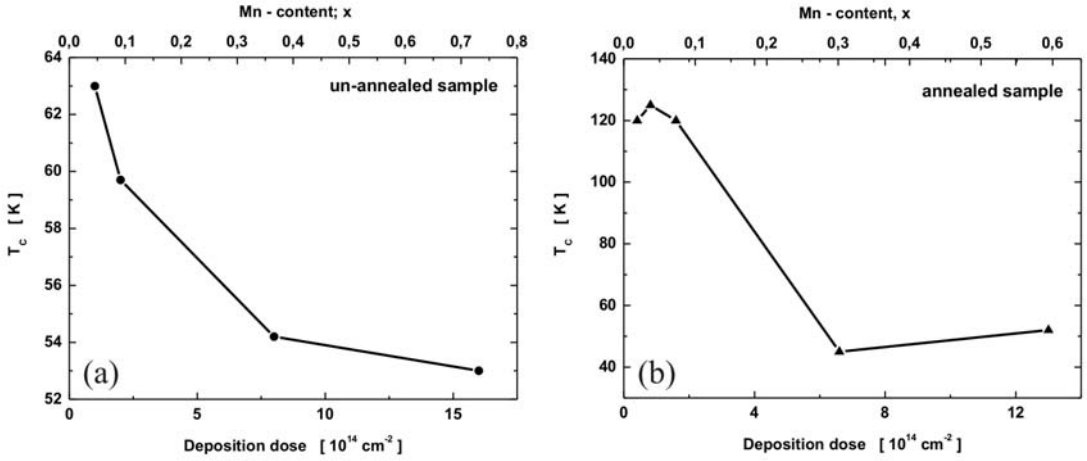

Figure 5.11: *(a) shows the dose dependency of the transition temperature T_C for the un-annealed sample and (b) depicts it for the annealed one.*

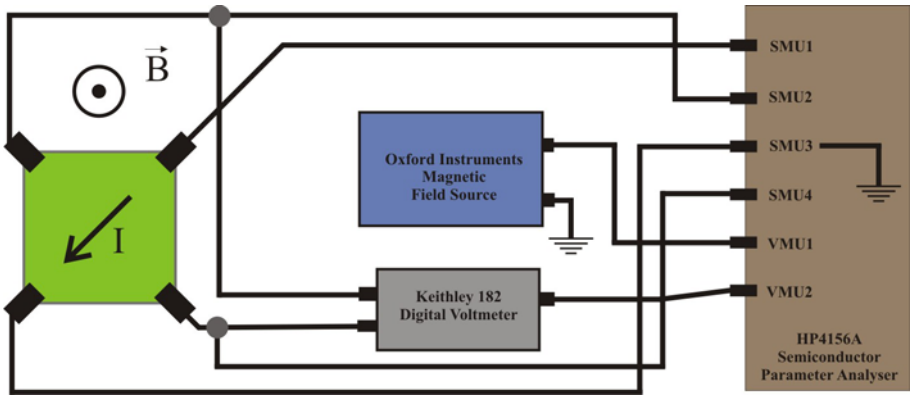

Figure 5.12: *This image shows the experimental setup for magnetotransport measurements in van der Pauw geometry.*

The magnetotransport measurements are performed using standard dc technique between 4.2 K and 100 K. The experimental setup is drawn schematically in figure 5.12. For experiments on un-annealed sample (#12196) magnetic fields up to 10 T are

applied perpendicular to the sample plane, where in the case of in-plane magnetic fields qualitatively the same MR behaviour is observed.

At low temperatures up to 40 K the sample has a very high resistance (~ GΩ), so that the resolution of the experimental equipment is not enough for the measurement of the current. Figure 5.13 depicts the longitudinal relative MR R_{XX} depending on the Mn content x at 40 K. At very low doses (x = 0.003) a strong negative MR effect is observed with saturation behaviour. With increasing Mn content the negative MR effect becomes weaker and above x = 0.091 positive MR occurs (figure 5.13.a) meaning that the sample is in paramagnetic state. The stronger negative MR effect at lower temperatures (40 K) becomes smaller with increasing temperature, which is represented for a Mn content of x = 0.003 in figure 5.13.b. At lower temperatures a plateau is observed for lower fields, which can be explain by the network model or the mobility model mentioned in chapter 5.1.

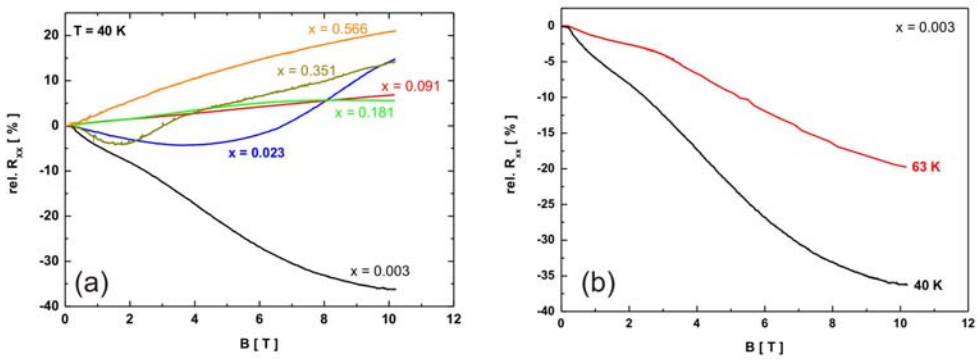

Figure 5.13: *(a) The relative MR at 40 K is depicted as a function of the Mn content. (b) The negative MR effect decreases with increasing temperature. The deposition dose is* $2.5 \cdot 10^{13}$ cm^{-2} *which corresponds a Mn content of x = 0.003.*

The Hall voltage V_H is measured in van der Pauw geometry and the calculated Hall resistance is drawn vs. magnetic field in figure 5.14, where the temperature (figure 5.14.a) and the Mn contend x (figure 5.14.b) are parameters. At temperatures below the ferromagnetic ordering temperature T_C there are two regimes with different slopes (R_0 and R_S). For weaker magnetic fields the AHE dominates ($R_S > R_0$) and for stronger fields the ordinary Hall effect ($R_S < R_0$). For temperatures higher than T_C the ordinary

Hall term is the dominant term and the relationship between the Hall resistance and magnetic field is linear. With increasing Mn concentration the AHE becomes weaker meaning that the sample shifts to the metallic side of the metal/insulator transition. For low concentration of Mn up to x = 0.091 the AHE is clearly observed, so that the sample is a semiconducting and ferromagnetic or superparamagnetic material.

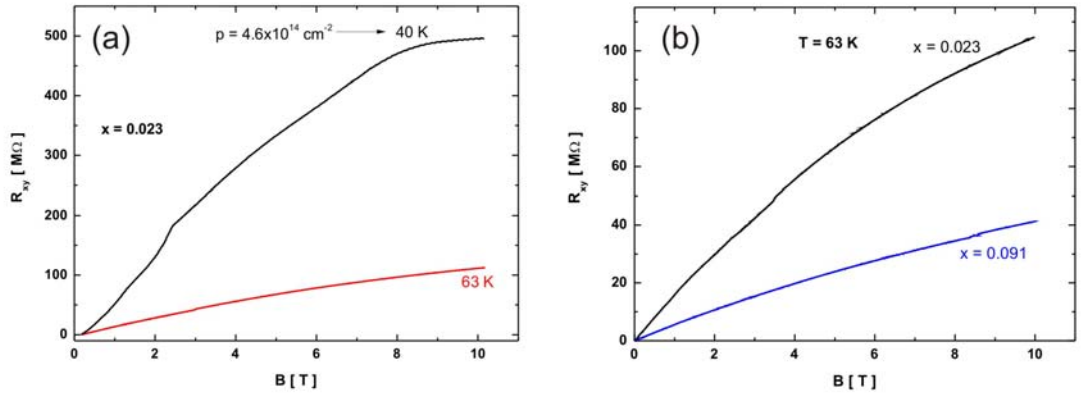

Figure 5.14: *The Hall resistance is drawn as a function of magnetic field depending on the temperature (a). The magnetic field dependence of the Hall voltage is depicted, where the Mn content is the parameter (b).*

The carrier densities depending on the temperature are calculated by the slope at very low and high fields in magnetic field dependent R_{xy} graphics as $4.6 \cdot 10^{14}$ cm^{-3} at 40 K and $4.2 \cdot 10^{15}$ cm^{-3} at 63 K (figure 5.14.a).

Chapter 6

p-doping of ZnO

The studies on ZnO started at the beginning of 1950's (Mollwo et al. Erlangen, Germany). But the attention is slackened up to the middle of 1990's, because the epitaxial growth of ZnO is difficult and the p-type doping did not succeed. n- and p-type conduction is necessary for electronic applications like diodes and bipolar transistors. Since middle of 1990's there is an increasing interest because of the hope for an alternative material to GaN, which is the main material of commercially available light emitting and laser diodes in the blue and UV spectrum [72]. The processing of GaN and ZnO is not easy, their band-gaps are nearly equal, but ZnO has a significant higher exciton binding energy of 60 meV which facilitates many optical applications.

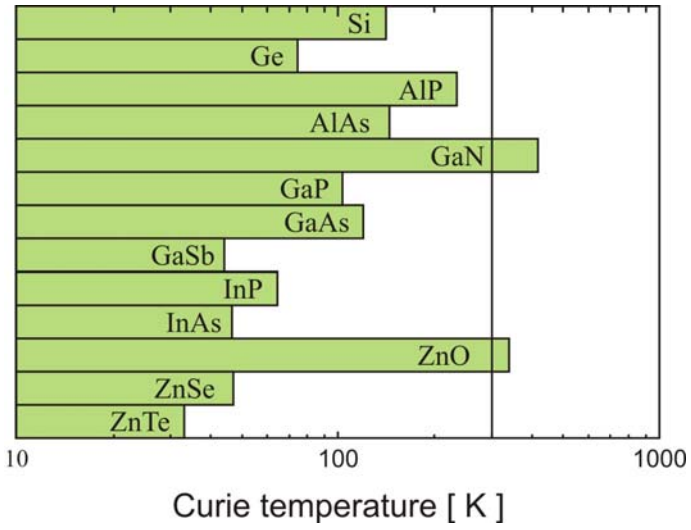

Figure 6.1: *A comparison of Curie temperatures of various material classes [46].*

Additionally, magnetic ions like Co can be incorporated into ZnO to make it magnetic and prepare it as a material for spintronics. So, ZnO is a promising candidate to realize a diluted magnetic material, and actually with Curie temperature above room temperature (figure 6.1). There is thus a high interest to achieve reproducible p-type doping also in ZnO.

6.1 Sample preparation

The sapphire-substrate is annealed at 500°C for 3 h in a high-vacuum sputtering chamber with a base pressure of $1 \cdot 10^{-7}$ mbar and etched for 10 min with an Ar ion beam before the deposition of ZnO. The ZnO layer with a nominal thickness of about 20 nm, according to the deposition time, is grown by sputter on the single-crystalline oriented a-plane Al_2O_3 (sapphire) wafer, of which both sides are polished. RF (13.56 MHz) sputtering is performed in an atmosphere of $5 \cdot 10^{-3}$ mbar pure Ar (99.999%) at 500°C. In order to increase the crystallinity of the ZnO films, a post-growth annealing process is carried out in an oxygen atmosphere with a partial pressure of up to 2000 mbar and a temperature of 800°C. After annealing, ZnO samples are implanted in *ILU-3* ion accelerator (*KPTI of RAS*) with 40 keV Co^+ ions at doses ranging from $0.25 \cdot 10^{17}$ ions/cm^2 to $2.00 \cdot 10^{17}$ ions/cm^2, at an ion current density of 8 µA/cm^2. For Hall measurements in van der Pauw geometry, four Au contacts are evaporated, of which the I(V) characteristics exhibits an ohmic behaviour, and have resistances ranging from 100 Ω to 1 kΩ determined by Hall measurements as drawn in figure 5.2.b in chapter 5. The layer structure and the Au contacts are shown in figure 6.2.

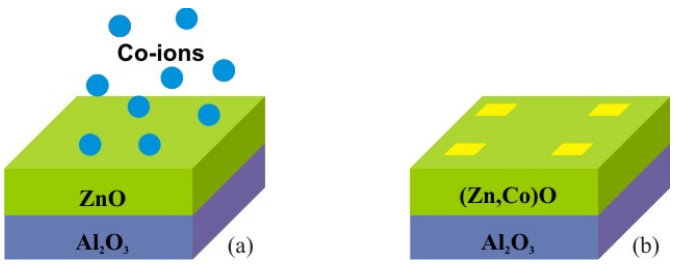

Figure 6.2: *Co^+ ions are implanted at various doses into ZnO grown on a-plane sapphire (a). Au contacts are realised (b).*

6.2 Hall measurements

The Hall data for Co-implanted ZnO samples with different doses are summarised in table 6.1 and table 6.2. These measurements are executed several times and the results are reproducible. For the lowest two doses ($0.25 \cdot 10^{17}$ ions/cm^2, $0.50 \cdot 10^{17}$ ions/cm^2) and for the highest one ($2.00 \cdot 10^{17}$ ions/cm^2), the measurements cannot be made because of a too small signal-to-noise ratio of the Hall voltage. For all other doses, a positive Hall voltage is measured, which clearly indicates that the material is p-type.

Table 6.1: *Hall data of the samples #CZ3 (D = $0.75 \cdot 10^{17}$ ions/cm^2), #CZ4 (D = $1.0 \cdot 10^{17}$ ions/cm^2), and #CZ5 (D = $1.25 \cdot 10^{17}$ ions/cm^2) at RT are summarised. D is the implantation dose.*

Features	#CZ3	#CZ4	#CZ5
Sheet resistivity [Ω]	245	69	132
Hall voltage [µV]	587	480	48
Hall mobility [cm^2/Vs]	45	87	68
2D hole concentration [cm^{-2}]	$5.7 \cdot 10^{14}$	$1.0 \cdot 10^{15}$	$6.9 \cdot 10^{14}$

Table 6.2: *Hall data of the sample #CZ6 at RT and 4.2 K are summarised, where the implantation dose is $1.50 \cdot 10^{17}$ ions/cm^2.*

Temperature	300 K	4.2 K
Sheet resistivity	55 Ω	48 Ω
Hall voltage	7 µV	5 µV
Hall mobility	172 cm^2/Vs	91 cm^2/Vs
2D hole concentration	$6.7 \cdot 10^{14}$ cm^{-2}	$1.5 \cdot 10^{15}$ cm^{-2}

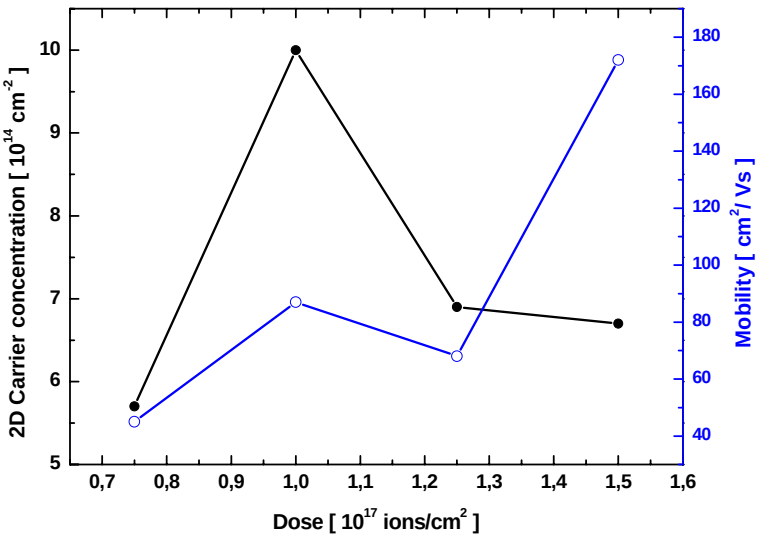

Figure 6.3: *The 2D hole concentration and the mobility as a function of implantation dose.*

The 2D hole concentration increases with increasing implantation dose, which is an indicator to the incorporation of Co into the ZnO crystal lattice.

However, in order to be sure that this results are trustable, anomalous Hall measurements are performed. Because, at lower magnetic fields the behaviour of the Hall voltage is determined by both ordinary and anomalous Hall terms. Thus a confident measurement has to do above the saturation field where the Hall voltage depends directly on the magnetic field, if the sample is ferromagnetic as the samples *#CZ3* - *#CZ5*. If the slope of the $V_H - B$ curve is negative, there is an electron conduction, and a positive slope indicates a hole conduction. Figure 6.4 shows the results of the anomalous Hall measurements. The negative slope at the saturation field exhibits that the formed material system is n-type and the carrier (electron) density is about $2 \cdot 10^{15}$ cm^{-2}.

As mentioned previously, p-type doping of wide-band-gap semiconductors (ZnO, GaN, ZnSe,…) is very difficult. The difficulties can arise from various reasons. Dopants may be compensated by low-energy native defects, such as Zn_i (Zn interstitials). Low solubility of the dopant in the host material is another possible

reason. Deep impurity levels can also be a source of doping problem, causing significant resistance to the formation of shallow acceptor level [73].

p-type doping in ZnO is possible by substituting either group-I elements Li, Na, and K for Zn sites or group-V elements N, P, and As for O sites. As for the authors' knowledge, there are so far few reports on the high and stable p-type doping, because of the reasons mentioned in the previous paragraph.

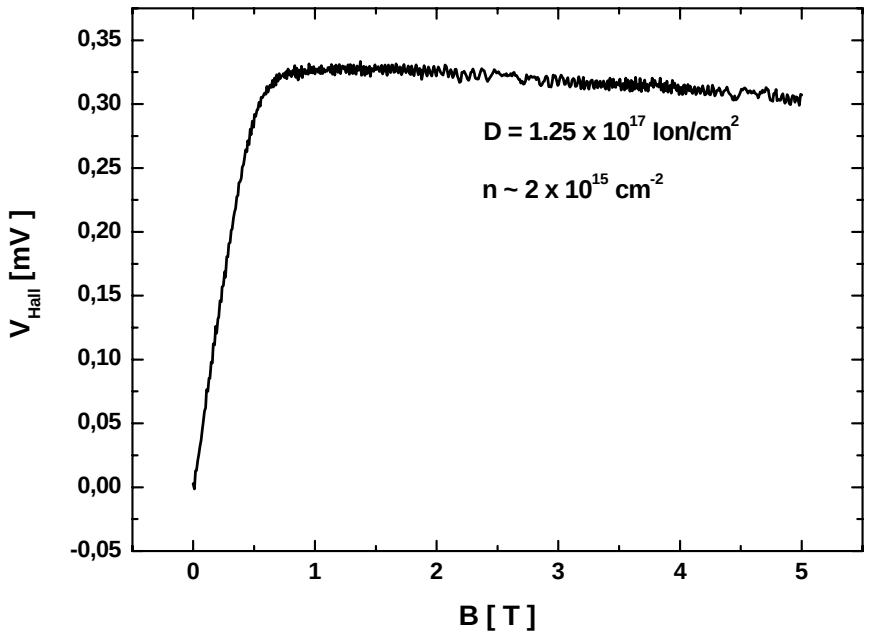

Figure 6.4: *The anomalous Hall effect on the sample #CZ5 observed at 4.2 K. D is the implantation dose of the ions and n is the electron density.*

Chapter 7

Summary and outlook

Although *spintronics* is a novel term introduced in 1996, today's research in spintronics bases on results obtained in diverse areas of the science, like magnetism, semiconductor physics, optics, and electronic device technology, and establishes new links between these different disciplines. There is worldwide a big scientific interest in this technology resulting in a large number of papers, conferences, and workshops. Spintronics is seen as one of the key technologies of the future. This new branch of the nanotechnology aims to simultaneously exploit both the charge and the spin of electrons in the same device and to describe the physics of the newborn scientific discipline. One of its tasks is to develop new functionality that does not exist separately in a ferromagnetic material or a semiconductor. In this regard new ferromagnetic materials with Curie temperatures above room temperature are necessary, which are compatible with today's III-V semiconductor electronics. In this respect, the semiconductor-ferromagnetic hybrid materials are excellent candidates, where ferromagnetic nano-magnets are embedded into the semiconductor matrix. Focused ion beam technique offers thereby a useful method to prepare this kind of material systems. The carrier concentration and type in a semiconductor is adjustable by introduction of impurities. Thus, the doping of impurities into the semiconductor tunes not only the concentration and type of the containing carriers, but gives also an opportunity to incorporate magnetic moments. Due to its partially filled 3d-orbitals the transition metal manganese is a good candidate to make a semiconductor magnetic. So the implantation of manganese ions into GaAs, which is one of the two common materials (the other one is silicon) of today's electronics, is performed for structural analysis.

Just after the implantation there are no nanoparticles on the surface, but an increase in the roughness of the surface is observed by AFM indicating to dislocations of the lattice atoms on the sample surface. Only after the annealing process nanoparticles appear on the surface, meaning that Mn and lattice atoms diffuse to the surface forming Mn:Ga_nAs_m alloy as nanoparticles. EDX-spectrum shows additional to the strong Ga and As peaks a weak one at 5.8 keV, which corresponds the *Kα-lines* of Mn. The diameter and the number of the nanoparticles depend on the annealing temperature and duration, implantation dose, and the size of the implanted area. The exact determination of the chemical concentrations of compounds demands investigations by different methods (like TEM, SQUID, AGM, and MCD) confirming in different respects.

The common preparation techniques of simultaneously ferromagnetic and semiconducting (Ga,Mn)As alloys are LT-MBE and MOVPE. In the framework of this thesis the MBE-FIB technique is used in soft-landing mode for the first time to incorporate Mn ions into the host lattice of GaAs with very low crystal defects. The combined MBE-FIB system provides to keep the new grown layer clean during the growth interruption for the deposition of Mn ions. The measured mobility of MBE-FIB samples is hundred times larger than that of the LT-MBE samples. With increasing deposition dose the mobility decreases because of the increasing number of the irregularities in the crystal structure induced during the deposition.

The magnetic features of materials for spintronics, which depends strongly on the position of the magnetic atom in the semiconductor lattice, play a key role for the future applications. Only the Mn ions on substitutional positions (Mn_{Ga}) contribute to the magnetism, and this in dual respect. First they act as a magnetic moment, and on the other side these substitutional ions are acceptors releasing holes to the semiconductor, which are the mediators of the ferromagnetic interaction. So the concentration of the substitutional Mn is a significant parameter. The comparison between the SQUID data of reference, un-annealed and annealed samples indicates that Mn ions can be incorporated into the substitutional lattice sides by ion implantation, where annealing can increase the part of Mn_{Ga}. The Mn_{Ga} content could be calculated from the saturation magnetisation. With FIB technique 57 % of the implanted Mn ions can be induced into the substitutional cation positions in GaAs.

The Curie temperature T_C of (Ga,Mn)As material system is still a mighty challenge. Nazmul et al. achieved the highest Curie temperature of 172 K by today. In this thesis, the Curie temperature of the un-annealed sample measured by transport experiments is 60 K. This low transition temperature could be increased by annealing up to an ambitious value of 125 K. T_C depends on the concentration of the carriers and the magnetic moments. The increase in T_C more than twice indicates that the incorporation of Mn ions is enhanced, which leads to an increase of the carrier concentration with the MBE-FIB technique in soft-landing mode. On the other hand the asymptotic increase of the resistance R_{XX} at low temperatures is typical for semiconductors, so that the prepared material here shows semiconducting and ferromagnetic properties, unfortunately with a low Curie temperature. Anomalous Hall effect confirms the ferromagnetic character of the prepared material system. In order to increase T_C the Mn content and the carrier concentration can be increased, but the increase of Mn leads to an increase in the size of the nanoparticles. The strength of the MR effect depends on the particle size in granular magnetic materials. So there is an optimal size (about 50 nm), where the MR effect becomes strongest [30]. Perhaps, further increase of T_C can be achieved by a high doping of the matrix, which enables p- as well, n-type conduction.

Finally, unless we realise the quantum computer, the realising of spintronic devices, like the spin-transistor stands in the line. The Curie temperature of the ferromagnetic semiconductors, which are the main material of spintronics must be increased. Therefore, a way to increase the carrier concentration and the content of the magnetic moments must be found. An additional object of the future research is the realisation of the p-type doping of ZnO, which is studied by Hall experiments in the framework of this thesis, and the explanation of the responsible mechanisms.

Appendix A

The mask layouts

The mask layouts of mesa structures and contacts are presented in this appendix. The van der Pauw mesa and contact masks are shown lapped in figure A1. The black rectangles are the contacts. Two of the shown structure can be etched on a sample with size of 5x5 mm^2, i.e. totally 40 van der Pauw structures. One of the van der Pauw structures can be seen separately in figure A2.

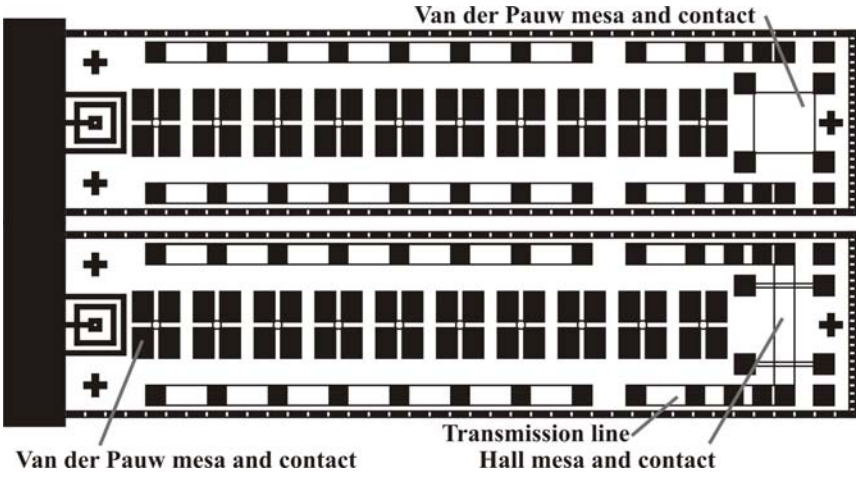

Figure A1: *The van der Pauw mesa and contact mask.*

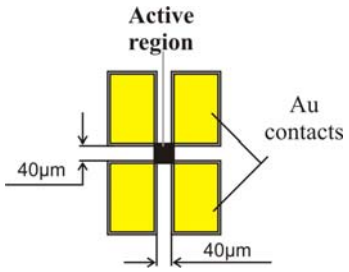

Figure A2: *The size of a single van der Pauw structure.*

The mask for the Hall bar structures is shown in figure A3. The contact mask laps the mesa mask. The evaporated ohmic contacts are depicted as black rectangles.

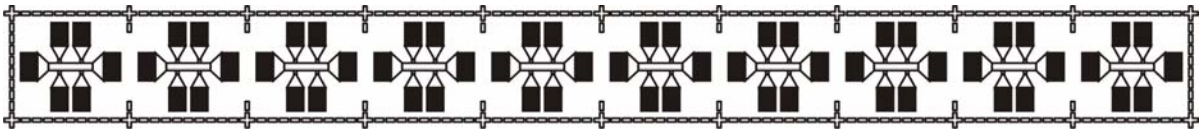

Figure A3: *The mesa and contact mask of the hall bar structures.*

One of the Hall bars is shown separately in figure A4 in order to specify its dimensions. The black bars are the mesa. The yellow rectangles are the gold contacts. The yellow dashed lines above and below the Hall bar are markers, which surround every Hall bar on the mask (this dashed lines are white in figure A3 on the mask). Seven of them can be etched on a sample with the size of 5x5 mm^2.

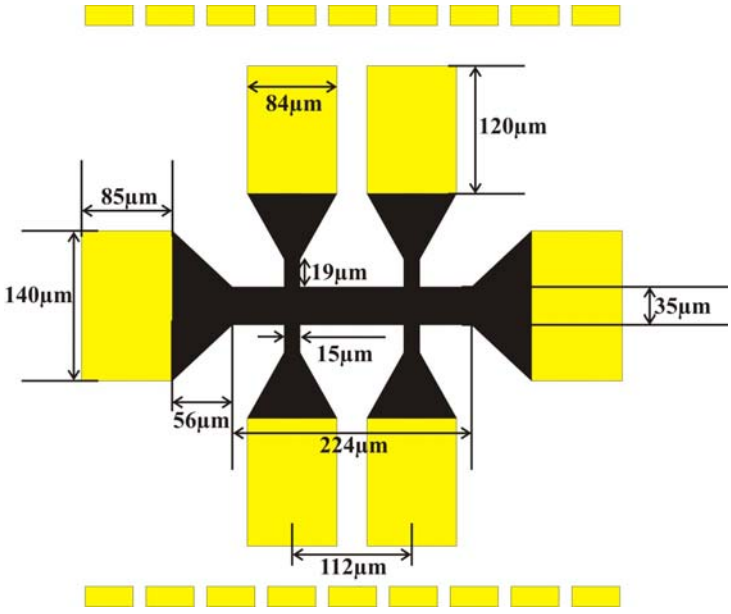

Figure A4: *The size of a single hall bar.*

Appendix B

Synopsis of the selected properties of GaAs

The temperature dependent properties are the values at RT, else denoted in brackets.

Group	III - V compound
Crystal structure	zinc blende
Atomic weight	144.63 amu
Lattice constant	5.653 Å
Density	5.32 g/cm^3 or 4.42·10^{22} Atoms/cm^3
Surface density (10nm thickness)	4.42·10^{16} Atoms/cm^2
E_g (300K / 0K)	1.42 eV / 1.52 eV
Type of the band gap	direct
Electron mobility	8500 cm^2/V s
Hole mobility	400 cm^2/V s
Effective mass of electrons (m^*/m_0)	0.067
Effective mass of holes (m^*/m_0)	(lh) 0.082 and (hh) 0.45
Intrinsic carrier concentration (n_i)	1.79·10^6 cm^{-3}
Donors (with E_D in meV)	Si(5.8), Ge(6), Sn(6), S(6), Te(30),…
Acceptors (with E_A in meV)	Mn(95), Co(160), C(26), Be(28), …

Underlined elements were used in this work.

Effective DOS in CB (N_C)	4.7·10^{17} cm^{-3}
Effective DOS in VB (N_V)	7.0·10^{18} cm^{-3}
Dielectric constant	ε_0 = 12.91 and ε_∞ = 10.1
Increase of gap with pressure	dE_g/dp = 12.6·10^{-10} eV/Pa

For these data is referred to [12].

The phase diagram of GaAs is shown in figure 4.7 in chapter 4.

Appendix C

The sample parameters

The sample series of #s100 and #s3661 are commercial undoped bulk GaAs wafers with a thickness of about 0.47 mm and 0.52 mm, respectively.

Table 1: *The growth data of the unstructured sample #11075.*

MBE sequence	Repetition	Thickness [nm]
GaAs	1	50 (bottom)
GaAs	Start 20x	2
AlAs	End	2
GaAs	1	300 (top)

#M275 is a LT-MBE sample with a 50 nm thick $Ga_{0.94}Mn_{0.06}As$ layer on a GaAs substrate.

Table 2: *The growth data of #12196 and #12198, no HEMT, mesa depth = 520nm.*

MBE sequence	Repetition	Thickness [nm]
GaAs	1	50 (bottom)
GaAs	Start 10x	5
AlAs	End	5
GaAs	1	200
Interruption: Mn deposition	-	-
GaAs	1	120

Table 3: *The Hall data of #12196 and #12198.*

	300 K	77 K	4.2 K
Mobility [cm^2/Vs]	$6.5 \cdot 10^3$	$1.75 \cdot 10^5$	$9.6 \cdot 10^5$
Carrier concentr. [cm^{-2}]	$6.8 \cdot 10^{11}$	$8.5 \cdot 10^{11}$	$4.4 \cdot 10^{11}$

Table 4: *The growth data of the samples #12200 and #12202, 2DHG depth = 136nm, mesa depth = 520 nm.*

MBE sequence	Repetition	Thickness [nm]
GaAs	1	50 (bottom)
GaAs	Start 10x	5
AlAs	End	5
GaAs	1	500
$Al_{0.35}Ga_{0.65}As$	1	15
AlAs	Start 5x	1.1
GaAs	End	2
Interruption: Mn deposition	-	-
AlAs	Start 5x	1.1
GaAs	End	2
$Al_{0.35}Ga_{0.65}As$	1	85
GaAs	1	5

Appendix D

Summary of the constants and units in magnetism

Constants [26]**:**

Velocity of light in free space	$c = 2.9979 \cdot 10^{8}$ m/s
Bohr radius for hydrogen	$a_H = 5.292 \cdot 10^{-11}$ m
Planck's constant	$h = 6.626 \cdot 10^{-34}$ Js
Electron rest mass	$m_0 = 9.109 \cdot 10^{-31}$ kg
Elementary charge	$e = 1.6022 \cdot 10^{-19}$ C
Electric permitivity of free space	$\varepsilon_0 = 8.854 \cdot 10^{-12}$ F/m
Bohr magneton	$\mu_B = 9.274 \cdot 10^{-24}$ Am^2
Magnetic permeability of free space	$\mu_0 = 4\pi \cdot 10^{-7}$ H/m
Magnetic flux quantum	$\Phi_0 = 2.0678 \cdot 10^{-15}$ Tm^2

Units	**SI**	**cgs** [26]**:**
Length	m	100 cm
Mass	kg	1000g
Force	N	10^5 dyne
Energy	J	10^7 erg
Magnetic induction	T	10^4 G
Magnetic field strength	A/m	$4\pi/1000$ Oe
Magnetic moment	J/T or Am^2	1000 erg/G or 1000emu
Magnetisation	A/m or J/Tm^3	10^{-3} Oe
Magnetic susceptibility	1	$1/4\pi$ emu/cm^3

Appendix E

Synopsis of the selected properties of ZnO

The temperature dependent properties are the values at RT, else denoted in brackets.

Group	II - VI compound
Crystal structure	rock salt (B1), (zinc blende (B2), wurzite (B3))
Atomic weight	81.38 amu
Lattice constant	4.580 Å
Density	5.67 g/cm^3
E_g (300K / 0K)	3.35 eV / 3.42 eV
Type of the band gap	direct
Electron mobility	200 cm^2/V s
Hole mobility	180 cm^2/V s
Effective mass of electrons (m^*/m_0)	0.27
Intrinsic carrier concentration (n_i)	$7.0 \cdot 10^{16}$ cm^{-3} (for ZnO on a-plane Al_2O_3)
Donors	Al, Ga, In, Cl, I, …
Acceptors	Li, Na, K, Co, N, P, As …
Dielectric constant	$\varepsilon_0 = 8.12$

For these data is referred to [12, 73].

Bibliography

[1] H. Ohno, Science **281** (1998) 951.

[2] P. Ball, Nature **404** (2000) 918.

[3] S. A. Wolf, D. D. Awschalom, R. A. Buhrman, J. M. Daughton, S. von Molnár, M. L. Roukes, A. Y. Chtchelkanova, and D. M. Treger, Science **294** (2001) 1488.

[4] J. Ackerman, Science **308** (2005) 508.

[5] I. Žutić, J. Fabian, and S. D. Sarma, Rev. Mod. Phys. **76** (2004) 323.

[6] G. A. Prinz, Science **282** (1998) 1660.

[7] H. Munekata, H. Ohno, S. von Molnár, A. Segmüller, L. L. Chang, and L. Esaki, Phys. Rev. Lett. **63** (1989) 1849.

[8] A. Shen, F. Matsukura, S. P. Guo, Y. Sugawara, H. Ohno, M. Tani, H. Abe, and H. C. Liu, J. Crys. Growth **679** (1999) 201.

[9] S. Maekawa, *Concepts in Spin Electronics*, Oxford Univ. Press, NY 2006.

[10] H. S. Nalwa, *Magnetic Nanostructures*, Amer. Scie. Publ., LA 2002.

[11] J. König, *Lectures on Spinelectronics*, summer semester 2006 at Ruhr-University Bochum, Germany.

[12] S.M.Sze, *Physics of semiconductor devices*, Wiley, NY, 1985, p. 249.

[13] J. Singleton, *Band theory and electronic properties of solids*, (Oxford university press, NY, 2004) p. 2.

[14] Bergmann & Schaefer, *Lehrbuch der Experimentalphysik, Band 6: Festkörperphysik*, (de Gruyter, Berlin 1992) p. 226 – 228.

[15] D. Diaconescu, Dissertation, Ruhr-Universität Bochum (2000).

[16] S. Hoch, Dissertation, Ruhr-Universität Bochum (2003).

[17] H. Krenn and P. Granitzer, Phys. in uns. Zeit, 33. Jahrg. 2002, Nr.5.

[18] J. Blinowski and P. Kacman, Phys. Rev. B **67** (2003) 121204(R).

[19] H. Ohno, A. Shen, F. Matsukura, A. Oiwa, A. Endo, S. Katsumoto, and Y. Iye, App. Phys. Lett. **69** (1996) 363.

[20] S. C. Erwin and A. G. Petukhov, Phys. Rev. Lett. **89** (2002) 227201.

[21] S. von Molnár, H. Munekata, H. Ohno, and L. L. Chang, J. Magn. Magn. Mater. **93** (1991) 356.

[22] C. Liu, F. Yun, and H. Morkoç, J. Mat. Scien.: Mat. Electr. **16** (2005) 555.

[23] T. Hayashi, M. Tanaka, and T. Nishinaga, J. App. Phys. **81** (1997) 4865.

[24] S. J. Potashnik, K. C. Ku, S. H. Chun, J. J. Berry, N. Samarth, and P. Schiffer, App. Phys. Lett. **79** (2001) 1495.

[25] A. M. Nazmul, S. Sugahara, and M. Tanaka, Phys. Rev. B **67** (2003) R241308.

[26] S. Blundell, *Magnetism in Condensed Matter*, Oxford University Press, 2004.

[27] T. Dietl, H. Ohno, F. Matsukura, J. Cibert, and D. Ferrand, Science **287** (2000) 1019.

[28] J. König, H. - H. Lin, and A. H. MacDonald, Phys. Rev. Lett. **84**, (2000) 5628.

[29] S. Ye, P. J. Klar, T. Hartmann, W. Heimbrodt, M. Lampalzer, S. Nau, T. Torunski, W. Stolz, T. Kurz, H. - A. Krug von Nidda, and A. Loidl, Appl. Phys. Lett. **83** (2003) 3927.

[30] M. Farle, in **"***Magnetism goes Nano. Electron Correlations, Spin Transport, Molecular Magnetism. Lecture Manuscripts of the 36th Spring School of the Institute of Solid State Research IFF Jülich, 14-25 February 2005***"**, edited by S. Blügel, T. Brückel and C. M. Schneider.

[31] Ch. Kittel, *Einführung in die Festkörperphysik*, (Oldenburg München, 1999).

[32] H. Zabel, *Lectures on Solid State Magnetism*, winter semester 2000/2001 at Ruhr-University Bochum, Germany.

[33] S. Fischer, *Lectures on Magnetoelectronics*, summer semester 2005 at Ruhr-University Bochum, Germany.

[34] A. Hubert and R. Schäfer, *Magnetic domains*, (Springer, Berlin, 2000) p. 108.

[35] A. Fert and C. Voille, in *Vorlesungsmanuskripte: 30. Ferienkurs des Instituts für Festkörperforschung "Magnetische Schichtsyseme"*, Forschungszentrum Jülich 1999.

[36] M. A. Hermann and H. Sitter, *Molecular Beam Epitaxy, Fundamentals and Current Status*, (Springer, Berlin 1989).

[37] M. Henzler and W. Göpel, *Oberflächenphysik des Festkörpers*, (Teubner, 1991), p.285.

[38] M. Ay, Dissertation, Ruhr-Universität Bochum (2004).

[39] K. Ploog, Angewandte Chemie, **Heft 5** (1988) 611-780.

[40] H. J. Osten, in *Physik Journal*, **Oktober** (2005) 43-48.

[41] T. Hartmann, Dissertation, Philipps-Universität Marburg (2003).

[42] Dr. A. Melnikov, personal impartation.

[43] M. Born and E. Wolf, *Principles of Optics* (MacMillan, NY, 1959).

[44] R. L. Seliger, J. Appl. Phys. **43** (1972) 2352.

[45] R. P. Feynman, R. B. Leighton, and M. Sands, in *Feynman Vorlesungen über Physik* (Oldenbourg, 2001) Band II, Kap. 29-3.

[46] T. C. Shen, G. B. Gao, and H. Morkoç, J. Vac. Sci. Technol. B **10(5)** (1995) 2113.

[47] C. Y. Chang, Y. K. Fang, and S. M. Sze, Solid-State Electron. **14**, (1971) 541.

[48] L. J. van der Pauw, Philips Res. Repts. **13**, 1 (1958).

[49] K. W. Edmonds, K. Y. Wang, and R. P. Campion, App. Phys. Lett. **81** (2002) 3010-3012.

[50] J. Singleton, *Band theory and electronic properties of solids*, (Oxford university press, NY, 2004) p. 2.

[51] S. Goek, Diploma thesis, Ruhr University Bochum (2001), p. 27.

[52] M. McElfresh, *Fundamentals of magnetism and magnetic measurements, featuring quantum design's, magnetic property measurement system*, Quantum Design (1994).

[53] J. Orloff, M. Utlaut, and L. Swanson, *High resolution focused ion beams*, Kluwer Academic / Plenum Publishers 2003.

[54] R. Baeuerlein, Zeit. f. Phys., **176** (1963) 498-507.

[55] D. K. de Vries, Dissertation, Max-Planck Institut für Festkörperforschung, Stuttgart (1995).

[56] J. F. Ziegler, J. P. Biersack, and U. Littmark, *The stopping and range of ions in solids*, **Vol. 1** of *the stopping and ranges of ions in matter*, Pergamon Press 1985.

[57] Ü. Dağkaldiran, Diploma thesis, Ruhr-Universität 2002.

[58] A. E. White, K. T. Short, R. C. Dynes, J. P. Garno, and J. M. Gibson, Appl. Phys. Lett. **50**(2) (1987) 95-97.

[59] W. G. Moffatt, *The Handbook of binary phase diagrams*, General Electric Company, (1978) p. 05/02.

[60] F. A. Shunk, *Constitution of binary alloys*, Material science and engineering series, McGraw-Hill (1969).

[61] W. Heimbrodt and P. J. Klar, *Magnetic nanostructures*, edited by H. S. Nalwa, American Sciencetific Publishers (2002).

[62] K. Ando, A. Chiba, and H. Tanoue, Appl. Phys. Lett. **73** (1998) 387.

[63] P. J. Wellmann, J. M. Garcia, J.-L. Feng, and P. M. Petroff, App. Phys. Lett. **73** (1998) 3291.

[64] J. Shi, D. D. Awschalom, P. M. Petroff, and K. Babcock, J. App. Phys. **81** (1997) 4331.

[65] J. Shi, J. M. Kikkawa, D. D. Awschalom, G. M.-Ribeiro, P. M. Petroff, and K. Babcock, J. App. Phys. **79** (1996) 5296.

[66] C. Chen, M. Cai, X. Wang, S. Xu, M. Zhang, X. Ding, and Y. Sun, J. Appl. Phys. **87** (2000) 5636.

[67] H. P. J. Wijn, *Magnetische Eigenschaften nicht-metallischer anorganischer Verbindungen von Übergangselementen*, Landolt - Börnstein III/27a, Springer-Verlag (1988).

[68] P. J. Wellmann, J. M. Garcia, J.-L. Feng, and P. M. Petroff, App. Phys. Lett. **71** (1997) 2532.

[69] J. K. Furdyna, J. Appl. Phys. **64** (1988) R29.

[70] C. Michel, P. J. Klar, S. D. Baranovskii, and P. Thomas, Phys. Rev. B **69** (2004) 165211.

[71] L. Berger and G. Bergmann, in *The Hall Effect and Its Applications*, edited by C. L. Chien and C. R. Westgate, Plenum Press, NY 1979, p. 55-61.

[72] C. Klingshirn, M. Grundmann, A. Hoffmann, B. K. Meyer and A. Waag, Physik Journal, January 2006, p.33-38.

[73] Ü. Özgür, Ya. I. Alivov, C. Liu, A. Teke, M. A. Reshchikov, S. Doğan, V. Avrutin, S.-J. Cho, and H. Morkoç, J. Appl. Phys. **98** (2005) 041301.

Zusammenfassung

Die im Jahr 1996 eingeführte Bezeichnung *Spintronik* ist relativ neu, aber die Spintronik-Forschung basiert auf traditionelle Ergebnisse aus diversen Fachbereiche der Physik, wie Magnetismus, Halbleiterphysik, Optik und elektronische Bauteil-Technologie und etabliert neue Verknüpfungen zwischen diesen verschiedenen Disziplinen. Es gibt weltweit großes Interresse von wissenschaftlicher Seite für Spintronik-Technologie, welches zu einer großen Anzahl von Veröffentlichungen, Konferenzen und Tagungen führt. Spintronik wird als eine der Schlüssentechnologien der Zukunft angesehen. Der neue Zweig der Nanotechnologie anvisiert eine gleichzeitige Ausbeutung des Ladungs- und des Spinfreiheitsgrats der Ladungsträger in einem und in demselben Bauteil, und die Beschreibung der Physik dieses neugeborenen interdisziplinären Fachbereichs. Eine Aufgabe der Spintronik ist die Entwicklung neue Funktionalitäten, die getrennt in einem ferromagnetischen Material oder in einem Halbleiter nicht vorhanden sind. In diesem Zusammenhang sind neue ferromagnetische Materialien mit Curie-Temperaturen oberhalb der Raumtemperatur notwendig, die mit der heutigen III-V Halbleiterelektronik kompatibel sind. In dieser Hinsicht sind die Halbleiter-Ferromagnet-Hybridmaterialien ausgezeichnete Kandidaten, in denen ferromagnetische Nano-Magnete in der halbleitenden Matrix eingebetet sind. Die Technik der fokusierten Ionenstrahlen bieten dabei eine nützliche Methode an, um Materialsysteme dieser Art herzustellen. Die Konzentration und der Typ der Ladungsträger in einem Halbleiter ist einstellbar mittels Einbau von Verunreinigungen. Also, die Dotierung von Halbleitern mit Verunreinigungen stellt nicht nur die Konzentration und Typ der Ladungsträger ein, sondern bringt gleichzeitig dem Einbau von magnetischen Momenten hervor. Durch seine partiell besetzte 3d-Orbitale ist der Übergangsmetal Mangan ein guter Kandidat, der einen Halbleiter magnetische Eigenschaften vergeben kann. Daher wurden Mn-Ionen implantiert in das

Halbleitermaterial GaAs, welches eines der zwei gebräuchlichsten Materialien der heutigen Elektronik ist (das andere Material ist Silizium).

Direkt nach der Implantation sind keine Nano-Partikel an der Oberfläche beobachtet, aber einen Anstieg der Oberflächenrauigkeit wurde mittels AFM festgestellt. Dies ist ein Zeichen dafür, daß die Oberflächenatome des Gitters versetzt wurden. Nur nach der thermischen Ausheilung erscheinen Nano-Partikel an der Oberfläche, d.h. Mn und Gitteratome diffundieren zur Oberfläche und bilden dort Mn:Ga_nAs_m Legierung als Nanopartikel. EDX-Spektren zeigen neben den starken Ga und As Peaks einen schwachen Peak bei 5.8 keV, der den K_α-Linien von Mn entspricht. Der Durchmesser und die Anzahl der Nano-Partikel hängen von der Ausheiltemperatur, der Ausheildauer, der Implantationsdosis und der implantierten Fläche ab. Die genaue Bestimmung der chemischen Zusammensetzung der neu entstandenen Verbindungen fordert untersuchungen (wie TEM, SQUID, AGM und MCD), die sich gegenseitig in verschiedener Hinsicht ergänzen und bestätigen.

Die gebräuchliche Präparationstechniken von (Ga,Mn)As Legierungen, die gleichzeitig ferromagnetisch und halbleitend sind, sind LT-MBE und MOVPE. Im Rahmen dieser Arbeit wurde MBE-FIB-Technik in sogenannter „soft-landing“ Modus eingesetzt, um Mn-Ionen in das GaAs Wirtsgitter mit sehr wenigen Kristaldefekten einzubauen. Die kombinierte MBE-FIB-Anlage bietet die Möglichkeit an, die neu gewachsene Schicht während der Wachstumspause für die Mn-Deposition sauber zu halten. Die gemessenen Mobilitäten sind hundertmal größer als die der LT-MBE-Proben. Mit steigender Depositionsdosis wird die Mobilität kleiner wegen der steigenden Anzahl der durch Deposition verursachten Irregularitäten in der Kristallstruktur.

Die magnetischen Eigenschaften der Materialien für Spintronik, die stark von der Position des magnetischen Atoms in dem halbleitenden Gitter abhängt, spielt eine Schlüsselrolle für die Anwendungen. Nur die Mn-Ionen auf Ga-Plätze (Mn_{Ga}) tragen zum Magnetismus bei, und dies in zweifacher Hinsicht. Erstens diese Atome wirken als magnetische Momente. Zweitens wirken sie als Akzeptoren, die das Vermittlerteilchen der ferromagnetischen Wechselwirkung (nämlich Löcher) freigeben. Daher ist die Konzentration der Mn-Atome auf Ga-Plätze ein signifikanter Parameter. Der Vergleich zwischen den SQUID-Daten von Referenz-, nicht-

ausgeheilte und ausgeheilte Proben deutet darauf hin, daß die Mn-Ionen in das Gitter auf Ga-Position durch Deposition eingebaut werden können, wobei deren Anzahl durch das thermische Ausheilen gesteigert werden kann. Die Anzahl der Mn-Ionen auf Ga-Plätze kann aus Sättigungsmagnetisierung berechnet werden. Mit der FIB-Technik kann 57% der deponierten Mn-Ionen auf substitutstionelle Kation-Position in GaAs eingebaut werden.

Die Curie-Temperatur T_C von (Ga,Mn)As Materialsystem ist immer noch eine große Herausforderung. Nazmul et al. erreichten die bisher höchste Curie-Temperatur von 172 K. In dieser Arbeit beträgt die gemessene Curie-Temperatur der nicht-ausgeheilten Probe 60 K. Diese tiefe Übergangstemperatur konnte durch thermisches Ausheilen auf einen anspruchsvollen Wert von 125 K gesteigert werden. T_C hängt von der Konzentration der Ladungsträger und der magnetischen Momente ab. Die Steigerung in T_C von mehr als zweifach ist ein Zeichen dafür, daß der Einbau der Mn-Ionen gesteigert ist, welches widerum zu einer Steigerung der Ladungsträgerkonzentration mittels MBE-FIB-Technik in „soft-landing“-Modus führt. Auf der anderen Seite ist die asymptotische Anstieg des Widerstandes R_{XX} bei tiefen Temperaturen typisch für Halbleiter, so daß das vorliegende Material sowohl Halbleitereigenschaften als auch ferromagnetische Eigenschaften mit leider einer niedrigen Übergangstemperatur hat. Der anomale Hall-Effekt bestätigt die ferromagnetische Character des hergestellten Materials. Um die Curie-Temperatur zu erhöhen, können Mn-Gehalt und die Ladungsträgerkonzentration erhöht werden. Allerdings, die Erhöhung des Mn-Gehalts führt zur Vergrößerung des Durchmessers der entstandenen Nano-Partikel. Die Stärke des Magneto-Widerstand-Effekts in granularen magnetischen Materialien hängt von der Teilchengröße ab. Es gibt also eine optimale Teilchengröße, bei der der MR-Effekt am stärksten ist. Weitere Erhöhung der Curie-Temperatur könnte wahrscheinlich durch eine hohe Dotierung der Matrix erzielt werden, welches eine p- sowie n-Leitung ermöglicht.

Abschließend muß bemerkt werden; bevor wir den Quanten-Computer realisieren, steht die Realisierung der Spintronik-Bauteile, wie Spin-Transistor, in der Reihe. Die Curie-Temperatur der ferromagnetischen Halbleiter, welche das Hauptmaterial der Spintronik-Bauteilen sind, muß weiter gesteigert werden. Dazu muß einen Weg zur Erhöhung der Konzentration der Ladungsträger und der magnetischen Momente

gefunden werden. Weitere Objekte der zukünftigen Forschung sind die p-typ dotierung von ZnO, wie im Rahmen dieser Arbeit studiert wurde, und die Erklärung des verantwortlichen Mechanismus.

Acknowledgement

I would like to express my acknowledgements to the following people:

Prof. Dr. A. D. Wieck for the kind reception in his group and for giving me the opportunity to work in an interesting field of semiconductor physics; my "master" both in lab and in office **Dr. A. Melnikov** for his help in all imaginable phases during the development of this thesis; **Dr. Murat Ay** for the thorough corrections of this thesis and for the supervising at every opportunity from afar, **Dr. D. Diaconescu** and **Dr. S. Hoch** for supporting me performing experiments as well as for the discussions concerning electronics and measurement techniques; **Dr. J.-L. Yang**, **Dr. D. Reuter** and **F.-Y. Lo** for growing the samples and "office conversations" about every thing; SFB491 speaker **Prof. Dr. H. Zabel** for his contribution to the evolution of my thesis particularly through the subjects in chapter 5 with the sample #M275; **Dr. C. Riedesel** for his help in getting some literature and support in German and English, **Dr. A. Ebbers** for his help in lab; **Dr. S. Uenluebayir** and **M. Richter** for corrections of my thesis, **N. Viteritti** for her help in sample preparation, **C. Werner** and **D. Salloch** for supporting in computer problems; **Dr. A. Rehmhof**, **A. Westfalen** and **N. Akdogan** for their help in performing EDS, MOKE and SQUID measurements; **G. Kortenbruck**, **R. Wernhardt** and **P. Stauche** for their technical support, introduction to the phase diagrams, conversation about life and for their touristic consultation; **C. Rockensüß**, **R. Lehnart** and **P. Hahn** in secretary for performing the paperwork; also all the other members of the institutes Applied Solid State Physics and Experimental Physics 4 for their friendship; and last but not least my lovely wife **Guelşen** for her hard work so that I didn't need to do any work at home and my sweet children **Elyesa Davut** and **Zeynep Meryem** for their lovely hug at the door so that I could enter my house happily.

Curriculum vitae

Name:	Gök, Şafak
Date of Birth:	26.01.1971
Place of Birth:	Zonguldak, Turkey
Marital status:	maried, 2 children
Citizenship:	Turkish

1977 – 1980	Primary School in Recklinghausen, Germany.
1980 – 1982	Central Primary School *Çatalağzı* in Zonguldak, Turkey.
1982 – 1985	Secondary school *Çatalağzı* in Zonguldak, Turkey.
1985 – 1988	*Mehmet Çelikel* High School in Zonguldak, Turkey.
1988 – 1993	Engineering of Physics, Faculty of Natural Sciences at Ankara University, Turkey. Title: Physics Engineer BSc Thesis: *Yarıiletken Laser Diyotlar* (translated: *Semiconductor Laser Diods*). Supervisor: Prof. Dr. F. Bayrakçeken.
1994 – 1996	Prepared for *Die Prüfung zum Nachweis deutscher Sprachkenntnisse* for the admission to Physics study.
February 1996	Passed at Ruhr University Bochum, Germany
1996 – 2001	Study of Physics at Ruhr University Bochum, Germany.
October 2001	Diploma in Physics at Ruhr University Bochum, Germany. Thesis: *Abbildung magnetischer Domänen* (translated: *Imaging of magnetic domains*). Supervisor: Prof. Dr. H. Zabel.
Since 2002	PhD student at Department for Applied Solid State Physics at Ruhr University Bochum, Germany. Supervisor: Prof. Dr. A. D. Wieck.